Mechanisms and methods for identification and monitoring of lateral subsurface flow in erosion affected arable soil landscape of the hummocky ground moraine

Dissertation
zur Erlangung des
Doktorgrades der Naturwissenschaften (Dr. rer. nat.)

der

Naturwissenschaftlichen Fakultät III
Agrar- und Ernährungswissenschaften,
Geowissenschaften und Informatik

der Martin-Luther-Universität Halle-Wittenberg

vorgelegt von

Frau Annelie Ehrhardt
Geb. am 11.08.1993 in Berlin

Gutachter:

Prof. Dr. Hans-Jörg Vogel
PD Dr. Horst H. Gerke
Prof. Dr. Ole Wendroth

Verteidigung am 16.01.2023

Acknowledgments

Abstract

Lateral subsurface flow (LSF) is a ubiquitous phenomenon occurring along impeding layers in the subsurface of hillslopes across various landscapes in the world. It poses severe risks to the environment, for example, by enhanced pesticide and nutrient transport or by initiating landslides. In contrast to forested landscapes, mechanisms and boundary conditions leading to the onset of LSF in agricultural soils remain unresolved.

The aim was to enhance the understanding how soil surface structure, soil macropores and precipitation conditions influence LSF occurrence along agricultural hillslopes in hummocky ground moraines.

The first objective was to find a method to deduce the impact of the soil surface structure and its influencing processes like soil erosion and soil settlement on LSF.
Soil surface structural changes were analyzed by the photogrammetric technique Structure-from-Motion (SfM). The processes of soil settlement and soil erosion were separated by correcting soil height changes detected by SfM with bulk density changes measured and modelled with the Root-Zone-Water-Qualitiy-Model (RZWQM). Experiments were conducted for small-scale plots (1 x 1.5 m²) at the upper, middle and lower part of a soil erosion measurement slope.
Bulk density measurements and the modeling approach (RZWQM) improved the SfM-derived soil erosion amounts and allowed the distinction between soil erosion and natural soil settlement. At upper slope sections soil settlement was the dominant process for soil surface structural changes, whereas at the middle slope soil erosion was the prevalent process. At the footslope position mainly soil deposition from upper slope parts was observed.
It may now be further analyzed how these individual processes are linked to the occurrence of LSF and how individual soil surface structures exhibit influence on LSF.

The second objective was to capture LSF events by comparing time series of water content data from a set-up of a lysimeter soil and an instrumented field soil at the lysimeter excavation site. Here, the discrepancies between the restricted vertical water flow in the lysimeter and the possibly laterally flowing water in the field might indicate LSF. Thus, boundary conditions leading to the occurrence of LSF can be derived.
The method of wavelet coherence analysis (WCA) was applied to correlate water content time series and find time shifts in the onset of water content increase after precipitation in a lysimeter soil and a corresponding field soil of an Endogleyic Colluvic Regosol.
A faster water content increase in the field in spring and autumn in the field soil was successfully identified by WCA and indicated possible lateral water inflow from upper slope

parts. Results suggest that LSF occurs under long precipitation events with a high amount of precipitation.

The first insight on possible boundary conditions leading to LSF need to be confirmed by analyzing such water content time series of other profiles. An optimization of the sensor placement closer to actual horizon boundaries would allow the observation of perched water tables during infiltration events indicating LSF.

The third objective was to analyze if the mechanism of macropore induced local water saturation along horizon boundaries leads to the occurrence of LSF in agricultural soils.

This was tested in a laboratory precipitation experiment on an undisturbed and rectangular soil monolith (25 x 25 x 12 cm³) sampled at a B-C-horizon boundary of an agriculturally used soil. Soil water content and soil water tension changes were monitored along a vertical macropore ending at a horizon boundary. A technique for sampling undisturbed soil monoliths was developed to allow for 2D modeling of water flow along horizon boundaries.

The first observed soil monolith showed little macropore induced occurrence of LSF along the horizon boundary. Experimental results were successfully verified by 2D-modeling of the water flow within the monolith.

The results imply that LSF occurs only under very specific conditions that were not captured in the experiments, e.g., by a lack of a perched water table due to a weak texture contrast between the impeding layer and the layer above. Further experiments need to be conducted to analyze under what texture contrasts macropore induced LSF is a relevant mechanism in agricultural landscapes.

To derive a more detailed conceptual model of LSF occurrence in agricultural landscapes also other mechanisms possibly inducing LSF must be tested. For instance, it remains unclear what role subsurface macropore networks, often observed in forested landscapes, play in agricultural soils. Dye and salt tracing techniques as well as ground penetrating radar (GPR) measurements might reveal such a network along impeding layers in the subsurface.

Zusammenfassung

Unterirdische laterale Flüsse (ULF) entlang von geneigten Horizontgrenzen in Böden treten in verschiedenen Landschaften auf. Sie stellen durch erhöhten Pestizid- und Nährstofftransport in angrenzende Gewässer oder durch das Auslösen von Hangrutschungen ein Umweltrisiko dar. Im Gegensatz zu bewaldeten Gebieten sind Mechanismen und Bedingungen, die ULF auslösen, in ackerbaulich genutzten Hängen nur wenig erforscht.

Ziel dieser Arbeit ist es das Verständnis zu erweitern, wie Bodenoberflächenstrukturen, Makroporen und Niederschlagsereignisse das Auftreten von ULF entlang von ackerbaulich genutzten Hängen in hügeligen Grundmoränen beeinflussen.

Hierfür wurde zunächst untersucht, mit welcher Methode die Einflüsse der Bodenoberflächenstruktur auf ULF detektiert werden können. Ziel war es dabei zwischen den die Bodenoberfläche beeinflussenden Prozessen der Sackung und Bodenerosion zu unterscheiden. Bodenoberflächenstrukturveränderungen wurden mit Hilfe der Structure-from-Motion- (SfM) Photogrammetrie analysiert. Die Prozesse der natürlichen Bodensackung und der der Bodenerosion wurden mittels Korrektur der SfM-detektierten Bodenhöhenveränderungen durch Lagerungsdichtemessungen und -modellierung durch das Root-Zone-Water-Qualtiy-Model (RZWQM) voneinander unterschieden. Die Experimente wurden auf kleinskaligen Plots (1 x 1.5 m²) am oberen, mittleren und unteren Teil eines Erosionsmesshanges durchgeführt. Lagerungsdichtemessungen und – modellierung (RZWQM) verbesserten die mittels SfM ermittelten Bodenhöhenänderungen durch Erosion und ermöglichte im Rahmen der Bodenhöhenveränderungsmessungen eine Unterscheidung der Prozesse der Bodenerosion und der natürlichen Sackung. Am Oberhang war Bodensackung ein dominierender Prozess für Bodenoberflächen-veränderungen, während am Mittelhang Erosion vorherrschte. Am Unterhang wurde v.a. Deposition beobachtet. Es ist nun möglich, den Einfluss der Bodenoberflächenstruktur und der sie beein-flussenden Prozesse der Bodenerosion und Sackung auf die Entstehung von ULF zu untersuchen.

Ein weiteres Ziel war die Erfassung von ULF mittels Vergleich der Zeitreihen von Wassergehaltsdaten eines Lysimeters und dem am Entnahmeort des Lysimeters instrumentierten Feldprofil. So können auf ULF hindeutende Unterschiede im Fließverhalten des im Lysimeter nur senkrecht fließenden Wassers und dem im Feldprofil frei beweglichen Wasser ermittelt werden. Auf diese Weise ist es möglich Einflüsse von äußeren Randbedingungen wie Niederschlägen auf die Entstehung von ULF abzuleiten. Die Methode der Wavelet-Kohärenz-Analyse (WCA) wurde zur Korrelation der Wassergehalts-Zeitreihen und Analyse des zeitlichen Versatzes des Wasser-

gehaltsanstiegs nach Niederschlagsereignissen eines Lysimeters und des dazugehörigen Feldprofils eines Kolluviums herangezogen. Ein schnellerer Anstieg des Wassergehalts im Feldprofil im Frühjahr und Herbst wurde erfolgreich mit der WCA nachgewiesen und deutet auf einen lateralen Wasserzutritt vom Oberhang hin. ULF tritt v. a. nach langen Regenereignissen mit hoher Niederschlagsmenge auf. Die ersten Ergebnisse über mögliche Randbedingungen zum Auslösen von ULF, die durch das Lysimeter-Feld-Experiment ermittelt wurden, müssen durch Analyse von Zeitreihen anderer Böden unter gleichem experimentellem Aufbau bestätigt werden. Eine Optimierung der Sensorplatzierung entlang der Bodenhorizontgrenzen würde es ermöglichen eine lokale Sättigung über der Stauschicht während der Infiltration zu beobachten, die zum Entstehen ULF führen könnte.

Schließlich wurde überprüft, ob der Mechanismus der durch Makroporenfluss induzierten lokalen Sättigung entlang von Horizontgrenzen ein Auslöser für das Auftreten von ULF darstellt. Dazu wurden Beregnungsversuche an einem ungestörten, rechteckigen und an einer A-C-Bodenhorizontgrenze einer ackerbaulich genutzten, hügeligen Grundmoräne entnommenen Bodenmonolithen (25 x 25 x 12 cm³) im Labor durchgeführt. Wassergehalts- und Tensionsveränderungen wurden entlang einer vertikalen auf einer Bodenhorizontgrenze endenden Makropore überwacht. Zur Entnahme von ungestörten, rechteckigen Bodenmonolithen, die der zweidimensionalen Modellierung von Wasser-flüssen dienten, wurde eine neue Probeentnahmemethode entwickelt. Der erste Bodenmonolith zeigte nur eine geringe Tendenz zum Makroporen-induzierten Auftreten lateraler Flüsse. Die experimentellen Ergebnisse konnten mit einer 2D-Modellierung der Fließprozesse im Monolithen überprüft werden. Die Ergebnisse legen nahe, dass ULF nur unter sehr spezifischen Bedingungen auftritt, die im durchgeführten Experiment nicht erreicht wurden, beispielsweise durch eine zu geringe Stau-Wirkung aufgrund zu schwacher Texturunterschiede entlang der Horizontgrenze. In weiteren Versuchen gilt es zu ermitteln unter welchen Texturunterschieden der durch Makroporen induzierte ULF in Agrarlandschaften relevant wird.

Um ein detaillierteres konzeptionelles Modell zum Auftreten ULF in Agrarlandschaften zu entwickeln, ist es notwendig auch andere Mechanismen, die zu ULF führen könnten, zu untersuchen. Z.B. ist es unklar, welche Rolle unterirdische Makroporennetzwerke, die häufig in bewaldeten Hängen beobachtet werden, für das Auftreten ULF in ackerbaulich genutzten Böden entlang von Hängen spielen. Farb- und Salztracerversuche sowie Bodenradaruntersuchungen können über ein solches Netzwerk entlang von Stauschichten im Untergrund Aufschluss geben.

Contents

List of figures

List of tables

Abbreviations

BC	Boundary Condition
COI	Cone Of Influence
DEM	Digital Elevation Model
DoD	DEMs of temporal Difference
EMI	Electromagnetic Induction
ERI	Electrical Resistivity Imaging
ERT	Electrical Resistivity Tomography
FDR	Frequency Domain Reflectometry
GCP	Ground Control Point
GPR	Ground Penetrating Radar
HNE	Hydraulic Nonequilibrium
LSF	Lateral Subsurface Flow
LoD	Level of Detection
PVC	Polyvinyl Chloride
RMSE	Root Mean Square Error
RZWQM	Root-Zone-Water-Quality-Model
SfM	Structure-from-Motion
SR	Seed Row
SWC	Soil Water Content
TL	Tractor Lane
TRI	Terrain Ruggedness Index
VAMOS	Vadose Zone Monitoring Systems
Vol-%	unit of the volumetric soil water content in volume percentage
VPF	Vertical Preferential Flow
WCA	Wavelet Coherence Analysis
WTC	Wavelet Coherency Spectrum
1D	one-dimensional
2D	two-dimensional
3D	three-dimensional

1 Introduction

1.1 Lateral subsurface flow in soils

Lateral subsurface flow (LSF) or funnel flow is the lateral redirection of water in the soil caused by textural boundaries, where water follows the least resistance to bypass less permeable zones (Hendrickx and Flury, 2001; Jarvis et al., 2016). It occurs when infiltrating water moves laterally and locally along an inclined hydraulically restrictive layer such as bedrock (Allaire et al., 2009).

LSF is a **ubiquitous phenomenon** found in various landscapes across the world and in different soil textures. It has been reported to occur mostly in forested hillslopes, for example, in Japan (Sidle et al., 2001), in Northern America (Lin et al., 2006) or Germany (Wiekenkamp et al., 2016). Also, in mountainous landscapes like the Alps in Europe (Maier et al., 2021) or the cloud-forested mountains in Costa Rica (Tobón and Bruijnzeel, 2021) LSF is to be found. Agricultural landscapes at various continents are subject to LSF occurrence: pasture and farmland in Tasmania (Hardie et al., 2013b), agricultural soil in New Zealand (Wöhling et al., 2012), paddy fields in Southern China (Zhang et al., 2011), vineyards in France (Peyrard et al., 2016) and ditch-drained agroecosystems in Northern America (Robinson et al., 2020). LSF is found in various soil textures, such as sandy soils (McCord and Stephens, 1987), loam (Wilcox et al., 1997), silt (Walter et al., 2000), clay (Patil and Das, 2013) and gravel (Miyazaki, 1988).

The lateral movement of water in the subsurface causes **environmental problems**, especially in agricultural landscapes. Firstly, nutrients like nitrate or phosphate might be leached and are not available to plants. Pesticides are transported by LSF and pollute groundwater resources and streams adjacent to agricultural fields. Lateral subsurface transport was observed for fungicides and insecticides in a litchi orchard in Northern Thailand (Kahl et al., 2008) and for nitrate transport in Eastern China (Xie et al., 2019). Also, LSF causes landslides by elevated pore water pressures along impermeable layers in the subsurface, thus posing a direct risk to human lives. Landslides induced by LSF were found in the Swiss Alps (Schneider et al., 2014) and Austrian Alps (Wienhöfer et al., 2011) as well as in the Qinling Mountains in Western China (Dai et al., 2022). Finally, LSF induces subsurface soil erosion leading to the vertical collapse of the soil body along a hillslope (Tao et al., 2020) and contributing to nutrient and pesticide loss and water pollution.

All in all, the risks induced by LSF and its occurrence in various landscapes and soil types imply the necessity to better understand and predict this phenomenon, especially for agricultural soils. Thus, in the following sections the state of the art in LSF will be summarized and knowledge gaps are derived.

1.2 Mechanisms of lateral subsurface flow occurrence

Mechanisms inducing LSF can be grouped into structural prerequisites and boundary conditions. Under structural prerequisites soil characteristics and geomorphologic or topographical features causing LSF are summarized. Boundary conditions describe the non-structural parameters influencing LSF, like weather conditions.

1.2.1 Structural prerequisites

Soil characteristics influencing LSF are (i) soil structure and (ii) soil moisture induced heterogeneity, (iii) plant roots, (iv) connectivity of macropores and (v) soil bedrock structure or porosity.

(i) The difference of hydraulic conductivity between two layers (***soil structural heterogeneity***) in the subsurface is one of the most common prerequisites for LSF occurrence. Vertically infiltrating water is laterally diverted into a more permeable horizon underlain by a less permeable layer (e.g., bedrock). As the soil gets saturated in a small section just above the impeding layer a pressure head builds up and a perched water table is created. This is referred to as transmissivity-feedback phenomenon and has been observed primarily in forested catchments along the soil bedrock interface (Fig. 1.1, [d]) (e.g., Laine-Kaulio et al., 2015, McNamara et al., 2005). If lateral macropores (e.g., from plant roots or burrowing animals) are located along the soil-bedrock interface, the perched water table can lead to concentrated lateral preferential flow within the macropores of forest soils (Fig. 1.1, [c]) (Buttle and McDonell, 2002; Nyquist et al., 2018). Although water flow along the soil-bedrock interface might be the most frequently observed type of LSF, other interfaces lead to LSF as well. Gerke et al. (2015) observed LSF between the litter layer and the underlying mineral soil of a forest soil in dye-tracer experiments (Fig. 1.1, [g]). LSF was found in soils with a horizon of higher permeability underlain by a compacted horizon of lower permeability in forested catchments (Fig. 1.1, [h]) (Guo et al., 2014), in pasture land (Fig. 1.2, [h]) (Hardie et al., 2012), in flood irrigated land (Claes et al., 2019) and steep vineyard soils (Peyrard et al., 2016). In agricultural landscapes the soil bulk density contrast between the loose surface layer and the compacted plough pan creates an interface for the initiation of LSF as observed by Sander and Gerke (2007) and Tang et al. (2010) (Fig. 1.2, [m]). LSF is also caused by smaller discontinuities like sand (Kung, 1990) or clay lenses (Walter et al., 2000) (Fig. 1.2, [k]). Even frozen layers in the subsurface lead to the lateral redirection of vertical water flow in permafrost soils (Fig. 1.1, [i]) (Wales et al., 2020).
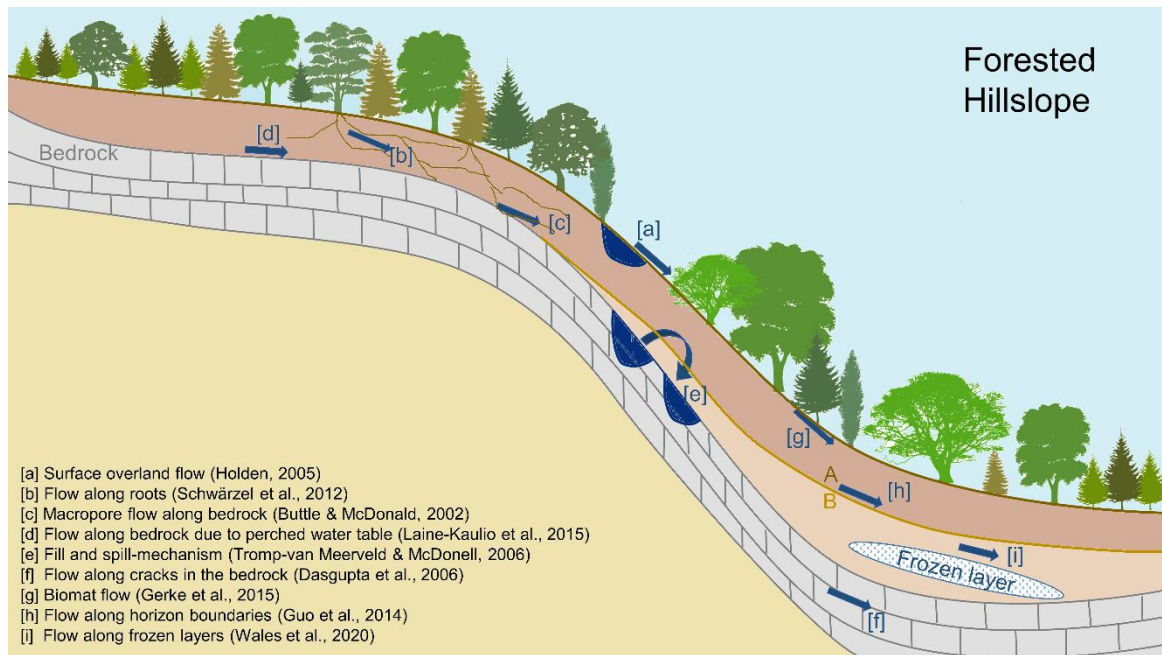
Figure 1.1: Concepts of LSF occurrence in forested hillslopes
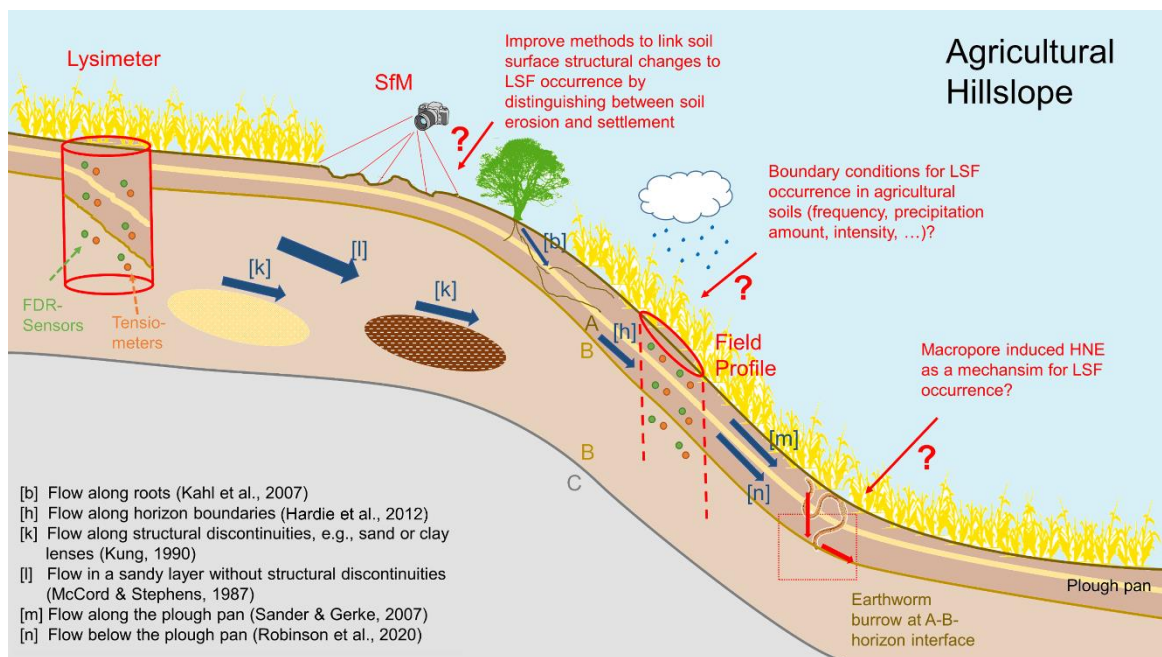
Figure 1.2: Concepts of LSF occurrence in agricultural hillslopes

(ii) Despite soil heterogeneity induced by soil structure also **soil moisture heterogeneities** might induce LSF: McCord and Stephens (1987) found LSF in a structurally homogeneous sandy layer without an impeding layer in the subsurface (Fig. 1.2, [l]). They attributed this to moisture redistribution and increased soil moisture below the land surface during infiltration leading to a zone of high hydraulic conductivity where flow paths might converge. This leads to an accumulation of soil moisture in

downslope direction. A similar mechanism might be responsible for the occurrence of LSF below the plough pan in a ditch drained field without an apparent impeding layer in the subsurface (Robinson et al., 2020) (Fig. 1.2, [n]).

(iii) ***Plant roots*** and their channels can serve as pathways for lateral preferential flow as was demonstrated for beech forest in temperate climate (Schwärzel et al., 2012) (Fig. 1.1, [b]), litchi orchards in tropical climate (Kahl et al., 2008), and pine forests in semiarid climate (Newman et al., 2004). However, single macropores can only act as preferential flow pathways over rather short distances like 0.6 m (Noguchi et al. 1999).

(iv) Thus, the ***connectivity between*** those ***macropores*** is an important parameter that needs to be considered. Sidle et al. (2001) proposed a conceptual model for steep forested slopes stating that macropores are interconnected by zones of loose soil and buried organic matter. In times of subsurface stormflow these zones are saturated and allow the subsurface water to pass between the macropores. Uchida et al. (2004) extended this concept by distinguishing between low and high permeable soil. In high permeable soils macropores are connected (or hydrologically active) even under dry conditions. With increasing wetness, the hydrologically active area is extended to upper slope zones. In low permeable soils macropores are not connected. As the soil moisture increases, the hydrologically active area extends further upslope than in high permeable soil.

Besides the connectivity, the disconnections of macropores, for example, by cemented material found within the soil, need to be considered. Laine-Kaulio and Koivusalo (2018) showed in a modeling study that due to the disconnection of macropores the flow in the connected macropores increases.

(v) ***Soil bedrock*** is often considered as a structure that acts as an impeding layer for LSF occurrence. However, LSF has been observed to occur within the bedrock itself, for example, when the bedrock is highly fractured like in limestone soil (Dasgupta et al., 2006) (Fig. 1.1, [f]). Thus, the bedrock structure plays an important role for LSF formation.

As **geomorphologic or topographical features** (i) slope angle, (ii) slope position, (iii) soil bedrock topography and (iv) soil surface structure influence LSF.

(i) Walter et al. (2000) could show in laboratory experiments that the differences in matric potential along the horizon interfaces increase with a stronger ***inclination of the slope***.

(ii) The occurrence of LSF depends on the ***slope position***: Lee and Kim (2019b) could show that subsurface water flow in a Korean hillslope is mainly vertical at the upper slope aeras, whereas LSF is likely to occur in footslope positions.

(iii) The ***topography of the impeding layer*** (e.g., bedrock layer) in the subsurface determines the onset of LSF. Tromp-van Meerveld and McDonell (2006) observed that depressions along the impeding layer or bedrock need to be filled with water to start spilling over the bedrock micro-topography. LSF along the hillslope is initialized after the entire soil-bedrock interface is hydraulically connected by a perched water table (fill-&-spill-mechanism) (Fig. 1.1, [e]).

(iv) The ***soil surface structure*** is a significant factor that influences how much of the precipitation water is infiltrated directly or diverted as infiltration excess or saturation excess overland flow (Holden, 2005) (Fig. 1.1, [a]). For example, a soil surface with a high roughness consisting of many depressions, where the water is collected during precipitation events, will more likely lead to local saturation and vertical infiltration and possible LSF than a soil with flat soil structure that redirects all precipitation water as overland flow.

1.2.2   Boundary conditions

Boundary conditions affecting LSF are (i) precipitation amount and (ii) intensity, (iii) antecedent soil moisture or (iv) saturation of the soil and (v) the distance to the water table.

(i) Regarding the ***precipitation amount*** a general consensus exists that more precipitation leads to an increase in LSF: Tang et al. (2010) found that LSF ceased under small precipitation amounts and a shorter duration of the precipitation events in a sloped farmland in Belgium. After classifying the precipitation events in a forested catchment in South Korea into insignificant, intermediate and significant events Lee and Kim (2021) demonstrated that only intermediate and significant precipitation events cause LSF. A minimum of 15 to 20 mm of precipitation per precipitation event was required to initiate LSF in a forested hillslope in Alberta, Canada (Redding and Devito, 2008). According to Hardie et al. (2012) LSF is possibly initiated after less precipitation in agricultural soils in comparison to forested soils, since the impeding layer in farmlands, i.e., the plough pan, is often closer to the surface than the bedrock layer in forested catchments. However, the actual depth of the layer causing LSF is site specific, and layers located at greater depths might additionally lead to the initiation of LSF in farmland.

(ii) Guo et al. (2018) demonstrated the influence of ***precipitation intensity*** on LSF generation: LSF was found along the soil-bedrock interfaces, in particular after short and intense precipitation events in a forested catchment. In a similar catchment Redding and Devito (2008) suggested precipitation intensity as a first-order control of LSF occurrence as well. LSF events caused by vertically infiltrating water were observed more frequently with increasing precipitation intensity by Liu et al. (2021) in a mountainous watershed in

Southwest China. These findings on LSF are in accordance with observations about vertical preferential flow (VPF) occurrence: VPF events in the form of water bypassing single horizons have been shown to occur more often under high intensity than low intensity precipitation in forested catchments (Liu and Lin, 2015; Wiekenkamp et al., 2016; Demand et al., 2019).

(iii) ***Initial soil moisture conditions*** prior to precipitation events influence the formation of LSF in two possible ways: Under dry conditions the hydrophobicity of the soil enhances the occurrence of LSF (Guo et al., 2018), whereas under wet conditions the connectivity between single macropores is established by the saturation of loose zones of soil and organic matter between the macropores (e.g., Sidle et al., 2001; McNamara et al., 2005). Kahl et al. (2008) could show that LSF occurred under dry conditions in the topsoil and under wet conditions in the subsoil.

(iv) However, it is still unclear whether soil ***saturation*** is required to initiate LSF. In several studies the occurrence of LSF was observed during flood irrigation of agricultural fields (e.g., Claes et al., 2019; Robinson et al., 2020). Newman et al. (2004) found LSF along the macropores of the Bt-horizon in a semiarid pine forest only after the A-horizon was fully saturated. Studies of LSF in forested catchments indicate that at least along the soil-bedrock interface a perched water table is required to initiate LSF (e.g., Nyquist et al., 2018; Weiler and McDonell, 2007). However, Laine-Kaulio et al. (2015) found LSF in a forested hillslope under saturated and under unsaturated conditions.

One mechanism of LSF initiation under unsaturated conditions is preferential flow through macropores: During precipitation events water infiltrates more easily into larger macropores causing local saturation and so called hydraulic nonequilibrium (HNE) conditions within the area around the macropores (e.g., Newman et al., 2004). Local saturation at the point of contact between macropore and impeding layer might lead to the onset of LSF. HNE describes a phenomenon where fast changes in water potential are followed by a redistribution of water and gas behind a drainage or wetting front (Hannes et al., 2016). In a water retention curve this is indicated by the water content lagging behind the water potential given by the equilibrium water retention curve. Schlüter et al. (2012) demonstrated that elongated structures like macropores in the direction of water flow induce such HNE conditions.

(v) Finally, the ***groundwater table*** influences the occurrence of LSF: Christiansen et al. (2004) and Logsdon (2007) observed that LSF was more likely to occur in areas with shallower water tables than in areas with a greater distance between the impeding layer and the water table.

1.3 Methodological advancements and bottlenecks in lateral subsurface flow detection

A wide variety of methods has been applied at field and laboratory scale to gain an understanding on the mechanisms and conditions leading to the initiation of LSF. In this section these methods are summarized and possible amendments are suggested.

1.3.1 Lateral subsurface flow detection at field scale

Methods to detect LSF at field scale include (i) non-invasive methods, (ii) tracer application, (iii) modeling studies and (iv) the installation of soil moisture sensor networks.

(i) ***Non-invasive methods*** are techniques that monitor the water flow within the soil without disturbing the soil structure. Guo et al. (2014) identified LSF in a macropore network of 2 m² area and 1.4 m depth with ground-penetrating radar (GPR). The application of electrical resistivity tomography (ERT) for LSF identification was demonstrated successfully by Scaini et al. (2017). However, experimental evidence by Leslie and Heinse (2013) suggests that ERT for LSF observation might be only applicable to homogeneous soils, since the texture contrast at the horizon boundary masks macropores. Electromagnetic induction (EMI) was applied by Zhu and Lin (2009) to identify LSF along a clay enriched layer of an agricultural soil.

(ii) Application of dye or salt ***tracers*** into the soil solution visualizes relevant flow paths within the soil (e.g., Allaire et al., 2009). However, the analysis of the tracer distribution often requires disturbing the soil structure by excavation and thus the results cannot be reproduced. With dye tracers like Brilliant Blue or Uranine lateral flow paths along beech roots (Schwärzel et al., 2012) and LSF between the litter layer and the mineral soil (Gerke et al., 2015) were identified. The salt tracer potassium bromide has been applied to detect LSF along the interface of an organic and a mineral horizon in a forest soil (Koch et al., 2017) and to analyze differences in the lateral movement of water along roots in a deciduous and coniferous forest (Luo et al., 2019).

(iii) ***Modeling*** studies help to predict the occurrence of LSF where soil parameters are known, but the direct observation of water flow is not possible. Filipović et al. (2018) could show within a numerical study the occurrence of LSF along horizon boundaries in an agricultural field of a hummocky ground moraine. Similarly, Dušek et al. (2012) were able to find LSF induced by vertical infiltration through macropores in a forest soil.

(iv) ***Soil moisture sensor networks*** are useful for investigating LSF in larger areas than plot or field scale. They consist of multiple sensors located across a larger study area (like a catchment) measuring parameters like soil moisture or tension at different depths automatically in short time intervals (min to h) over a long period of time (several years)

(Guo and Lin, 2018). Martini et al. (2015) detected LSF at the boundary between Bt- and Bw-horizons with such a soil moisture sensor network. Different methods for analyzing subsurface water flow of these network based measurements are available. The Non-sequential Soil Moisture Response (NSMR) method allows for the detection of VPF: If the soil moisture responds to precipitation in a deep soil horizon earlier than in horizons closer to the surface the water must have bypassed the upper horizons indicating VPF (e.g., Hardie et al., 2013a; Graham and Lin, 2011). Occurrence of LSF can be derived by the soil water mass balance (SWMB) method (Guo et al., 2018; Lee and Kim, 2019a): If the soil water storage in one horizon increases more than the vertical input by precipitation indicates, additional water must have entered the soil horizon laterally. Self-organizing maps were applied by Lee and Kim (2021) as a machine learning tool to cluster different hydrologic events registered by a soil moisture sensor network in a South Korean forested hillslope. The derived clusters could be attributed to different flow events including LSF. Wavelet analysis as a tool to correlate periodic time series was used to identify LSF events. Thus, correlations of soil water content changes at different soil depths along a slope (Lee and Kim, 2019b) and correlations between discharge and soil moisture were revealed (Liu et al., 2020).

Often, the application of one single method is not sufficient to derive subsurface flow patterns. Sidle et al. (2001) combined detailed soil structural observations from excavations within the observed catchments (e.g., measurements of macropore length and density) with dye staining tests to derive their conceptual model of lateral flow by interconnections through macropores. In the Shale Hills Catchment (Pennsylvania, USA) detailed topographic maps showing, for example, the depth to bedrock gained by auger observations were combined with soil moisture sensor network measurements to derive LSF patterns along soil-bedrock interfaces (Lin et al., 2006).

1.3.2 Lateral subsurface flow detection in laboratory experiments

Laboratory experiments help to identify local mechanisms inducing LSF under controlled conditions (e.g., known precipitation rate or defined slopes). Walter et al. (2000) examined the effect of capillary barriers on the generation of funnel flow. Xie et al. (2019) were able to derive the lateral transport of nitrate under defined precipitation rates. However, most laboratory experiments are conducted with artificially created, i.e., repacked disturbed soil samples. Hereby, the soil structure within the artificial sample is known to the observers. As main disadvantage, the transfer of the laboratory results to field conditions is impeded if the natural soil structure is destroyed. However, taking large undisturbed samples from the field or measuring in-situ in the field requires a lot of effort (e.g., Germer and Braun, 2015; Pirastru et al., 2017).

1.3.3   Surface structure detection and its impacts on lateral subsurface flow

The topsoil surface structure is an important contributor to the occurrence of LSF. For example, the roughness of a topsoil determines whether ponding occurs during a precipitation event or not. Ponding indicates that soil is possibly locally saturated and that at these areas LSF might be initiated along impeding layers. For instance, Ma et al. (2022) could show that more LSF occurs along slopes with a rough soil surface than along slopes with a smooth soil surface. Also, the initiation of LSF was faster in soils with a rough soil surface structure in comparison to smooth soil surfaces (Ma et al., 2022).

The soil surface structure is highly dynamic and is influenced by processes like soil erosion and soil settlement. Both processes might be related to different subsurface flow patterns. One of the main causes for soil settlement is the vertical infiltration of water: the filling of the soil pores with water enhances contractive forces of water menisci between soil particles (Hartge et al., 2014) leading to a reduction in soil height. In contrast, soil erosion indicates the occurrence of overland flow due to the saturation of upper soil layers (Holden, 2005). Under these circumstances LSF might be initiated along impeding layers in the subsurface (Newman et al., 2004).

In order to assess how LSF is affected by the different processes influencing soil surface structural changes it is necessary to detect and analyze these dynamics. Non-invasive techniques are employed to capture these temporal changes over longer time periods. Photogrammetric methods like Terrestrial Laser-Scanning (TLS) or Structure-from-Motion (SfM) (e.g., Eltner et al., 2015) allow the generation of three-dimensional soil surface models at several points in time. However, the soil surface height changes gained from these models need to be attributed to soil erosion and soil settlement (Hänsel et al., 2016). To analyze how these processes affect soil surface structural changes and thus the onset of LSF separately, it is necessary to develop adequate methods to distinguish between soil height changes due to soil erosion and soil settlement.

1.4   Knowledge gaps of LSF occurrence in agricultural landscapes

LSF is more common in forested catchments (Fig. 1.1) and thus the mechanisms for the onset of LSF are better investigated in comparison to agricultural soils. The reasons for the more frequent observations of LSF in forests and alpine hillslopes might be the smaller solum thickness over the bedrock in comparison to agricultural areas. Also, forest soils are more structured by tree roots that serve as preferential flow pathways.

The boundary conditions for LSF formation in agricultural landscapes are less well understood than in forest soils. Hardie et al. (2012) suggested that possibly less precipitation is required to initiate LSF in agricultural soils than in forest soil. Soil moisture

sensor networks might help to investigate this question (Guo and Lin, 2018). One approach to detect LSF at field scale is the comparison of soil water content time series of a lysimeter and corresponding field soil (Fig. 1.2). Water flow in a lysimeter is restricted to the vertical direction, whereas in the field at the lysimeter excavation site water can still flow laterally. Under similar precipitation conditions, water content changes in the lysimeter might differ temporally from water content changes in the field when LSF occurs in the latter. In these cases, LSF can be indicated by time shifts in the correlations between the water content time series of a lysimeter and field soil. However, classical correlation analysis like Pearson-correlation fails for non-stationary time-series like water content data (Biswas and Si, 2011). A promising tool to account for these temporal shifts and scale variabilities in the correlation of periodic time series is the wavelet coherence analysis (WCA). However, the application of WCA to such a lysimeter-field sensor network has not been studied and might give new insights into boundary conditions causing LSF.

Also, the mechanisms of LSF occurrence in agricultural landscapes differ from those in forest areas. In agricultural soils earthworm burrows instead of tree roots mainly serve as preferential flow pathways. Instead of the soil-bedrock-interface other interfaces like horizon boundaries or the plough pan act as impeding layers for the initiation of LSF (Sander and Gerke, 2007; Hardie et al., 2012). One possible mechanism for LSF occurrence in agricultural landscapes is VPF along macropores that might initiate local saturation along horizon boundaries and cause LSF under nonequilibrium conditions (Fig. 1.2, earthworm burrow). Such a mechanism would provide the missing link between VPF and LSF (Allaire et al., 2009) and can be investigated by 2D-soil core experiments with undisturbed sampled soil monoliths with (artificial) macropores.

In forests the soil is covered from the direct impact of heavy precipitation initiating soil erosion by the leaf canopy (Holz et al., 2015). Thus, processes changing the soil surface structure like soil erosion or soil settlement have a higher impact on the onset of LSF in agricultural landscapes than in forest soils. In order to assess the impact of soil surface structural changes on the initiation of LSF, appropriate methods for the detection of processes impacting the soil surface structure are needed (Fig. 1.2). However, the mentioned techniques of soil surface structure detection and soil erosion quantification by SfM cannot distinguish between soil settlement and soil loss due to erosion. One approach that has not been tested so far is the calculation of soil settlement via bulk density changes derived from equations presented in the Root-Zone-Water-Quality-Model (RZWQM) (Linden and van Doren, 1987).

1.5   Objectives and Hypotheses

The aim of this thesis is to provide further understanding of mechanisms and factors influencing the onset of LSF in agricultural landscapes of hummocky ground moraines. From the knowledge gaps stated above the following hypotheses and objectives are derived:

(I)   The **first objective** is to enable finding the link between the occurrence of LSF and soil surface structure and processes influencing the soil surface structure like soil erosion and settlement. Therefore, photogrammetric methods like SfM for the analysis of soil surface structures need to be improved by attributing soil height changes separately to soil settlement and soil erosion. The **first hypothesis** is that soil height changes recorded by SfM can be attributed separately to soil erosion or natural soil settlement if soil settlement is accounted for via bulk density change detection (Chapter 2).

(II)   The **second objective** is to gain insights on boundary conditions impacting the occurrence of LSF in agricultural soils by extending existing methodologies for detecting LSF. The **second hypothesis** is that LSF is indicated by differences in soil moisture dynamics between a field soil and a soil with similar horizon sequence in the lysimeter. A novel set-up of soil sensor networks is presented by comparing water content time series of a lysimeter, which omits lateral water movement, and a corresponding field soil extracted from an agricultural hillslope. Time shifts in the correlation of the time series are identified by applying wavelet coherence analysis (Chapter 3).

(III)   The **third objective** is to enhance the understanding on mechanisms leading to the initiation of LSF in agricultural soils. The **third hypothesis** is that local pore water saturation (i.e., water potentials close to zero) can lead to the onset of lateral and preferential flows. An experimental set-up providing evidence for LSF in soil monoliths under nonequilibrium conditions of macropore infiltration is presented (Chapter 4).

In Chapter 5 the individual methodological improvements for LSF detection and their limits will be discussed. First conceptual findings for the occurrence of LSF in agricultural soil of hummocky ground moraines will be derived and further steps to create a conceptual model for LSF in this landscape will be presented.

1.6   Experimental sites

As experimental sites hillslopes in morainic agricultural landscapes were chosen. The first experimental hillslope is located in Müncheberg (Eastern Brandenburg). Here it was possible to compare the soil loss measured along the hillslope in smaller plots by the SfM photogrammetry to the collected sediment at the footslope by an automated sediment collector station.

At the CarboZALF-D experimental site in Dedelow (Northern Brandenburg) the occurrence of LSF has been assumed since a virtual tracer experiment by Filipović et al. (2018). Also, Rieckh et al. (2012) reported texture and bulk density contrasts between the soil horizons with possibly impeding layers suggesting the presence of LSF. The vadose zone monitoring systems (VAMOS) were installed at three hillslope positions at the CarboZALF-D experimental site (Haplic Regosol, eroded Haplic Luvisol, Endogleyic Colluvic Regosol) to observe LSF. Three lysimeters and the corresponding field profiles at the extraction sites of the lysimeters were equipped with soil water content sensors and tensiometers. Thus, soil water dynamics can be monitored simultaneously inside and outside of the lysimeters, possibly indicating the occurrence of LSF. The schematic approach of the experimental set-up is depicted in Fig. 1.2.

2 Soil surface micro-topography by Structure-from-Motion photogrammetry for monitoring density and erosion dynamics

2.1 Abstract

Soil erosion is a major threat to soil fertility, food security and water resources. Besides a quantitative assessment of soil loss, the dynamics of erosion-affected arable soil surfaces still poses challenges regarding field methods and predictions because of scale-dependent and soil management-related complex soil-crop-atmosphere processes. The objective was to test a photogrammetric Structure-from-Motion (SfM) technique for the mm-scale mapping of the soil surface micro-topography that allows the monitoring without special equipment and with widely available cameras. The test was carried out in May 2018 on three plots of 1.5 m^2 (upper-, middle-, and footslope) covering surface structural features (tractor wheel lane, seed rows) along a Maize-cultivated hillslope with a coarse-textured topsoil and a runoff monitoring station. The changes in mm-scaled surface micro-topography were derived from repeatedly photographed images of the same surface area during a 2-weeks period with two rain events. A freely available SfM-program (VisualSfM) and the QGIS software were used to generate 3D-models of the surface topography. Soil cores (100 cm^3) were sampled to gravimetrically determine the topsoil bulk density. The micro-topographical changes resulting from rainfall–induced soil mass redistribution within the plots were determined from the differences in SfM maps before and after rain.

The largest decrease in mean soil surface elevation and roughness was observed after rain for the middle slope plot and primarily in initially less compacted regions. The spatially-distributed intra-plot changes in soil mass at the mm-scale derived from the digital micro-topography models indicated that local depressions were filled with sediments from surrounding knolls during rainfall. The estimated mass loss determined with the SfM technique decreased, if core sample-based soil settlement was considered. The effect of changes in the soil bulk density could be described after calibration also with an empirical model suggested in the Root-Zone-Water-Quality-Model. Uncertainties in the presented plot-scale SfM-technique were due to geo-referencing and the numerical limitations in the freely available SfM-software. The photogrammetric technique provided valuable information on soil surface structure parameters such as surface roughness. The successful application of SfM with widely available cameras and freely available software might stimulate the monitoring of erosion in regions with limited accessibility.

2.2   Introduction

Soil loss due to erosion is a global threat to arable land, environment and agricultural productivity (e.g., Pimentel & Burgess, 2013; Borrelli et al., 2013; Sutton et al., 2016). In order to take effective erosion control measures, it is necessary to quantify the soil mass that has been translocated during erosion (García-Ruiz et al., 2015). Standard approaches include stationary sediment and run-off collectors installed at experimental hillslopes, which can operate automatically for the event-based erosion monitoring (e.g., Deumlich et al., 2017) or temporary rainfall simulation experiments (e.g., Kaiser et al., 2015). Disadvantages of these methods include the cost for installation in case of monitoring stations and the relatively small surveillance areas of rainfall simulators (Boardman, 2006). Recently, the Structure-from-Motion (SfM) photogrammetry has been developed as an alternative method (James and Robson, 2012; Eltner et al., 2016) to generate Digital Elevation Models (DEMs) in relatively high spatial resolution (Eltner et al., 2015). By combining the images taken from several cardinal points after calibration (Westoby et al., 2012), this method allows to even utilize digital images from low-cost consumer-grade cameras such as those in smart-phones (Micheletti et al., 2015; Prosdocimi et al., 2017) for the calculation of 3D DEMs. Repeated photographic imaging of the same surface at consecutive times allows to derive the DEM of Difference (DoD) for determining temporal changes in soil micro-topography (Eltner et al., 2017); a mean decrease in surface elevation is indicating a soil loss (e.g., erosion) while an increase represents a gain (e.g., sedimentation). Changes in the soil surface micro-topography have also been determined by using laser scanning (e.g., Haubrock et al., 2009; Nouwakpo et al., 2016). But in contrast to SfM, laser scanning is more expensive and not widely accessible (Nadal-Romero et al., 2015). The SfM technique has already been applied to quantify soil erosion (Di Stefano et al. 2017, Vinci et al., 2017; Meinen and Robinson, 2020) or to monitor crop growth variability (Bendig et al., 2013). It has been used to identify soil structural discrepancies between conservation and conventional agriculture (Tarolli et al., 2019), and to quantify soil roughness parameters depending on soil cultivation practices (Martinez-Agirre et al., 2020).

A major challenge not only for the SfM-based quantification of soil erosion is to distinguish between soil surface elevation changes by erosion (which can be deposition of soil material from uphill regions and soil loss towards downhill regions) and changes that could occur due to soil compaction or settlement (Hänsel et al., 2016; Kaiser et al., 2018). Freshly cultivated soils are characterized by an initially unconsolidated and relatively loose structure that can easily collapse during wetting or due to raindrop impact (e.g., Bergsma und Valenzuela, 1981). This natural soil settlement can be determined by comparing the soil bulk density before the rain storm and after the soil erosion event (Hänsel et al., 2016).

Empirical model approaches to estimate the bulk density changes due to soil settlement of arable soils accounted for rain intensity and rainfall energy (e.g., Linden and van Doren, 1987; Ahuja et al., 2006); these models were implemented, for instance, in the Root-Zone-Water-Quality-Model (RZWQM) (Ahuja et al., 2000).

The accuracy of the determination of changes in the soil surface topography obtained from 3D DEMs was found to decrease with increasing plot sizes due to limited image resolution (e.g., Kaiser et al., 2018). Thus, soil height loss analyzed by SfM-photogrammetry at smaller plots could only be qualitatively compared to data collected at hillslope scale with a sediment collector station. It is well known that an upscaling of soil loss is not possible because erosion processes are scale-dependent (Boix-Fayos et al., 2006; Parsons, 2019). Boix-Fayos et al. (2007) observed increased sediment yields at larger plots as compared to smaller scales, whereas Martinez et al. (2017) reported decreased sediment yields at larger (27 m²) as compared to smaller plots (0.7 m²). The comparison of soil erosion results obtained from differently-sized plots does not allow quantifying rates of components of the soil mass changes; but it may provide relevant qualitative information on the soil surface micro topography dynamics (Boix-Fayos et al. 2007).

Another more technical limitation is that licensed software such as Agisoft Photoscan has been applied to generate DEMs by SfM in soil erosion studies (e.g., Laburda et al., 2021; Prosdocimi et al., 2017). Thus, SfM data processing is limited to occasions, where licensed software is affordable and available (Jiang et al., 2020). On the other hand, freely available software like VisualSfM exists (Wu, 2011):

Thus, the question arises, whether image analysis using freely available software is reasonable. Also, it still remains a challenge to distinguish between rainfall-erosion induced soil settlement and soil redistribution, deposition, or loss, when applying SfM-photogrammetry. The objective was to test a photogrammetric Structure-from-Motion (SfM) technique for the mm-scale mapping of the soil surface micro-topography that allows monitoring without special equipment and with widely available cameras. We compare two methods for the consideration of soil settlement via bulk density changes. Specific tasks were (i) to test a photogrammetric Structure-from-Motion (SfM) technique for the mm-scale mapping of the soil surface micro-topography that allows monitoring without special equipment and with widely available cameras and (ii) to determine soil re-consolidation after soil tillage and sowing to analyze the effect of bulk density changes on the predicted soil mass movement. In addition (iii), the changes in soil surface roughness, which can be used as parameter for soil erosion models, was determined from micro-topographical changes. For the present study, data from an experimental soil erosion hillslope were used. Observations were carried out at the same experimental field and for the same period under identical soil and crop management conditions.

2.3   Materials and Methods

2.3.1   Experimental hillslope and SfM plots

The experimental hillslope (Fig. 2.1a) of the Leibniz-Centre of Agricultural Landscape Research (ZALF) in Müncheberg is located in the north-eastern part of Germany (52.6°N, 14.3°E; Deumlich et al., 2017). The site is characterized by an average annual precipitation of 547 mm (1992-2019) and an annual mean temperature of 9.3 °C (https://open-research-data.zalf.de/default.aspx, DWD-ZALF Weather Station, March, 2020). The soils along the hillslope are mostly Luvisols that developed from coarse-textured glacial sediments; the topsoil consists of loamy to silty sands with about 3% clay (<0.002 mm), 16% silt (0.002-0.063 mm), 81% sand (0.063-2 mm equivalent particle diameter) and about 6 g/kg of organic carbon (Deumlich et al., 2017). The arable field of the south-east exposed hillslope (length: 53.5 m, width; 6 m) ends at the footslope in tinplate funnel for runoff and sediment collection (Fig. 2.1a & b). Cultivation was carried out together with the sowing of corn (*Zea Maize*, L.) with a grubber-drill combination machine on April 26, 2018 (row spacing was 0.75 m); fertilizer was mechanically applied eight days later.

The automated runoff station at the footslope of the hillslope consists of a funnel-shaped runoff collector (Fig. 2.1b, 1), a system of pipes and channels for distributing runoff water and sediments (Fig. 2.1b, 2), a Coshocton-type sampler for splitting the runoff (Fig. 2.1b, 3) with a subsurface installed automated sample collector with plastic bottles on a turntable, a runoff tank at ground level (Fig. 2.1b, 4), for registration of the total amount of surface runoff, and a Hellmann rain gauge (Fig. 2.1b, 5); the small meteorological tower was to measure wind speed, in 20, 50, 100 and 400 cm above the surface.
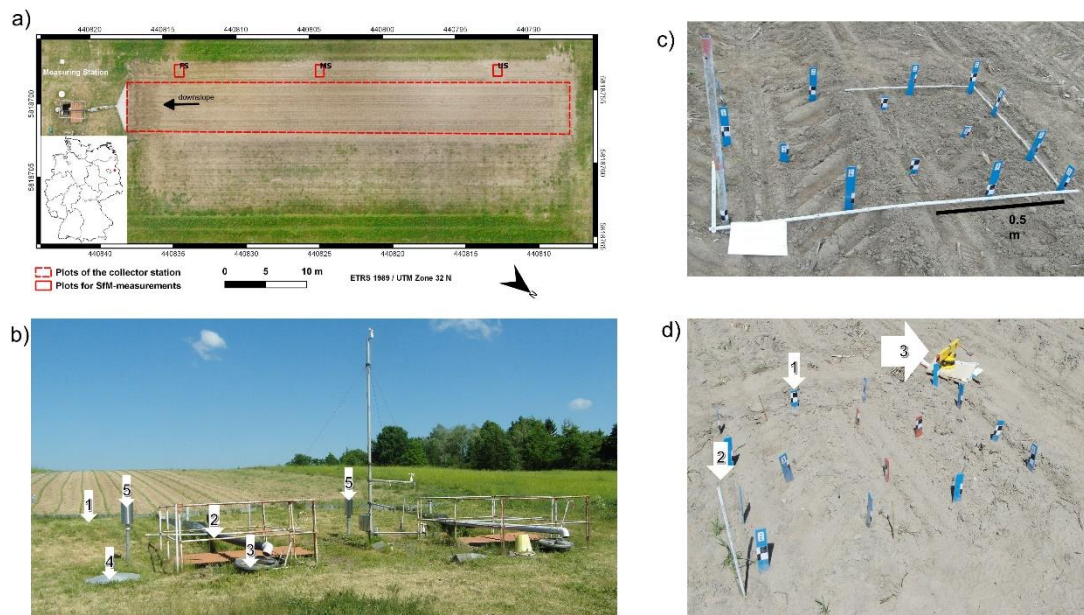
Figure 2.1: (a) Location of the erosion measurement hillsite in Germany (bottom left inlet) and photo image of the hillslope with the collector stations and SfM-plots at the three slope positions: FS (footslope), MS (middle slope), and US (upper slope); (b) Set-up of the erosion measurement station: (1) V-shaped sediment collector, (2) Venturi channel system, (3) sample splitting device, (4) tank, (5) rain gauge; (c) Experimental set-up for the assessment of soil erosion with SfM at the footslope (FS); (d) Referencing of the GCPs (1) with folding rule (2) and laser level (3).

The plots for structure-from-motion (SfM) photogrammetry were installed on May 3, 2018, at the upper slope (US), middle slope (MS), and footslope (FS) in north-western direction on an identically-tilled area next to the large hillslope-plot (Fig. 2.1a). Since soil erosion rates differ according to slope angle (e.g., Quan et al., 2020) these three plots were chosen for representing the different angles from 3° to 6° present at the hillslope. The potential flow lines at the soil surface of the hillslope runoff experiment determined from a digital elevation model (GlobalMapper 19.0, LiDAR, 2018, resolution: 1.2 cm x 1.2 cm, see Appendix A2.1) indicated that the SfM plots are not directly connected to the runoff collector at the footslope. The SfM plot size of 1 m length and 1.5 m width was selected such that all surface features (i.e., wheel track, non-compacted region, and 2 rows of corn) were included (Fig. 2.1c) and the area was small enough to achieve mm-resolution due to SfM-processing. The distance between plots at footslope (FS) and MS was 16 m, and between plots at FS and US it was 38 m (Fig. 2.1a). Replicates for the plots could not be identified at this field and were not required since the 3 plots at major hillslope positions could already sufficiently demonstrate the applicability of the SfM-technique and comparison of methods for soil settlement correction. The plots were marked by specially labelled sticks with black-and-white markers for ground control (GC) points (Fig. 2.2). Sticks were driven into the ground down to at least 30 cm depth to ensure that their position

was not affected by topsoil porosity changes. Each SfM plot received 15 sticks with GC markers, from which 3 or 4 were placed at the sides and 4 sticks were placed inside of the plot with the GC markers showing in different directions (Fig. 2.1c). The local coordinates of the GC points were determined by using a ruler and a laser level (Einhell Bavaria BLW 400) relative to a reference point at the bottom left corner of each plot (Fig. 2.1d, 2); UTM coordinates were obtained with GPS (Trimble Geo 7X, Handheld GNSS System, accuracy: 0.5-1.0 m) for reference points to determine the position of plots along the hillslope.
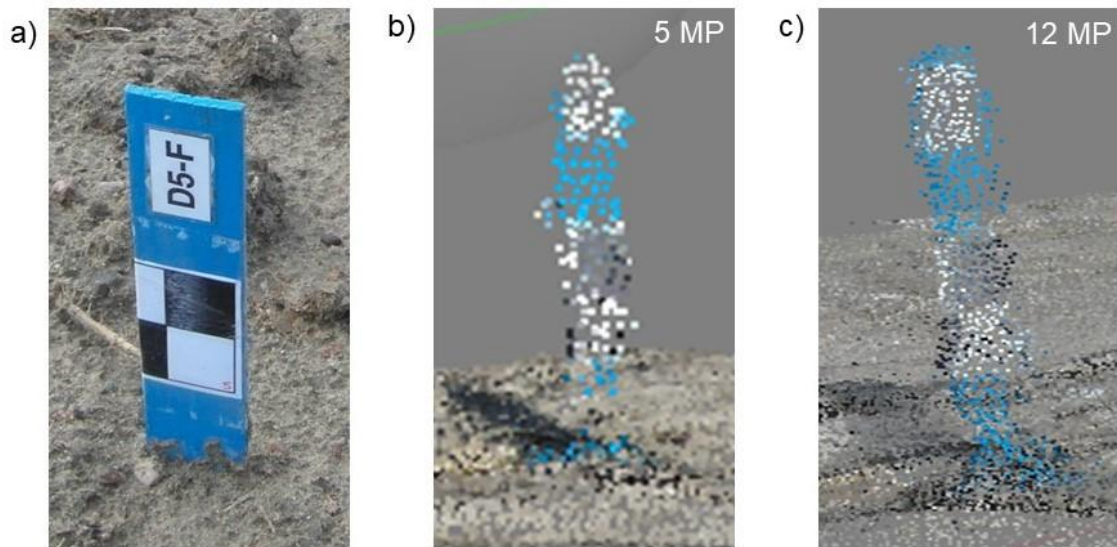
Figure 2.2: a) Example photo of a ground control point (GCP) at the plot surface and point clouds generated by photos taken with a resolution of b) 5 MP and c) 12 MP.

During the observation period from May 3 to May 16, 2018, two relevant rainfall events occurred on May 3 (5.8 mm) and May 15 (14.4 mm), the latter rain had the highest rain energy (311.5 J m^{-2}) and erosivity (EI30) of 6 MJ mm ha^{-1} h^{-1} in terms of the maximal 30-min rain intensity (I30). The cumulative rainfall energy E of both events amounted to 406 J m^{-2}.

The bulk density, ρ_b (kg m^{-3}) was determined gravimetrically using 100 cm³ intact soil cores (cylindrical steel cylinders of 5 cm height) by oven drying at 105 °C for about 3 days. Samples were collected before the SfM measurements (May 3) and after the heavy rainfall (May 15) from the 1 to 6 cm soil depth related to the local surface elevation assuming that the value is valid initially after cultivation for most of the topsoil. The top 1 cm of soil could not be sampled without disturbance and was discarded. Since core sampling was destructive, we selected a region outside and downhill of the SfM plots for the sampling. Thus, the plot surface for SfM measurements remained intact and that the potential

surface runoff from uphill was not affected by any disturbances of the soil surface. In each field campaign, 6 core samples were taken beneath each SfM plot, of which 3 samples were from the intact cultivated area and 3 soil cores from the area compacted by tractor wheels to capture the variability of soil bulk density related to visible soil structures of the plot (Fig. 2.1c). The number of bulk density samples was limited because of limited soil area in the close vicinity of the SfM-plots that should remain intact for subsequent sampling and runoff observations. Note that each core sampling led to significant disturbance of the intact soil next to the plots. Also, the soil of the larger hillslope measurements should remain intact, thus only a relatively small area for bulk density sampling was available.

The bulk density after the rainfall event on May 15 was alternatively determined from the estimated porosity φ (t) (Linden and van Doren, 1987) as:

$$\varphi = \varphi_i - (\varphi_i - \varphi_c)\left(1 - e^{(-aP - bE)}\right) \tag{2.1},$$

where φ_i is the initial porosity, φ_c the final porosity of the re-consolidated soil, P [mm] is the amount of rainfall during the event and the cumulative rainfall energy E [J cm^{-2}]. The bulk density ρ_b is obtained by

$$\rho_b = (1 - \varphi) * \rho_s \tag{2.2},$$

where ρ_s is the density of the solid particles. The parameters for Eqn. 2.1 and 2.2 are defined in Tab. 2.1. Parameters "a" and "b" in Eqn. 2.1 were fitted manually. The optimization was based on the lowest root-mean-square-error (RMSE) in the mean between the measured and the calculated bulk densities inside and outside the tractor lane in the upper-, middle- and footslope.

Table 2.1: Original and adapted parameters for Eqn. 2.1: amount of rainfall P, cumulative rainfall energy E, density of solid particles ρ_s, final bulk density $\rho_{b,c}$, final porosity φ_c, original and adapted parameters a and b and root-mean-square-error RMSE of the final measured and modelled bulk density; TL: Tractor lane

	P	E	ρ_s	$\rho_{b,c}$	φ_c	a_{orig}	b_{orig}	a_{adap}	b_{adap}	RMSE
	[mm]	[J cm^{-2}]	[kg m^{-3}]	[kg m^{-3}]	[]	[]	[]	[]	[]	[kg m^{-3}]
within TL	20.2	0.0406	2650	1620	0.39	0.015	1.5	0.02	1.5	75
outside TL				1550	0.42			0.013	1.5	5

2.3.2   SfM-Photogrammetry and image processing

Photo images of the plots for SfM-processing were taken on a daily basis with the compact digital camera SAMSUNG WB750 in approximately 1.5 m distance from the plot's boundaries. The camera has a locked focal length, f, of 4 mm, a maximum aperture of f/3.2 (i.e., a maximum opening width of the objective lens) and a pixel size of 1.49 µm (Samsung, 2011). The DEMs of the soil surface were generated before and after two rainfall events. Each plot was photographed 30– to 50-times from different perspectives to ensure a spatial overlapping of the images of at least 60% as suggested previously (Kaiser et al., 2015; Westoby et al., 2012). There was no need to adjust the camera to similar perspectives or heights for subsequent photo-sessions at different days, since the camera positions were automatically determined during the image processing, and ground control points (GCP) ensured the georeferencing of the 3D-models. This was one of the major advantages of the SfM-photogrammetry in comparison to e.g., laser scanning. A sensor size of 5 Mega Pixel (MP) (2592 x 1944 pixels) was used for the images during the initial period (May 2 to May 14) and a size of 12 MP (4096 x 3072 pixels) for the images taken until May 16. The 12 MP images were downscaled to a pixel sensor size of 5 MP before processing with Adobe Photoshop Elements (Adobe Systems 2018, Adobe Photoshop Elements Version: 15.0 (20160905.m.97630) x64, operation system: Windows 8.1 64-Bit,Version: 8.1). The point cloud obtained with VisualSfM (Fig. 2.2) appeared to have more evenly distributed points, as compared to a point cloud generated from original 5 MP images. This advantage of downscaling the pictures was found throughout the experimental period, such that images were only taken in 12 MP resolution at the end of the observation period.

The image processing was carried out with the freely available software VisualSfM (Wu, 2011); the workflow (Fig. 2.3) depicts the applied software for each of the subsequent steps, starting with the image alignment and the reconstruction of the sparse and the dense point clouds that were combined to 3D point clouds. The sparse point cloud contains all points that are found in three or more pictures (Westoby et al., 2012). The dense point cloud contains additional points that are reconstructed by the application of the CMVS- and PMVS2-algorithms. In VisualSfM, the Scale Invariant Feature Transform (SIFT) was used to identify common points and structures in the images independent of their size, illumination, and rotation. The Bundle Block Adjustment (BBA) carried out non-linear 3D spatial optimization of camera position related to GC points (Fig. 2.1d) to find the common structures on images for generation of a condensed point cloud. The Clustering View for Multi-view Stereo (CMVS) routine divided data obtained with BBA-algorithm in smaller easier to handle point cloud clusters as a first step to aggregate the combined point cloud.

Finally, the Patch-based Multi-view Stereo (PMVS2) routine was applied to independently reconstruct the 3D-spatial data clusters obtained with the CMVS as the second step in point cloud aggregation.

Software	Step of processing
Photoshop Elements	• Downscaling of photos taken with 12 MP to 5 MP
Visual SfM	• Alignment of pictures • Sparse point cloud reconstruction • Dense point cloud reconstruction
MeshLab	• Georeferencing • Removal of vegetation
Cloud Compare	• Estimation of Change Detection Limit (CDL) • DEM generation
QGIS	• DoD generation • Masking of pixels with change value < CDL • Calculation of soil loss

Figure 2.3: Workflow of SfM-photogrammetry data processing.

After the Visual SfM step (Fig. 2.3), georeferencing of the 3D point clouds was carried out by assigning the measured local coordinates to 4 of the reconstructed GC points (Fig. 2.1d) using MeshLab software (Cignoni et al., 2008; Cignoni, 2016). All points resulting from above-ground vegetation (i.e., maize plants) were manually removed in the May 16th surface models (i.e., end of the observation period). The Level of Detection (LoD) was then estimated using CloudCompare software (Cloud Compare 2020, CloudCompare V2, EDF R&D / TELECOM ParisTech (ENST-TSI), Paris 2016) before exporting the DEMs derived from the point clouds to QGIS software (QGIS Development Team, 2018). The DEM generated from images after a rain event was subtracted from that derived from images before the event in QGIS to create a map of the pixel-based changes in soil surface micro-topography (for images of the workflow see Appendix A2.4). These DEMs of temporal Difference (DoD) were corrected for the uncertainty in the determination of the re-location of GC points by assigning a value of zero to all pixel values smaller than the

LoD. Thus, we assumed that uncertainties caused by small differences in referencing the DEMs of two times were negligible. The plot-average changes in soil surface elevation, $\overline{\Delta z}^{\Delta t}$, between two times, $\Delta t = t_2 - t_1$, were obtained from the sum of DoD pixel values, Δz_i, divided by the number of pixels, $N_p = 1,\ldots, i$, as:

$$\overline{\Delta z}^{\Delta t} = \frac{1}{Np} \sum_{i=1}^{Np} \Delta z_i. \tag{2.3}$$

The LoD is defined as the smallest value of change in soil elevation that can actually be detected with SfM without being considered as noise. For the determination of the LoD only those GC points were deployed that were not used for georeferencing. For the LoD different definitions exist in the literature (e.g., Brasington et al., 2003). Here, the LoD between two measurements, Δt, is calculated from the differences of the x-, y-, z- coordinates (isotropic) in all directions as

$$LoD^{\Delta t} = \sqrt{\frac{1}{n*k} \sum_{i=1}^{n} \sum_{j=1}^{k} \left[\left(X_{P_{i,j}}^{t2} - X_{P_{i,j}}^{t1} \right)^2 \right]} \tag{2.4},$$

where *X* denotes the $k = 3$ coordinates of the $n = 4$ GC points ($P_{i,j}$) at times t_1 and t_2.

The component describing surface elevation changes due to consolidation and natural compaction (e.g., by rain impact) was considered by the mean surface elevation changes, $\overline{\Delta z}_{cs}^{\Delta t}$ (subscript *cs* denotes "compacted soil"), obtained from the original ($\bar{z}_{ts}^{t1}$) mean elevation (subscript *ts* means "tilled soil") and the soil bulk density relations before (ρ_b^{t1}) and after the rain event (ρ_b^{t2}) (Hänsel et al., 2016) as:

$$\bar{z}_{cs}^{t2} = \left(\rho_b^{t1} / \rho_b^{t2} \right) * \bar{z}_{ts}^{t1} \tag{2.5a},$$

where the thickness of tilled soil before the rain at t_1 was first assumed to correspond with the height of the soil core of 5 cm. The value of $\bar{z}_{cs}^{t2}$ (here in mm) depends on the thickness of the cultivated soil region, considered to be affected by consolidation; here we compare the effect of a thickness of 5 cm with that of when assuming a value of $\bar{z}_{ts}^{t1}$ of 10 cm. Other values were not considered because major elevation changes due to consolidation during single rain events were expected to occur within the uppermost 0 - 10 cm layer of the topsoil (Rousseva et al., 1988). The two different thickness values were assumed as possible range, since we did not know, whether the bulk density changes occurred in the upper 5 cm of the soil or reached down to 10 cm. Different consolidation was measured outside (2/3 of the plot) and inside the tractor lane (1/3 of the plot). This was accounted for by weighing the soil surface elevation change in the different parts of the plots as:

$$\bar{z}_{cs}^{t2} = \left(\rho_{b,i}^{t1} / \rho_{b,i}^{t2} \right) * \bar{z}_{ts}^{t1} * \frac{1}{3} + \left(\rho_{b,o}^{t1} / \rho_{b,o}^{t2} \right) * \bar{z}_{ts}^{t1} * \frac{2}{3} \tag{2.5b}$$

The subscripts "i" and "o" denote "inside" and "outside" the tractor lane, respectively.

The plot-related mean settlement-induced component of the reduction in soil surface elevation, $\overline{\Delta z}_{cs}^{\Delta t} = (\bar{z}_{cs}^{t2} - \bar{z}_{ts}^{t1})$, was subtracted from the mean changes in surface elevation obtained from either the DoD maps between the two times, $\overline{\Delta z}^{\Delta t}$, Eqn. 2.3, to yield a corrected mean value of surface elevation changes as:

$$\overline{\Delta z}_{cor}^{\Delta t} = \overline{\Delta z}^{\Delta t} + \overline{\Delta z}_{cs}^{\Delta t} \qquad (2.6),$$

where subscript *cor* denotes "corrected".

The fraction of the area of which the soil surface elevation increased, decreased or remained unchanged was calculated for the main soil surface structural areas of the plots. The surface structures inside the tractor lane (in TL), outside the tractor lane (out TL), and the seed row (SR) were defined and manually distinguished according to the visible structures in the DoDs. The DoDs of each plot were reduced to the individual soil surface structure and pixels were classified according to increase (+), decrease (-) and no change (0) in soil height and the number of pixels in each class was summed up. The area fraction of each class of soil surface structural feature was obtained (c.f., Eqn. 2.3) from the sum of pixels divided by the total number of pixels.

2.3.3 Potential errors in data acquisition and processing

Throughout the process of soil loss determination by SfM several errors accumulate: a) GC points were manually levelled, (b) the generation of the dense point clouds in Visual SfM depends on the image quality and leads in case of low quality images to a lower point density causing errors when creating surface models (c) georeferencing errors, and (d) errors in soil loss calculation from soil elevation changes due to natural consolidation.

Here, during the levelling the GC points with the laser level an accuracy of ± 1 mm was achieved. The standard deviation of georeferencing the point clouds in MeshLab and the calculation of the Level of Detection (LoD) in CloudCompare amounts to 0.7 mm. For the bulk density measurements used for the correction of soil settlement, a mean standard deviation for all plots of 70 kg m^{-3} was obtained. This value resulted in an error of 0.5 mm if a 5 cm topsoil layer $\bar{z}_{ts}^{t1}$ and of 1.1 mm if a 10 cm topsoil layer $\bar{z}_{ts}^{t1}$ is assumed (Eqn. 2.5a). Thus, these errors add to a maximal value of 2.2 to 2.8 mm if all sources of possible inaccuracies in data acquisition and processing are considered.

2.3.4   Calculation of soil surface roughness

Soil surface roughness, as an important input for soil erosion models (e.g., Kaiser et al. 2015), was calculated in QGIS by employing the roughness algorithm derived from the GDAL DEM utility (QGIS Development Team 2014). This algorithm derives the roughness from the Terrain Ruggedness Index (TRI) according to Wilson et al. (2007) by averaging the absolute values of the differences in height between a pixel and its 8 neighbors. This algorithm was used because it provided a convenient and quick possibility to characterize morphologic soil surface changes within the plots. It was the only algorithm currently implemented in QGIS to determine soil roughness. In order to obtain an average roughness of the whole plot, the values of all pixels per plot were averaged.

2.4   Results

2.4.1   Soil bulk density

Soil bulk density was initially higher in the tractor lanes (1430 to 1480 kg m^{-3}) than in the soil regions between tractor lanes with 1180 to 1270 kg m^{-3} (Tab. 2.2, for statistical analyses see Appendix A2). Measured soil bulk density increased within the 20 days in most plots, except for the tractor lane regions on the middle and upper slopes; however, this effect of a decrease in soil bulk density was smaller than the standard deviation and negligible. The soil outside of the tractor lanes was generally more compacted at the second date indicated by a density increase of about 80 to 100 kg m^{-3} as compared to the first date and the soil within tractor lanes. On the plot at the footslope position, soil regions in and outside the tractor lanes were similarly more compacted as indicated by a density increase of 70 to 80 kg m^{-3}. According to statistical analysis the bulk density differences between inside and outside the tractor lane were not significant, except for the middle and upper slope on May 2, 2018 (Appendix A2). The predicted bulk density (Eq. 2.1) for the May 22 was similar to the measured bulk density outside the tractor lane. However, modelling showed a stronger increase in soil bulk density inside the tractor lane than the measurements suggested (Tab. 2.2).

Table 2.2: Surface soil (1-6 cm depth) bulk density, ρ_b (kg m^{-3}), for the SfM-plots at the three slope positions determined from samples taken inside and outside of the wheel track of a tractor lane (TL) on May 2 and 3 and on May 22, and differences between the two times, Δ(for statistical significant differences see boxplots in Appendix A2); mean values (MV) and standard deviation (SD) from 3 replicates. TL: Tractor lane

Slope position	TL	May 2 and 3		May 22 (measured)			May 22 (modelled)	
		MV	SD	MV	SD	$\Delta \rho_b$		$\Delta \rho_b$
		ρ_b						
		[kg m^{-3}]						
foot	within	1440	100	1510	110	70	1506	66
	outside	1270	50	1350	50	80	1346	76
middle	within	1480	70	1440	150	-40	1532	51
	outside	1180	40	1280	90	100	1283	100
upper	within	1430	80	1410	60	-20	1500	70
	outside	1250	20	1330	40	80	1331	82

2.4.2   SfM-measurements of surface structural changes and soil loss

The final DoD-maps (Fig. 2.4) show spatially-distributed patterns of increasing (green) and decreasing (red) soil surface elevations. The tractor lanes and the seed rows could be identified more clearly in the individual DEMs provided in the Appendix (Appendix A2.5). For the upper slope position, only relatively small changes in soil surface topography are noticed during the first two days after the installation of the plots (Fig. 2.4a, top). Settlement of the soil can be observed more in the less compacted right part of the plot as compared to the more compacted seed rows and tractor lanes. After twelve days (Fig. 2.4a, centre), the settling of the soil was more pronounced (i.e., more decreasing surface elevations) also in the plot region of the initially more compacted soil. Note that the first leaves of the maize plants could be identified as spots of larger elevation increase along the seed row in the middle of the plot. After the heavy rainfall event on May 15, the increased red spots in the lowest DoD map (Fig. 2.4a, bottom) indicated a larger decrease in soil surface elevation esp. in the less compacted regions of the plot, where more than 80% of the area was subject to soil height loss (Fig. 2.5).
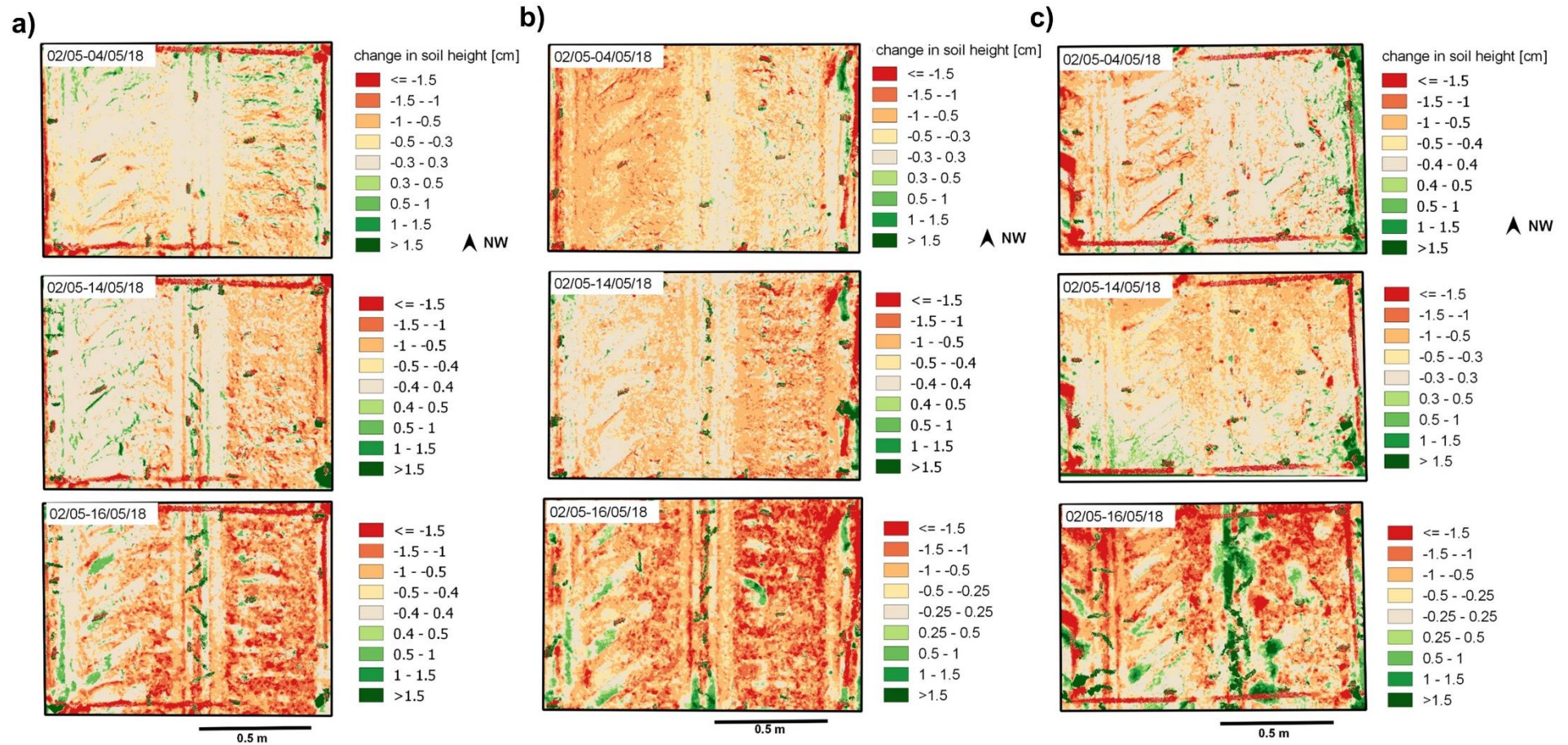
Figure 2.4: Maps of changes in soil surface height (micro-topography) calculated from the SfM-derived DEM's of two dates (i.e., DoD) at the plots of (a) the upper-, (b) the middle-, and (c) the footslope position during the period between May 2 and May 16; see Appendix A2.5 for DEMs.

For the plots at the middle- (Fig. 2.4b) and the footslope (Fig. 2.4c) positions, the changes in soil surface topography are relatively similar during the first period between May 2, 4 and 14 (upper and central rows of the maps in Fig. 2.4). An exception is the plot at the middle slope: the decrease in surface elevation was stronger in the more compacted tractor lane than in the looser region of the plot (Fig. 2.4b, top). Twelve days later, the situation has changed completely: now the loose area shows higher settlement than the tractor lane (90% of the area outside the tractor lane was subject to soil height loss, Fig. 2.5). This might be attributed to the different values in the level of detection, LoD, assigned to the DoDs. Changes in soil surface elevation could be masked by a higher limit used as LoD. On May 16, due to rainfall the soil surface elevation was more strongly decreasing (red spots) than increasing (green spots) especially for the plot at the middle slope (Fig. 2.4b, bottom). Deposition of soil can be observed at the middle slope plot especially at the lower end of the seed row and in the imprints of the tyres. For the plot at the footslope position, the regions with an increase in surface elevation or deposition are largest and oriented along the seed row along the central part (Fig. 2.4c, bottom & Fig. 2.5); for this plot at the footslope, a gradient in surface elevation changes was observed ranging from decreasing elevations (erosion) in the upper to increasing elevations (deposition) in the footslope regions. Red and green spots next to each other, especially for plots at the middle and the bottom slope position (Figs. 4b and 4c, maps at the bottom), indicate a flattening of the soil surface topography due to deposition, of soil particles that were detached at the local peaks for example, within the wheel tire marks.
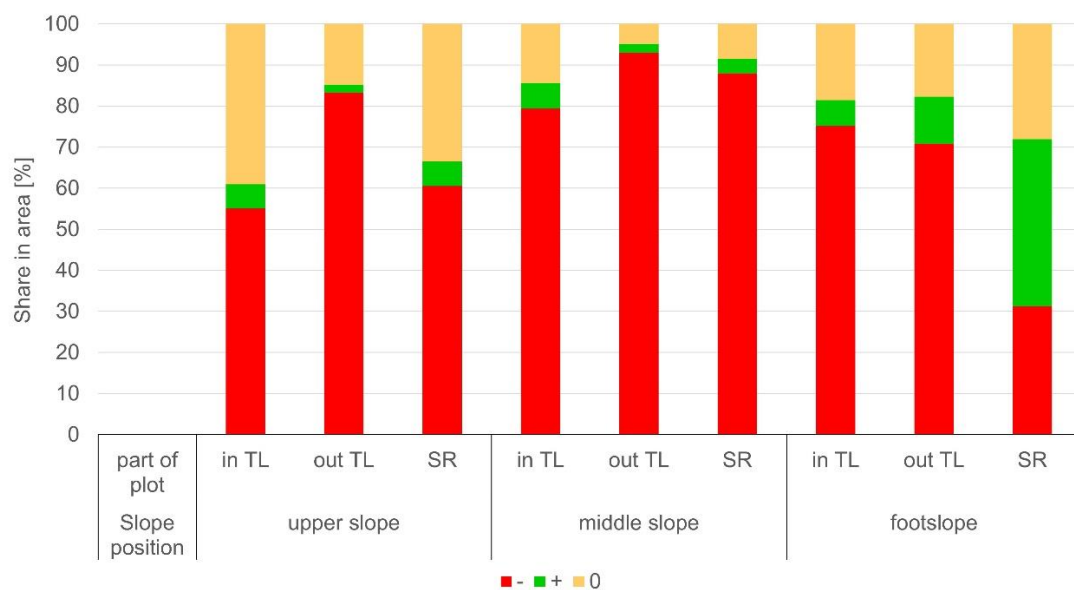
Figure 2.5: Share in area that increased (+), decreased (-) or did not change (0) in the individual soil surface structural sections tractor lane (in TL), outside tractor lane (out TL) and seed row (SR) at the upper, middle and footslope from May 02 to May 16

Between May 02 and 16, the plot at the upper slope position experienced the smallest changes in mean surface elevation. This means that here a larger area of the plot remained at the same surface elevation than at the middle slope and footslope (Fig. 2.5). As observed qualitatively the middle slope had the highest surface area fraction with soil height loss in all soil surface structural regions (>80%). For the footslope, the seed row experienced the most pronounced increase in soil height, since 40% of the seed row area fraction increased in soil height (Fig. 2.5).

The plot-scale averages of the changes in soil surface elevation obtained from the DoD-maps between May 14 and May 16 were all larger as compared to the hillslope-related calculated soil loss of the sediment yield of the collector station (Tab. 2.3). The plot-scale mean elevation changes were all negative except for the plot at footslope position, if considering no soil consolidation and consolidation related to 5 cm topsoil (Fig. 2.6). When consolidation was related to 10 cm topsoil, all plots (upper-, middle- and footslope) showed increase in soil surface elevation, except when no consolidation was accounted for (Fig. 2.6).

Table 2.3: Weighted changes in average soil surface elevation (h), volume (V), and mass (M) at the SfM-plots along the experimental slope between May 2 and A: May 4, B: May 14, and C: May 16; D indicates changes in surface elevation and mass between May 14 and 16 after correction for soil settlement; mass, M, collected at the hillslope erosion station between May 2 and 16 (C) was used to calculate a slope-averaged value of the change in surface elevation (h) over the total hillslope.

Slope position	Compact. depth*	h [10^{-3} m]				V [10^{-3} m^3]				M [kg m^{-2}]			
		A	B	C	D	A	B	C	D	A	B	C	D
upper slope	5 cm	-1.8	-4.6	-3.8	-1.1	-1.7	-4.6	-3.7	-1.8	-2.35	-6.36	-5.12	-1.47
	10 cm	-1.8	-4.6	-1.7	1.0	-1.7	-4.6	-1.7	-0.1	-2.35	-6.36	-2.37	1.29
middle slope	5 cm	-4.5	-4.8	-5.1	-2.2	-5.4	-5.7	-6.2	-3.5	-5.94	-6.51	-7.19	-2.94
	10 cm	-4.5	-4.8	-2.5	0.4	-5.4	-5.7	-3.0	-1.1	-5.94	-6.51	-3.50	0.56
foot-slope	5 cm	-1.7	-3.1	-1.8	3.1	-1.8	-3.1	-1.9	3.0	-2.34	-4.38	-2.59	4.36
	10 cm	-1.7	-3.1	1.0	5.9	-1.8	-3.1	1.0	5.8	-2.34	-4.38	1.37	8.33
Collector Station				-0.07				-22.6				-0.097	
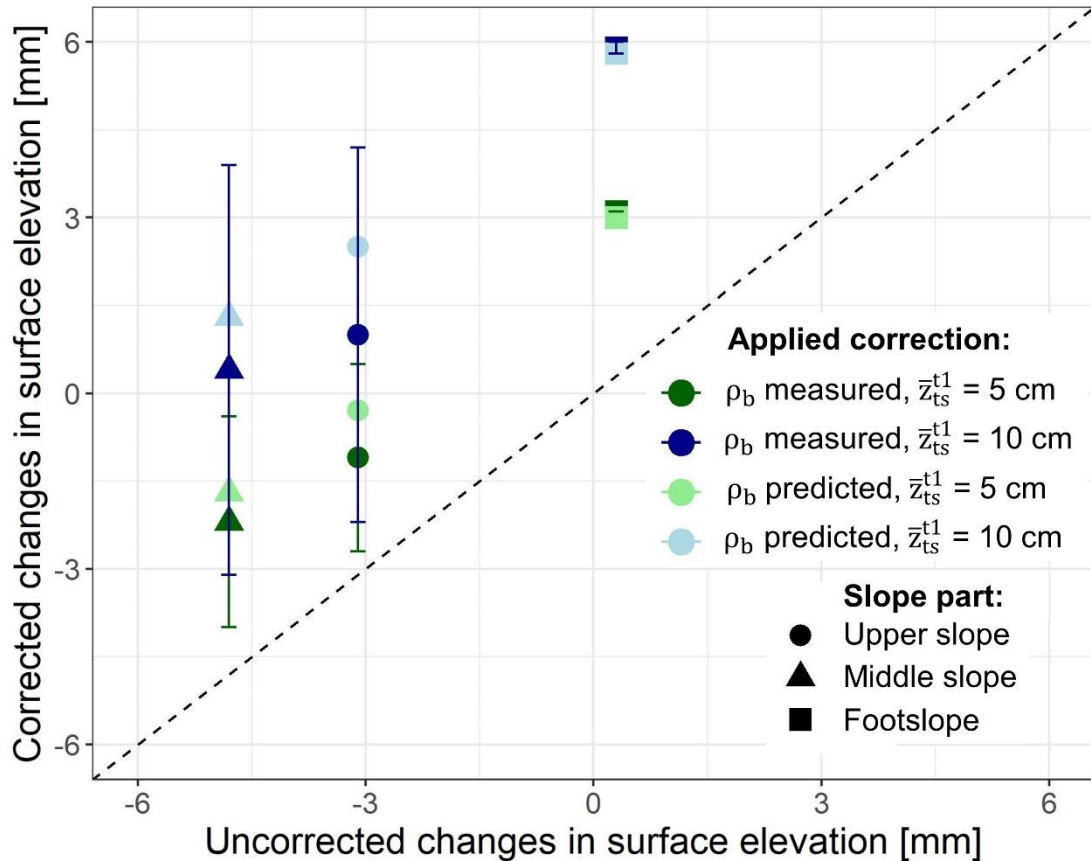
Figure 2.6: Uncorrected vs. corrected soil elevation changes [mm] between May 14 and May 16 in the upper slope, middle slope, footslope. The soil height elevation changes were corrected for consolidation by the measured final bulk density ρ_b assuming a thickness of the tilled soil, $\bar{z}_{ts}^{t1}$, of 5 cm and 10 cm and corrected for consolidation by the predicted final bulk density ρ_b assuming a thickness of the tilled soil, $\bar{z}_{ts}^{t1}$, of 5 cm and 10 cm.

The plot-scale averages of the changes in soil surface elevation depict values between -6 and -2 mm that are dependent on the slope (Fig. 2.7a). One exception is the positive value found for the plot at the bottom slope position indicating predominant deposition during the rain event. The plot at the upper slope (Fig. 2.7a) with the smallest inclination (6%) showed smallest elevation changes (-1.8 mm) but relatively large changes due to consolidation of approx. -5 mm (Tab. 2.3). The plot at the middle slope with 9% inclination experiences the most pronounced surface changes (-2.2 mm) and consolidation (up to -5.4 mm). Although the inclination was largest at the plot at the footslope (11%), only relatively small changes (-1.7 to -3.1 mm) in the mean surface elevation were observed before and deposition (+3 mm) was observed after the rainfall event on May 15 (Tab. 2.3). The plot at the middle slope shows the highest losses in surface elevation in contrast to the plots at the upper- and footslope, which corresponded with the loss in soil volume and soil mass (Tab. 2.3).

The average soil roughness in terms of the Terrain Ruggedness Index (TRI) decreased at all plots from May 2 till May 16 (Fig. 2.7b). The plot at the footslope had the highest initial soil roughness with 2.5 mm, whereas the upper slope had the smallest initial soil roughness (2.2 mm). Throughout the observation period, the footslope position showed the strongest decrease of TRI-values from 2.5 to 1.9 mm, which corresponds to the deposition and levelling of the soil surface that was observed for the plot surface at the footslope position. At middle and upper slope positions, TRI values decreased only by approximately 0.4 mm from 2.3 to 2.0 mm and 2.1 to 1.7 mm. The roughness of the soil surface at the footslope position most gradually decreased (Fig. 2.7b), while at the middle and upper slopes, the surface roughness decreased initially more strongly from May 2 till May 4, remained at the same level till May 15, and decreased again after the rainfall on May 15.
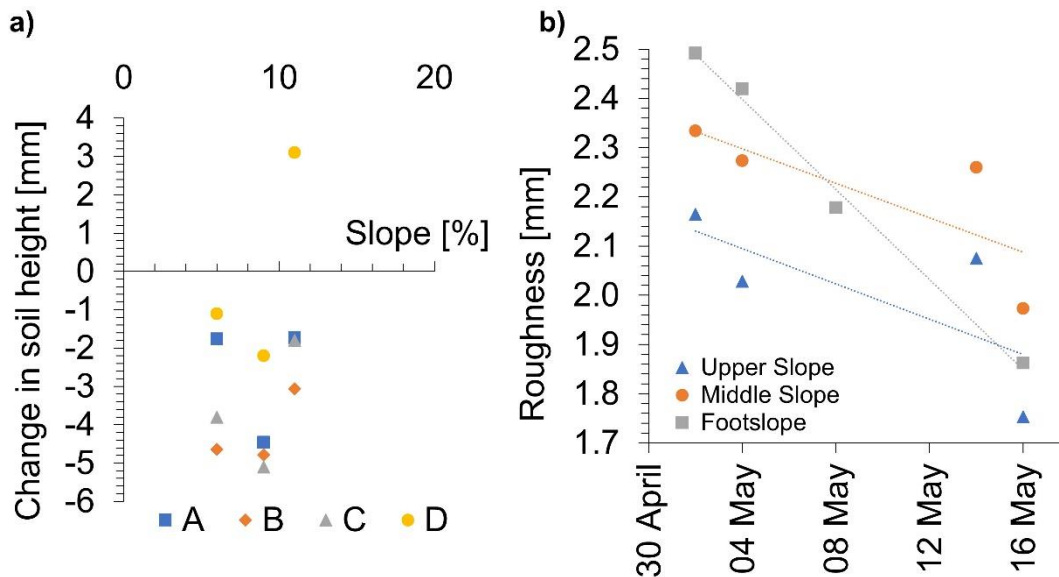
Figure 2.7: (a) Corrected changes in soil elevation assuming a thickness of the tilled soil, , $\bar{z}_{ts}^{t1}$, of 5 cm since May 2 depending on the slope at different times: A – May 4; B – May 14; C – May 16; D – temporal change in soil elevation between May 14 and May 16; (b) Soil roughness change at the upper-, middle- and footslope between May 2 and May 16 (The DEM of the footslope was created at May 8 instead of May 14 since the image quality of the pictures taken on May 14 did not proof to be sufficient to generate a DEM).

2.4.3 Comparison of methods for soil settlement correction and comparison to slope

The subplots for soil erosion assessment with SfM, installed at the upper, middle, and footslope position of the hillslope differed with respect to slope inclination. After correcting the mean soil surface elevation changes of these plots by using predicted bulk density changes, the elevation changes were generally smaller as compared to the changes obtained by using measured bulk density for the correction (Tab. 2.4). Both, measurements and predictions, resulted in an overall reduction in original mean surface elevation of the tilled soil ($\bar{z}_{ts}^{t1}$) for plots at the upper and the middle slopes. However, an increase in soil surface elevation was found for the plot at footslope position when the settlement correction was related to a 5 cm soil layer. When bulk density changes were assumed to affect a soil layer of 10 cm thickness, a net deposition was obtained for plots at the upper, middle, and footslope positions. Here, the predictions of the soil settlement correction led to larger values of the surface elevation changes as compared to the measurements (Tab. 2.4).

Table 2.4: Slope length (L) and area (A) of the different slope sections (in m² and % of the total slope) of the total slope together with weighted changes in average soil surface elevation (h) (according the share of each slope part of in the total slope) corrected by the measured and predicted soil bulk density (Eqn. 2.1) at the SfM-plots along the experimental slope between May 14 and 16 after correction for soil settlement; $\bar{z}_{ts}^{t1}$ denotes the applied correction value for the compaction depth of 5 and 10 cm; the weighted sum describes the average loss in soil elevation derived from the SfM-plots extrapolated to the total slope and weighted by the different area sizes.

| | L | A | | h [10^{-3} m] | | | |
| | [m] | [m²] | [%] | measured | | Predicted | |
$\bar{z}_{ts}^{t1}$	/	/	/	5 cm	10 cm	5 cm	10 cm
upper slope	28.5	171	54	-1.1	1.0	-0.3	2.5
middle slope	14.5	87	27	-2.2	0.4	-1.7	1.3
footslope	10	60	19	3.1	5.9	3.0	5.8
Weighted sum (US, MS, FS)				-0.60	1.74	-0.07	2.79
Total slope	53	318	100	-0.07			

Although the soil loss observed by SfM at the smaller plots cannot quantitatively be compared to soil loss by surface runoff and erosion at larger slopes (Parsons, 2019, see discussion 4.4), an extrapolation may be useful to check the plausibility range of the SfM data and evaluate ranges and relative soil masses quantified with the SfM method. Still, for comparing subplot information with that of the hillslope, the soil mass changes determined at the SfM-plots needed to be weighted, here according to the upper-, middle-, and footslope area fractions (Tab. 2.4). Note that the typical relations between slope

lengths and relative sizes of slope sub-divisional areas (Jha et al., 2015) were modified by increasing the length of the footslope sub-division from 3 to 10 m and proportionally reducing the length of the middle slope to account for the observation of deposition along this 10 m slope region (Appendix A2.3). The soil loss measured in the collector station was in the range of SfM-measurements corrected by using the predicted bulk density changes according to Linden and van Doren (1987) when assuming a topsoil height of 5 cm. With the correction based on measured bulk density values related to a 5 cm thick topsoil, the soil loss extrapolated by the SfM-technique for the total slope was 8- to 9-times that observed at the hillslope station (Tab. 2.4). The correction of the soil settlement applied to a topsoil height of 10 cm led to an increase in soil surface elevation after the erosion event for all plots (Fig. 2.6 and Tab. 2.4).

2.5 Discussion

2.5.1 Soil loss and surface structural changes obtained by SfM

Soil surface structural changes due to raindrop impact could be quantified with the SfM-technique at the three hillslope positions. The plot located near the footslope received more sediments than were eroded (Tab. 2.3) because in these regions, any surface runoff coming from upper slope regions is saturated with sediments and cannot take up more soil particles (Schmidt, 1996). For plots at middle and upper slope positions, surface runoff only locally affected the surface roughness (Fig. 2.7b, Appendix A2.5) and probably generated not sufficient kinetic energy for initiating larger-scale erosion under the present conditions and slope angles. The observed internal distribution of the soil within one SfM-plot with similar slope angle (10%) was also found in the study by Quan et al. (2020) with soil elevation increasing at the lower end of the plot. Kaiser et al. (2018) and Hänsel et al. (2016) reported similar local redistribution of soil from the exposed higher elevated plot regions into the depressions and lower elevated regions.

Between May 02 and 16, the plots showed a decrease in soil surface elevation in all surface structural units (Fig. 2.5). In the plot at upper slope position, larger area fractions remained unaffected from these changes than in the plots at middle and footslope positions. Since soil erosion is unlikely to occur so far upslope due to insufficient kinetic energy of the runoff (Schmidt 1996) and according to visual inspection, soil consolidation must have been the main reason for soil surface elevation reduction. Note that the area fraction for which elevation changes were observed with SfM for the soil surface structural regions is not directly related to the amount of soil erosion in the plot. Relatively small areas of the plot with relatively large elevation changes could have affected the overall plot scale mass changes.

The decline in soil surface roughness (Fig. 2.7b) could be attributed to the collapse of soil aggregates. Mechanisms for aggregate breakdown have been attributed to contractive forces of water in menisci between soil particles (Hartge et al., 2014), the decrease in structural stability of soil aggregates during wetting (Bergsma und Valenzuela, 1981), the destruction of soil aggregates by rain drop impact (Bolt und Koenigs, 1972) and the subsequent transport of smaller particles into larger pores (Schmidt, 1988). The soil surface maps at the footslope position with the strongest decrease in soil roughness supported the observation that soil particles were deposited in the local depressions leading to a levelling of the profile (Figs. 4, 5, and 7b). The small effect of slope inclination on soil surface dynamics was probably related to relatively high infiltration rates at the upper and middle slope positions, and the focused surface runoff on cultivation-induced features such as wheel tracks and plant rows (Appendix A2.3).

2.5.2   Comparison and limitations of techniques for soil consolidation estimation

Soil loss estimated by SfM-photogrammetry was smaller when soil consolidation was accounted for either by bulk density measurements or predictions (Eqn. 2.1) according to Linden and van Doren (1987) (Tab. 2.4). This seems more plausible because the overall soil loss of the total slope was significantly smaller than that derived from plot-scale data (Tab. 2.3). Soil consolidation needs to be considered as an important source for soil elevation decrease of a freshly cultivated soil in temperate climate zones (Schmidt, 1988).

When comparing the measurement with the prediction of soil settlement correction, similar trends for the overall change in soil height of the plots can be found: A decrease in soil height for the upper and middle slopes and increase (i.e., net deposition) for the footslope position (Tab. 2.4). The prediction method has the advantage that no elaborate bulk density measurements are needed after each precipitation event. Measurement errors of the soil bulk density can lead to larger errors, so a lot of soil samples would need to be taken and larger soil areas need to be disturbed for the sampling. In case of the bulk density prediction, however, site-specific characteristics cannot directly be included in the analysis. Additionally, data of bulk density changes as determined here by core sampling, cannot clearly distinguish between natural soil settlement and erosion or deposition (e.g., Knapen et al., 2008). Both processes might lead to a change in bulk density in addition to natural consolidation due to raindrop impact. An alternative approach in this case would be to determine the bulk density changes in a levelled area (i.e., control plot) that is not subject to soil erosion but only to natural soil consolidation via rainfall. However, this plot would have to be located in the vicinity to the sloped plot, to ensure comparable raindrop impact and soil conditions. To install such a control plot in the field, might be challenging; and could be only tested under simulated rainfall and in the laboratory (e.g., Kaiser et al.

2018). The settlement prediction considers bulk density changes only due to raindrop impact for levelled plots and thus predicts final bulk densities without the impact. The advantage of the prediction over the direct measurements is that the model could be calibrated by fitting parameters "a" and "b" to site-specific bulk density changes observed when erosion impact could be excluded.

2.5.3 Limitations caused by SfM-data processing

Besides deviations caused by conditions in the field, uncertainties might occur also throughout the SfM-processing due to low precision in georeferencing of the 3D point clouds in MeshLab. Because of limited computational power, dense point clouds were not generated for every single part of the plots. In most cases, the centre of the GCPs was not exactly represented by a single point but was rather located in between two points. Consequently, throughout the georeferencing process only one of the points located a certain distance away from the actual GCP centre could be chosen for georeferencing leading to a deviation from the real coordinates. The described georeferencing error has been accounted for by considering a detection level, LoD (Fig. 2.7, legends).

Between the points of the 3D point cloud, an interpolation was carried out in areas with a low point density during DEM generation in CloudCompare. This is the case especially in the regions close to the plot boundaries, where the coverage with images was lower than in the plot centre. For every time step, VisualSfM produced different point clouds depending on the photo images. This was also the case, when two 3D models of the same object were generated from a different set of pictures. Hence, for both 3D models, different point clouds existed as a template for the DEM generation so that interpolation between the points was different leading to differences in the DEMs of the same object. This interpolation error increased with the complexity of an object's surface. Since soil surfaces were rather heterogeneous, this error was probably important. A possible solution could be to use pictures with a higher image resolution (Fig. 2.2; i.e., from 5 to 12 MP). Unfortunately, VisualSfM software was unable to process such highly resolved data. By the use of downscaled pictures from 12 MP to 5 MP in Photoshop Elements, the point cloud density was not increased but the points were more evenly distributed throughout the point cloud. Other software such as PhotoScan (Agisoft, 2018) would be better able to handle a variable amount of data points (Jiang et al., 2020). However, this software was not available and required more computational power.

2.5.4 Challenges of small-scale erosion quantification by SfM and future needs

The SfM-photogrammetry proved to be a useful tool to observe small scale soil surface micro-topography and structural changes at three plots or subplots along a hillslope. The advantage of our case study carried out in combination with the hillslope erosion experiment was that the same agricultural management was carried out uniformly over the whole field and that the basic conditions, soil, crop, tillage, and weather information could be directly used and compared with the complete hillslope. However, the soil loss found at the SfM-plots could not be related to that measured at the hillslope collector station for several reasons: For a start, the origin of the sediments collected at the footslope is uncertain, and according to the surface flow lines, sediments may have also passed the funneled collector (c.f. Appendix A2.1). It is not clear, where the sediment in the collector station might have come from. Travel distances of particles is finite and small (Parsons et al. 2010), thus the small plots can only estimate local redistribution. Also, the suggested approach to relate soil surface elevation changes of a smaller slope to the average soil surface elevation changes of a larger slope (Tab. 2.4) is dependent on the empirically adjusted slope length among other factors. Thus, this approach is site specific and cannot be transferred to other areas. Similar comparisons of smaller plots to larger slopes (Chaplot and Poesen, 2012) gave considerably higher sediment delivery rates from 1 m^2 plots as compared to hillslope-scale (899 versus 4.3 g m^{-2} y^{-1}). These authors attributed this discrepancy to splash erosion being the dominant sediment detachment and transport mechanism at hillslopes. Martinez et al. (2017) also found lower sediment yields at larger plots (27 m²) as compared to smaller plots (0.7 m²). In contrast, Boix-Fayos et al. (2007) found higher sediment concentrations at larger plots (30 m²) than in 1 m²-sized plots.

Thus, the observed discrepancies between the different soil loss estimation techniques in this study can be attributed to the smaller size of the plots used for the SfM-measurements (1.5 m²) in contrast to the collector station that accumulates the eroded sediment from a 318 m² hillslope. The SfM-plots reveal the local deposition and erosion processes and do not allow estimating processes between plots (Parsons et al., 2010). Any comparison would improve, if DoD maps of the hillslope were generated provided the SfM-technique could be applied to the total area. Unfortunately, the resolution of the DoDs for a larger area would still be too coarse, the identification of effects of rain events on surface structure dynamics is limited (Kaiser et al., 2018). On the other hand, one could separate larger hillslopes into smaller areas (1 to 3 m²) that are each observed in detail with SfM and finally merged into a large DoD maps.

The SfM measurements basically provide quantitative and spatially-distributed information on the surface topography; it is not possible to distinguish between deposition of soil from

uphill and erosion of soil that left the plot and the settlement. Furthermore, the change in the surface micro-topography includes the decline in surface roughness after rain. This may be considered as a kind of local erosion and deposition, which makes it difficult to separate between the deposition from uphill and local processes. The separation between input and output from changes in mean surface elevation requires additional assumptions that could be based on observations at the neighboring hillslope as follows:

Upper slope position: Based on observations it may be assumed that here the deposition from above was negligibly small such that the changes in surface elevation can be explained by runoff soil loss and by settlement.

The soil surface at the middle slope is in a through-flux position and has both deposition from above and soil loss towards downhill positions. Soil settlement could be the main unknown when assuming that lateral inputs equal outputs of soil mass. At the footslope position, there is clearly more deposition than erosion such it is assumed that the surface elevation changes account for net accumulation and some settlement.

Note that the observations do not allow to exactly quantify the rates of the different components of the soil mass changes but we can provide information on potentially relevant limits by making estimates when assuming minimal and maximal range limits from the comparison with the data obtained at the complete hillslope.

2.6   Conclusions

The application of SfM-photogrammetry on a bare soil allowed quantifying differences in soil surface elevation and structure dynamics due to the impact of rainfall, erosion, and consolidation on soils freshly sowed with Maize. Maps of local or micro- topographic changes were generated for plots at three hillslope positions.

The results of testing different soil consolidation rates in form of soil bulk density changes in topsoil layers indicated that it would be necessary to better account for the structure dynamics in the entire topsoil volume when trying to estimate the elevation changes caused by natural consolidation. The results of the comparisons between data and regression approach suggest that the relatively simple regression after calibration can be useful to correct soil surface elevation changes induced by rain for natural soil settlement.

The results of the soil mass balancing of the plots from the difference between SfM surface elevation maps before and after a rain event revealed also uncertainties that resulted from georeferencing and computation limits of the used software.

The SfM technique designed for the non-destructive and repeated monitoring of soil surface structural dynamics under field conditions, provided valuable information on soil

structure parameters such as surface roughness. Improvements could be achieved by using higher resolution images and expanding the SfM-application to the hillslope.

The results suggest that the use of widely available cameras and application of freely available software for processing photos and DEMs is possible. This may stimulate the application and monitoring of erosion-affected soil surface changes in many arable soil landscapes and regions with limited accessibility. Further improvements of the standardized application, the accuracy, and the calibration of empirical bulk density models are still necessary.

2.7   Acknowledgments

2.8   References

AdobeSystems. Adobe Photoshop Elements., Online available https://www.adobe.com/de/products/photoshop-elements.html, Access date: 19/10/2018

Agisoft (2018). PhotoScan. Online available https://www.agisoft.com/, Access date: 21/03/2020

Ahuja, L.R., Ma, L., Timlin, D.J. (2006). Trans-Disciplinary Soil Physics Research Critical to Synthesis and Modeling of Agricultural Systems. Soil Sci. Soc. Am. J. 70 (2), 311–326. https://doi.org/10.2136/sssaj2005.0207.

Ahuja, L.R., K.W. Rojas, J.D. Hanson, M.D. Shaffer, and L. Ma. (ed.) (2000). Root Zone Water Quality Model: Modeling management effects on water quality and crop production. Water Resources Pub., LLC, Highland Ranch, CO.

Bendig, J., Bolten, A., & Bareth, G. (2013). UAV-based Imaging for Multi-Temporal, very high Resolution Crop Surface Models to monitor Crop Growth Variability: Monitoring des Pflanzenwachstums mit Hilfe multitemporaler und hoch auflösender Oberflächenmodelle von Getreidebeständen auf Basis von Bildern aus UAV-Befliegungen. Photogrammetrie - Fernerkundung - Geoinformation. (6), 551–562. Retrieved from https://kups.ub.uni-koeln.de/20608/

Bergsma, E., Valenzuela, C.R. (1981). Drop testing aggregate stability of some soils near Merida, Spain. Earth Surface Processes and Landforms 6, 309–318.

Boardman, J. (2006). Soil erosion science: Reflections on the limitations of current approaches. CATENA, 68(2-3), 73–86. https://doi.org/10.1016/j.catena.2006.03.007

Boix-Fayos, C., Martínez-Mena, M., Arnau-Rosalén, E., Calvo-Cases, A., Castillo, V., & Albaladejo, J. (2006). Measuring soil erosion by field plots: Understanding the sources of variation. Earth-Science Reviews, 78(3-4), 267–285. https://doi.org/10.1016/j.earscirev.2006.05.005

Boix-Fayos, C., Martínez-Mena, M., Calvo-Cases, A., Arnau-Rosalén, E., Albaladejo, J., & Castillo, V. (2007). Causes and underlying processes of measurement variability in field erosion plots in Mediterranean conditions. Earth Surface Processes and Landforms, 32(1), 85–101. https://doi.org/10.1002/esp.1382

Bolt, G.H., Koenigs, F.F. (1972). Physical and chemical aspects of the stability of soil aggregates. Ghent Rijksfac Landbouwetensch Meded.

Borrelli, P., Robinson, D. A., Fleischer, L. R., Lugato, E., Ballabio, C., Alewell, C., . . . Panagos, P. (2013). An assessment of the global impact of 21st century land use change on soil erosion. Nature Communications, 8(1), 2013. https://doi.org/10.1038/s41467-017-02142-7

Brasington, J., Langham, J., & Rumsby, B. (2003). Methodological sensitivity of morphometric estimates of coarse fluvial sediment transport. Geomorphology, 53(3-4), 299–316. https://doi.org/10.1016/S0169-555X(02)00320-3

Chaplot, V., & Poesen, J. (2012). Sediment, soil organic carbon and runoff delivery at various spatial scales. CATENA, 88(1), 46–56. https://doi.org/10.1016/j.catena.2011.09.004

Cignoni, P. (2016). MeshLab: an Open-Source Mesh Processing Tool. Online available: http://www.meshlab.net/, Access date: 29/04/2018

Cignoni, P., Callieri, M., Corsini, M., Dellepiane, M., Ganovelli, F., Ranzuglia, G. (2008). MeshLab: an Open-Source Mesh Processing Tool, in: Eurographics Italian Chapter Conference. The Eurographics Association.

CloudCompare V2., Edition 2.7.0, Online available: http://www.cloudcompare.org., Access date: 28/04/2018

Deumlich, D., Jha, A., & Kirchner, G. (2017). Comparing measurements, 7Be radiotracer technique and process-based erosion model for estimating short-term soil loss from cultivated land in Northern Germany. Soil and Water Research, 12(No. 3), 177–186. https://doi.org/10.17221/124/2016-SWR

Di Stefano, C., Ferro, V., Palmeri, V., & Pampalone, V. (2017). Measuring rill erosion using structure from motion: A plot experiment. CATENA, 156, 383–392. https://doi.org/10.1016/j.catena.2017.04.023

Eltner, A., Baumgart, P., Maas, H.-G., Faust, D. (2015). Multi-temporal UAV data for automatic measurement of rill and interrill erosion on loess soil. Earth Surf. Process. Landforms 40, 741–755. 10.1002/esp.3673.

Eltner, A., Kaiser, A., Abellan, A., Schindewolf, M. (2017). Time lapse structure-from-motion photogrammetry for continuous geomorphic monitoring. Earth Surf. Process. Landforms 42, 2240–2253. 10.1002/esp.4178.

Eltner, A., Kaiser, A., Castillo, C., Rock, G., Neugirg, F., Abellán, A. (2016). Image-based surface reconstruction in geomorphometry – merits, limits and developments. Earth Surf. Dynam. 4, 359–389. 10.5194/esurf-4-359-2016.

García-Ruiz, J. M., Beguería, S., Nadal-Romero, E., González-Hidalgo, J. C., Lana-Renault, N., & Sanjuán, Y. (2015). A meta-analysis of soil erosion rates across the world. Geomorphology, 239(1–2), 160–173. https://doi.org/10.1016/j.geomorph.2015.03.008

Hänsel, P., Schindewolf, M., Eltner, A., Kaiser, A., & Schmidt, J. (2016). Feasibility of High-Resolution Soil Erosion Measurements by Means of Rainfall Simulations and SfM Photogrammetry. Hydrology, 3(4), 38. https://doi.org/10.3390/hydrology3040038

Hartge, K.H., Horn, R., Bachmann, J., Peth, S. (2014). Einführung in die Bodenphysik: Mit 24 Tabellen. 4th ed., Stuttgart: Schweizerbart.

Haubrock, S.-N., Kuhnert, M., Chabrillat, S., Güntner, A., & Kaufmann, H. (2009). Spatiotemporal variations of soil surface roughness from in-situ laser scanning. CATENA, 79(2), 128–139. https://doi.org/10.1016/j.catena.2009.06.005

James, M. R., & Robson, S. (2012). Straightforward reconstruction of 3D surfaces and topography with a camera: Accuracy and geoscience application. Journal of Geophysical Research: Earth Surface, 117(F3), n/a-n/a. https://doi.org/10.1029/2011JF002289

Jha, A., Schkade, U., & Kirchner, G. (2015). Estimating short-term soil erosion rates after single and multiple rainfall events by modelling the vertical distribution of cosmogenic 7Be in soils. Geoderma, 243-244, 149–156. https://doi.org/10.1016/j.geoderma.2014.12.020

Jiang, S., Jiang, C., & Jiang, W. (2020). Efficient structure from motion for large-scale UAV images: A review and a comparison of SfM tools. ISPRS Journal of Photogrammetry and Remote Sensing, 167(7), 230–251. https://doi.org/10.1016/j.isprsjprs.2020.04.016

Kaiser, A., Neugirg, F., Schindewolf, M., Haas, F., & Schmidt, J. (2015). Simulation of rainfall effects on sediment transport on steep slopes in an Alpine catchment. Proceedings of the International Association of Hydrological Sciences, 367, 43–50. https://doi.org/10.5194/piahs-367-43-2015

Kaiser, A., Erhardt, A., & Eltner, A. (2018). Addressing uncertainties in interpreting soil surface changes by multitemporal high-resolution topography data across scales. Land Degradation & Development, 29(8), 2264–2277. https://doi.org/10.1002/ldr.2967

Knapen, A., Poesen, J., & Baets, S. D. (2008). Rainfall-induced consolidation and sealing effects on soil erodibility during concentrated runoff for loess-derived topsoils. Earth Surface Processes and Landforms, 33(3), 444–458. https://doi.org/10.1002/esp.156

Laburda, T., Krása, J., Zumr, D., Devátý, J., Vrána, M., Zambon, N., . . . Dostál, T. (2021). SfM-MVS Photogrammetry for Splash Erosion Monitoring under Natural Rainfall. Earth Surface Processes and Landforms, 46(5), 1067–1082. https://doi.org/10.1002/esp.5087

Linden, van Doren Jr, D. M. (1987). Simulation of interception, surface roughness, depression storage, and soil settling. In M. J. Shaffer & W. E. Larson (Eds.), Conservation Research Report: 34-1. NTRM: A Soil Crop Simulation Model for Nitrogen, Tillage, and Crop-Residue Management (90-93).

Martinez, G., Weltz, M., Pierson, F. B., Spaeth, K. E., & Pachepsky, Y. (2017). Scale effects on runoff and soil erosion in rangelands: Observations and estimations with predictors of different availability. CATENA, 151, 161–173. https://doi.org/10.1016/j.catena.2016.12.011

Martinez-Agirre, A., Álvarez-Mozos, J., Milenković, M., Pfeifer, N., Giménez, R., Valle, J. M., & Rodríguez, Á. (2020). Evaluation of Terrestrial Laser Scanner and Structure from Motion photogrammetry techniques for quantifying soil surface roughness parameters over agricultural soils. Earth Surface Processes and Landforms, 45(3), 605–621. https://doi.org/10.1002/esp.4758

Meinen, B. U., & Robinson, D. T. (2020). Where did the soil go? Quantifying one year of soil erosion on a steep tile-drained agricultural field. The Science of the Total Environment, 729, 138320. https://doi.org/10.1016/j.scitotenv.2020.138320

Micheletti, N., Chandler, J. H., & Lane, S. N. (2015). Investigating the geomorphological potential of freely available and accessible structure-from-motion photogrammetry using a smartphone. Earth Surface Processes and Landforms, 40(4), 473–486. https://doi.org/10.1002/esp.3648

Nadal-Romero, E., Revuelto, J., Errea, P., & López-Moreno, J. I. (2015). The application of terrestrial laser scanner and SfM photogrammetry in measuring erosion and deposition processes in two opposite slopes in a humid badlands area (central Spanish Pyrenees). SOIL, 1(2), 561–573. https://doi.org/10.5194/soil-1-561-2015

Nouwakpo, S. K., Weltz, M. A., & McGwire, K. (2016). Assessing the performance of structure-from-motion photogrammetry and terrestrial LiDAR for reconstructing soil surface microtopography of naturally vegetated plots. Earth Surface Processes and Landforms, 41(3), 308–322. https://doi.org/10.1002/esp.3787

Parsons, A. J. (2019). How reliable are our methods for estimating soil erosion by water? The Science of the Total Environment, 676, 215–221. https://doi.org/10.1016/j.scitotenv.2019.04.307

Parsons, A. J., Wainwright, J., Fukuwara, T., & Onda, Y. (2010). Using sediment travel distance to estimate medium-term erosion rates: a 16-year record. Earth Surface Processes and Landforms, 35(14), 1694–1700. https://doi.org/10.1002/esp.2011

Pimentel, D., & Burgess, M. (2013). Soil Erosion Threatens Food Production. Agriculture, 3(3), 443–463. https://doi.org/10.3390/agriculture3030443

Prosdocimi, M., Burguet, M., Di Prima, S., Sofia, G., Terol, E., Rodrigo Comino, J., . . . Tarolli, P. (2017). Rainfall simulation and Structure-from-Motion photogrammetry for the analysis of soil water erosion in Mediterranean vineyards. The Science of the Total Environment, 574, 204–215. https://doi.org/10.1016/j.scitotenv.2016.09.036

Quan, X., He, J., Cai, Q., Sun, L., Li, X., & Wang, S. (2020). Soil erosion and deposition characteristics of slope surfaces for two loess soils using indoor simulated rainfall experiment. Soil and Tillage Research, 204, 104714. https://doi.org/10.1016/j.still.2020.104714

QGIS Development Team (2014). QGIS User Guide. https://docs.qgis.org/2.8/en/docs/user_manual/index.html. Accessed 15 July 2019.

QGIS Development Team (2018). QGIS Geographic Information System: Open Source Geospatial Foundation Project.

Rousseva, S.S., Ahuja, L.R., Heathman, G.C. (1988). Use of a surface gamma-neutron gauge for in situ measurement of changes in bulk density of the tilled zone. Soil and Tillage Research 12 (3), 235–251. https://doi.org/10.1016/0167-1987(88)90014-1.

Samsung WB750 (2011). User Manual.

Schmidt, J. (1988). Wasserhaushalt und Feststofftransport an geneigten, landwirtschaftlich bearbeiteten Nutzflächen. Dissertation. na, Berlin. (Water budget and solid matter transport in sloped agricultural areas)

Schmidt, J. (1996). Entwicklung und Anwendung eines physikalisch begründeten Simulationsmodells für die Erosion geneigter landwirtschaftlicher Nutzflächen: 34 Tabellen. Institut für Geographische Wissenschaften, Berlin, ISBN: 3880090629 (Development and application of a physically based simulation model for soil erosion along sloped agricultural areas)

Sutton, P. C., Anderson, S. J., Costanza, R., & Kubiszewski, I. (2016). The ecological economics of land degradation: Impacts on ecosystem service values. Ecological Economics, 129(3), 182–192. https://doi.org/10.1016/j.ecolecon.2016.06.016

Tarolli, P., Cavalli, M., & Masin, R. (2019). High-resolution morphologic characterization of conservation agriculture. CATENA, 172, 846–856. https://doi.org/10.1016/j.catena.2018.08.026

Vinci, A., Todisco, F., Brigante, R., Mannocchi, F., & Radicioni, F. (2017). A smartphone camera for the structure from motion reconstruction for measuring soil surface variations and soil loss due to erosion. Hydrology Research, 48(3), 673–685. https://doi.org/10.2166/nh.2017.075

Westoby, M. J., Brasington, J., Glasser, N. F., Hambrey, M. J., & Reynolds, J. M. (2012). 'Structure-from-Motion' photogrammetry: A low-cost, effective tool for geoscience applications. Geomorphology, 179, 300–314. https://doi.org/10.1016/j.geomorph.2012.08.021

Wilson, M.F.J., O'Connell, B., Brown, C., Guinan, J.C., Grehan, A.J. (2007). Multiscale Terrain Analysis of Multibeam Bathymetry Data for Habitat Mapping on the Continental Slope. Marine Geodesy 30, 3–35. 10.1080/01490410701295962.

Wu, C. (2011). VisualSFM: A Visual Structure from Motion System. Online available: http://ccwu.me/vsfm/, Access date: 29/04/2018

3   Wavelet analysis of soil water state variables for identification of lateral subsurface flow: Lysimeter vs. field data

3.1   Core Ideas

- Soil water content time series in weighing lysimeters are compared with those of field soil.
- Identification of lateral subsurface flow in sloping hummocky soil landscape.
- Deviations of lysimeter from field data depending on infiltration events.
- Wavelet coherency analysis to quantitatively describe temporal patterns of time shifts.

3.2   Abstract

Preferential and lateral subsurface flow (LSF) may be responsible for the accelerated transport of water and solutes in sloping agricultural landscapes; however, the process is difficult to observe. One idea is to compare time series of soil moisture observations in the field with those in lysimeters, where flow is vertically oriented. This study aims at identifying periods of deviations in soil water contents and pressure heads measured in the field and in a weighing lysimeter with the same soil profile. Wavelet coherency analysis (WCA) was applied to time series of hourly soil water content and pressure head data (15-, 32-, 60-, 80-, and 140-cm depths) from Colluvic Regosol soil profiles. The phase shifts and periodicities indicated by the WCA plots reflected the response times to rain events in the same depth of lysimeter and field soil. For many rain events and depths, pressure and moisture sensors installed in the field soil responded earlier than those in the lysimeter. This could be explained by either vertical preferential flow or LSF from upper hillslope positions. Vice versa, a faster response in the lysimeter soil could be indicative for vertical preferential flow effects. Dry weather conditions and data gaps limited the number of periods with elevated soil moisture in 2016–2018, in which LSF was likely to occur. The WCA plots comprise all temporal patterns of time shifts and correlations between large data time series in a condensed form to identify potentially relevant periods for more detailed analyses of subsurface flow dynamics.

3.3 Introduction

Lateral subsurface flow (LSF) or funnel flow describes the lateral redirection and funneling of water caused by textural boundaries in the soil (Gerke, 2006; Guo & Lin, 2018; Hendrickx & Flury, 2001). In agricultural landscapes, this phenomenon can potentially be responsible for accelerated nutrient and pesticide transport from fields into adjacent water bodies like streams and kettleholes leading to a pollution of these ecosystems (Julich et al., 2017; Kahl et al., 2008). In mountainous regions, LSF is also known to promote the development of landslides (Wienhöfer et al., 2011). The LSF process has been studied; for example, in the Shale Hills Catchment (Guo et al., 2018) in a hummocky ground moraine in northeast Germany (Gerke et al., 2010; Filipović et al., 2018), in a soil cover over waste rock (Hopp et al., 2011), in forested hillslopes (Laine-Kaulio et al., 2014), and in an alpine region (Wienhöfer & Zehe, 2014).

The conditions for LSF are inclined soil layers with contrasting hydraulic properties and water saturation in the upper, more permeable soil layer (Laine-Kaulio et al., 2014; Liu & Lin, 2015). Lateral subsurface flow is occurring especially during periods of high soil moisture—for example, those induced by snowmelt (Wilcox et al., 1997). In unsaturated soils, water flow is mainly vertical as predicted by simulations based on the Richards equation (Filipović et al., 2018). Only if the soil water pressure head approaches a value of zero and capillary forces become negligible—for example, near impeding layers and less conductive soil horizons—the gravitation-driven LSF may occur (Lu et al., 2011; Lv et al., 2013). However, a vanishing of capillary forces does not necessarily mean that all soil pores are water saturated. The relation between pressure head and water content (i.e., water retention function) is not a unique and single function; it is hysteretic and changing with time due to local nonequilibrium processes (Hannes et al., 2016; Herbrich & Gerke, 2017), and it is affected by the spatial heterogeneity of local or pore scale and macroscopic soil properties at pedon and larger spatial scales (Filipović et al., 2019; Guo & Lin, 2018; Lin & Zhou, 2008). These effects may also occur in combination (Dasgupta et al., 2006); for instance, during vertical preferential flow through macropores, local nonequilibrium conditions in the pressure head between macropores and matrix can develop (Gerke, 2006). In such cases, water-saturated pore regions can occur locally where the macropore flow hits an impeding layer and from where lateral flow can be initiated (Newman et al., 2004). These authors also observed that LSF was starting from root macropores in the clay-enriched illuvial subsoil horizon after macropore-centred saturation. Earlier, Sidle et al. (2001) suggested from observations in sloping forest soils that vertical and lateral subsurface preferential flow paths are connected by a network of macropores forming the basis for lateral preferential flow in such sites.

In soil columns and lysimeters, lateral flow is restricted due to the limited size and fixed boundaries at the sides such that macroscopic flow is assumed to be predominantly vertical (Bravo et al., 2020; Wittenberg et al., 2019, 2020). Although macropore-centred saturation (Newman et al., 2004) due to vertical preferential flow can also occur in an intact soil monolith of a lysimeter, lateral water movement remains local and may occasionally lead to water movement along the interface between the soil and the sidewall of the lysimeter (Corwin, 2000). As indicated by two-dimensional flow simulations (Filipović, et al., 2018), water dynamics in a sloping field soil may be assumed to start deviating from that in the same depth of a lysimeter if the soil is approaching pore water saturation at some point in the flow domain. It is likely to assume that with the beginning of lateral flow in the field, the pressure head increase will be limited at uphill positions while the increase in soil water content (SWC) will continue at downhill positions during a flow event. In contrast, the SWC in the lysimeter soil will increase faster above impeding horizons than in the field, where lateral downhill movement can reduce the pressure head buildup.

The observation of LSF and especially the detection of the beginning of LSF in the field soil is still a challenge (Lamb et al., 2019; Xie et al., 2019). Preferential flow was identified by comparing soil moisture − depth differences of larger time series according to response sequences (Graham & Lin, 2011; Wiekenkamp et al., 2016). Both vertical and lateral preferential flow pathways have been experimentally studied by various techniques including dye staining, using compounds such as uranine, brilliant blue FCF, or methylene blue (Alaoui et al., 2011; Luo et al., 2019). The dyes can be sprinkled onto the soil surface (Gerke et al., 2015) or injected during infiltration experiments (Nyquist et al., 2018). However, an adequate observation of deep dye patterns requires sectioning the soil along different vertical or horizontal planes, which necessitates extensive effort and destroys the soil in the process. More recently, geophysics techniques (e.g., ERT and GPR) were also adopted to investigate subsurface flow processes (Guo et al., 2020; Lamb et al., 2019). Although most techniques are either destructive or technically demanding, available data from common and field measurements (Pütz et al., 2016; Sommer et al., 2016), such as SWCs and pressure heads, could provide information on temporal dynamics of LSF.

Thus, we hypothesize that differences in the soil moisture dynamics between the field soil and the soil with a similar horizon sequence in the lysimeter will be indicative for the beginning of deviations from vertical flow in the field. We are aware that the possible occurrences of LSF and vertical preferential flow can only be indirectly determined with this approach; furthermore, data interpretation is affected by soil spatial heterogeneity and differences in plant and root distributions (Luo et al., 2019). The data analysis requires the evaluation and comparison of larger time series of water contents and pressure heads in

order to capture a wide range of conditions that include both water saturated and unsaturated soil condition. In regions with relatively low annual precipitation, such as in northeastern Germany (Herbrich & Gerke, 2017; Rieckh et al., 2012), transient near-saturated soil moisture conditions in subsurface horizons occur only infrequently.

One major challenge when analysing two time series of the SWC or the pressure head is to find possible correlations in these often nonstationary datasets (Ritter et al., 2009). Classical correlation analyses fail for datasets that include periodicities and trends (Biswas & Si, 2011). Temporal variation in the relationship between two time series cannot be specified if an overall correlation coefficient over the entire period is calculated (Bravo et al., 2020; Hu & Si, 2013). Time series of soil water state variables underlie periodic fluctuations like diurnal, seasonal, and annual cycles (Herbrich & Gerke, 2017; Liu et al., 2017; Rahmati et al., 2020).

Time series analysis of periodic signals is based on wavelet transform (Torrence & Compo, 1998; Grinsted et al., 2004). The transfer from the time domain into the frequency domain is achieved by comparing the original signal with a set of template functions of known frequency (Farge, 1992). The wavelet analysis can be used to determine the correlation between two time series, even if they are shifted in time, by calculating the coherency between two wavelet spectra (Grinsted et al., 2004). The squared wavelet coherence is a statistical tool to determine the similarity between two time series. It can be compared with R^2 in regression analysis and varies between zero and one (Si, 2008).

Wavelet coherency analysis (WCA) has been applied to detect spatial and temporal variations of soil hydraulic properties along a transect in the loess plateau of China (Yang et al., 2018) and differences in the moisture dynamics inside and outside of lysimeters for volcanic ash soils in southern Chile (Bravo et al., 2020). Earlier, Yang et al. (2016) compared the temporal stability of the soil matric potential of grassland and cropland with WCA and found stronger temporal variations in shallower than in greater depths. In their analysis of a 16-yr SWC record, Wu et al. (2002) determined the time shift in the SWC response to precipitation with depth. Lee and Kim (2019) used WCA for identifying vertical preferential flow events from the time shift in depth-dependent SWC responses between closer and more distant soil horizons.

The objective of this study is to identify deviations between field and lysimeter time series of SWC and pressure head for the analysis of the possible occurrence of LSF. The deviations are separately interpreted for specific rain infiltration events in all four seasons by assuming that flow in the lysimeter soil is forced to be vertical. For the WCA, wavelet, cross wavelet, and wavelet coherency spectra are analyzed that are obtained from a unique dataset of time series of SWC and pressure heads in a colluvial soil profile of an arable soil landscape for the 2016–2018 period.

3.4   Materials and Methods

3.4.1   Site and soil description

The datasets were measured with sensors installed in an intact soil monolith of a lysimeter and in the field at the monolith extraction pit. The field site is located in a hummocky ground moraine soil landscape at the CarboZalf-D experimental field of the Leibniz-Centre for Agricultural Landscape Research (ZALF), Müncheberg (Sommer et al., 2016) where the occurrence of LSF has been assumed (Filipović et al., 2018; Gerke et al., 2010). The site is located close to the village of Holzendorf, near Dedelow, northeast Germany (53°23′ N, 13°47′ E; 50–60 m asl). The average annual values of precipitation (495 mm), potential evapotranspiration (633 mm), and the annual mean air temperature (8.6 °C) were recorded from 1992 to 2016 at the Lysimeter Experimental Field Station Dedelow (53°22′2.45 N, 13°48′10.91 E) maintained by the ZALF (www.zalf.de). More information on the soils and hummocky arable soil landscape can be found elsewhere (Herbrich et al., 2017; Rieckh et al., 2012; Rieckh et al., 2014).

The 2-m-deep colluvial soil profile is from a toe slope position (Fig. 3.1) where the slope angle was about 4%. The intact soil monolith was extracted at the location "field" (Fig. 3.2) of the experimental site CarboZALF-D (53°22′43″ N, 13°47′01″ E in October 2012). The soil can be classified as Endogleyic Colluvic Regosol (IUSS, 2006) and consists of colluvial material down to about 70-cm depth (Fig. 3.1) covering a former Luvisol soil profile with gleyic features at the bottom. The soil properties (Tab. 3.1) were determined from bulk and 300-cm^3 core samples taken directly at the soil profile during the excavation of the soil monolith. Lateral flow could be expected to occur in the topsoil (Ap-horizon) above the plough pan and in the Ahb horizon above the relatively dense Btg horizon.
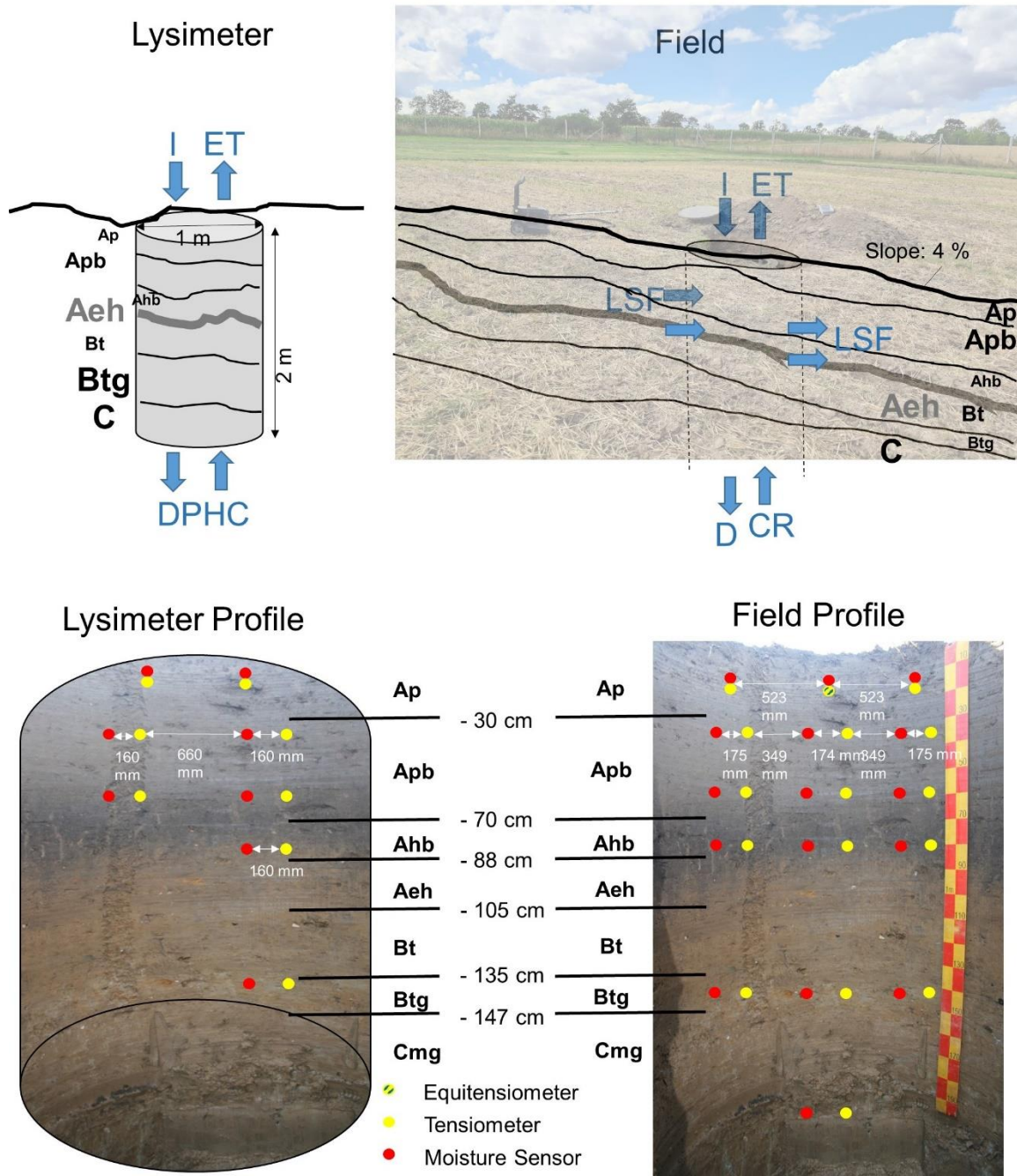
Figure 3.1: The lysimeter-field system with soil horizons and boundary conditions for the lysimeter (left) and the field (right) situation; upper two schemes: infiltration (I), evapotranspiration (ET), drainage (D), capillary rise from the water table (CR), dynamic pressure head control by soil water pressure head measured in the field (DPHC), lateral subsurface flow (LSF). Bottom pictures show the Endogleyic Colluvic Regosol soil profile after the extraction of the lysimeter and the location of the sensor installations of frequency domain reflectometry (red dots) and tensiometers (yellow dots) in the lysimeter (left) and the field (right). Soil horizons were classified according to IUSS (2006).

Table 3.1: Soil physical and chemical characteristics of the Endogleyic Colluvic Regosol(Fig 3.1): classification of soil horizons according to IUSS (2006) and KA5 (Ad-hoc-Arbeitsgruppe Boden, 2006); the organic C content (C_{org}), and the pH value (pH_{CaCl2}); and equivalent particle size of organic C-free and carbonate-free sieved (<2 mm) soil for sand (2–0.063 mm), silt (0.063–0.002 mm), and clay (<0.002 mm) (Michael Sommer, ZALF, personal communication, July 2020).

Horizon (IUSS, 2006)	Horizon (KA5)	Depth	Sand	Silt	Clay	C_{org}	pH_{CaCl2}
		[cm]	[g kg^{-1}]				[]
Ap[a]	Ap	0–30	630	260	100	0.90	5.05
Apb[a]	M	30–70	590	310	110	0.44	5.87
Ahb[b]	fAh	70–88	570	280	150	0.56	6.39
AEh	fAh-Al	88–105	580	260	170	0.34	6.66
Bt	Bt-sGo	105–135	560	240	190	0.22	7.01
Btg	Bt-sGro	135–147	570	240	190	0.12	7.27
Cmg	elCc-Gor	>147	580	290	140	0.01	7.69

[a]*Gray topsoil: sandy material from the eroded parts of the upper slope (E horizons).*

[b]*Former topsoil (dark color) with light colored filled earthworm burrows.*

The unsaturated soil hydraulic conductivity, K, was determined by throughflow experiments with tension disc infiltrometers for core samples extracted in vertical, K_v, and horizontal, K_h, direction (Tab. 3.2). The K values at a pressure head, h, close to full water saturation ($h = -1$ cm) decreased about 20-fold from K_h of about 24 cm d^{-1} towards a value of 1.0 cm d^{-1} for the Btg-horizon. The values were higher in horizontal as compared to vertical direction (Tab. 3.2) for the Apb, Ahb, and Btg-horizons and the values of anisotropy ratios K_v/K_h are ranging between 0.4 and 0.7.

Table 3.2: Soil bulk density (ρ_b), soil hydraulic conductivity in vertical (K_v) and horizontal (K_h) direction measured at pressure head of h = -1 cm, and anisotropy ratio (K_v/K_h). Mean values, SD, and SE from five replicates are shown.

Horizon	ρ_b		K_h			K_v			K_v/K_h
	Mean	SD	Mean	SD	SE	Mean	SD	SE	
	[g cm^{-3}]		[cm d^{-1}]						[]
Apb	1.65	0.06	14.94	10.96	5.48	6.59	4.39	1.97	0.44
Ahb	1.63	0.03	23.72	22.32	9.98	14.38	13.28	5.94	0.61
Btg	1.82	0.07	1.02	1.13	0.51	0.70	0.15	0.07	0.68

The soil monolith extraction, the lysimeter setup, and the installation of the sensors in the lysimeter soil and of the field soil profile were carried out by the company Umwelt-Geräte-Technik (UGT). A special soil cutting device was used that allowed for minimal disturbance during the extraction of the intact soil monolith and the surrounding field soil profile. The extracted soil monolith was fitted in a stainless steel cylinder of 1-m² surface and 2-m height and moved to a lysimeter station located about 80 m northeast (53°23′21″ N, 13°47′6″ E) of the "field" extraction site (Fig. 3.2). Here, the soil monolith lysimeter was placed in a larger polyethylene-casing box that was recessed into the ground such that the surfaces of the soil in the lysimeters and the surrounding soil were at the same level. A detailed description of the lysimeter equipment can be found elsewhere (Umwelt-Geräte-Technik, 2013). At the lysimeter bottom, the flux out of or into the lysimeter soil is controlled by filter panels that allow for conditions in the lysimeter soil that correspond with pressure head values measured in the field in a depth of 190 cm. By this dynamic pressure head control of the lysimeter's bottom boundary it was intended to match the soil water dynamics according to that of the field soil. The idea was to mimic field conditions of both downward flow during times with a relatively shallow water table in the field and upward capillary water flow from deeper soil regions to avoid drier conditions and more reactive responses of the SWC on precipitation in the lysimeter as compared to the field soil (Groh et al., 2016).

Figure 3.2: Aerial image (capture date range: 30 June 2010 to 19 Sept. 2016) and map of the experimental field site (CarboZalf-D) located in northeastern Germany; the locations of the rain gauges and the "field" soil profile and "lysimeter" station. Locations of rain gauges for measuring precipitation are numbered (1–5), and instrument types are described (Appendix A3.2).

At the monolith extraction site ("field" in Fig. 3.2), a cylindrical plastic tube was inserted in the 2-m-deep hole to stabilize the profile walls and to be able to cover it later with topsoil after the installation was completed. From the inside of this 1-m^2 tube, the frequency domain reflectometry (FDR) sensors and tensiometers were horizontally inserted into the surrounding soil at the same profile locations as in the lysimeter (Fig. 3.1). Data from the field and the lysimeter were monitored in hourly intervals by data loggers outside the managed field plot connected with subsurface data cables. The plastic tube at the "field" was then closed and covered by about 35 cm of soil such that soil cultivation including plowing, seedbed preparation, crop management, and harvesting (Appendix A3.1) could be carried out uniformly for the whole plot. The soil and crop management of the lysimeter was carried out manually, thus trying to imitate the management of the field plot.

Both soil profiles (i.e., "field" and "lysimeter") were equipped with sensors for measuring SWC and soil water pressure head (Fig. 3.1). The SWC was measured with FDR sensors (SM300, after August 2018: SMT-100, UGT) in up to three replicates per depths. The soil water pressure head was measured with tensiometers (Tensio160, UGT) and an Equitensiometer (EQ15, ECOMATIK) with a measurement range of up to −1,500 kPa and an accuracy of ±10 kPa. The sensors were installed in 15-, 32-, 60-, 85-, 140-, and 190-cm depths in the lysimeter and in 15-, 32-, 55-, 80-, 140-, and 195-cm depths in the field. In the lysimeter, two sensors of each type were inserted down to 60-cm soil depth sensors and a single one in the depths below. In the field soil profile, three sensors of each type were inserted per depth level, except for 195-cm depth, where only one tensiometer and FDR-sensor were installed and in 15-cm depth, where one Tensio160 was replaced by the EQ15 (Fig. 3.1). Data were recorded since August 2013 in uniform intervals of 1 h with data logger DL-2000 (UGT).

Precipitation was recorded by different types of rain gauges (Appendix A3.2) at five locations distributed at the experimental field (Fig. 3.2). The time-resolved precipitation data were aggregated to hourly sums and manually corrected for outliers. For the analysis, the arithmetic mean of corrected data of the available sensors was used. Here, field and lysimeter sensor data of the relatively wet year 2017 (656 mm yr^{-1}) were compared with those of the relatively dry years 2016 (385 mm yr^{-1}) and 2018 (303 mm yr^{-1}).

3.4.2   Time series data gap filling procedure

The application of the WCA requires continuous time series without data gaps of a period that covers as much of the temporal variation as possible (e.g., Bravo et al., 2020, analyzed a period of several years); however, shorter periods have also been studied (Lee & Kim, 2019). Thus, a data gap filling procedure was used (see Appendix A3.3 for more details) to obtain consistent time series of comparable quality. Still, logger failures for a period of more than one day led to missing data that could not be reconstructed. Thus, only complete periods without data gaps in the time series were selected for the present analysis. Data processing was carried out with the software R 3.6.2 (R Core Team, 2019).

3.4.3   Wavelet analysis and WCA

The complex Morlet wavelet (wavenumber $k_0 = 6$) was applied here because it provided a balance between time and frequency resolution (Grinsted et al., 2004) and information about phase and amplitude of a signal (Torrence & Compo, 1998). Wavelet coherence (ρ^2) was calculated (Torrence & Webster, 1999) as

$$\rho^2_{X,Y} = \frac{\overline{S}^2_{X,Y}}{\overline{S}_{X,X}\,\overline{S}_{Y,Y}} \tag{3.1}$$

where $\overline{S}^2_{X,Y}$ is the smoothed cross-wavelet transform of the time series *X* and *Y*, and $\overline{S}_{X,X}$ and $\overline{S}_{Y,Y}$ are the smoothed wavelet spectra of the time series *X* and *Y*. The cone of influence (COI) is the part of the plot of the wavelet coherency spectrum (WTC) where edge effects due to padding of the time series with zeroes to a length of 2^n time steps can be ignored. According to Grinsted et al. (2004), the COI is here calculated as the area in which the wavelet power caused by a discontinuity at the edge has dropped to e^{-2} of the value at the edge.

Statistical significance was tested to detect whether the wavelet spectra differed from a "red noise" background power spectrum modeled by a first order autoregressive (AR1) process. For the wavelet coherence, statistical significance was calculated by a Monte Carlo method. A number of 300 surrogate dataset pairs was used for the Monte Carlo estimation of the significance level. A 5% significance level against red noise was chosen. Further details can be found in Si and Zeleke (2005) and Grinsted et al. (2004). Calculations of the wavelet spectra, cross wavelet spectra, and wavelet coherency spectra were carried out in Matlab (2019b) with the code provided by B. Si and W. Hu. This code was based on the Matlab-code developed by A. Grinsted that is available under http://www.glaciology.net/wavelet-coherence.

3.4.4 Crop development in field and lysimeter

The development of plant height was observed at the field plot from autumn 2016 to spring 2018 (Fig. 3.3). The winter rye (*Secale cereale* L.) crop was planted in autumn 2016 and 2017 and used only as a cover crop before cultivation for the summer crops maize (*Zea mays* L., 2017) and oat (*Avena sativa* L., 2018). Crop yield was measured as dry mass of biomass for maize and as grain yield for oat (Tab. 3.3). It was larger for the lysimeter than for the field plot in both years. Depth of the rooting system was not recorded since this would lead to distortions in the lysimeter measurements. A previous study of Herbrich et al. (2018) suggested a maximal rooting depths for wheat (*Triticum aestivum* L.) of 150 cm at this site. Average maximal rooting depth for grains like rye and oat of 150–180 cm and 120–150 cm for maize can be assumed (Kutschera et al., 2009).

Table 3.3: Cropping dates and of biomass for maize (2017) and grain yield of oat (2018) for the lysimeter (Lys) and the field plot (Michael Sommer & Gernot Verch, ZALF, personal communication, July 2020).

Crop	Plot	Planting date	Harvest date	Dry mass
				[kg m^{-2}]
Maize	Lys	24 Apr. 2017	25 Sept. 2017	3.81
	Field	24 Apr. 2017	25 Sept. 2017	1.98
Oat	Lys	9 Apr. 2018	30 July 2018	0.37
	Field	9 Apr. 2018	30 July 2018	0.30
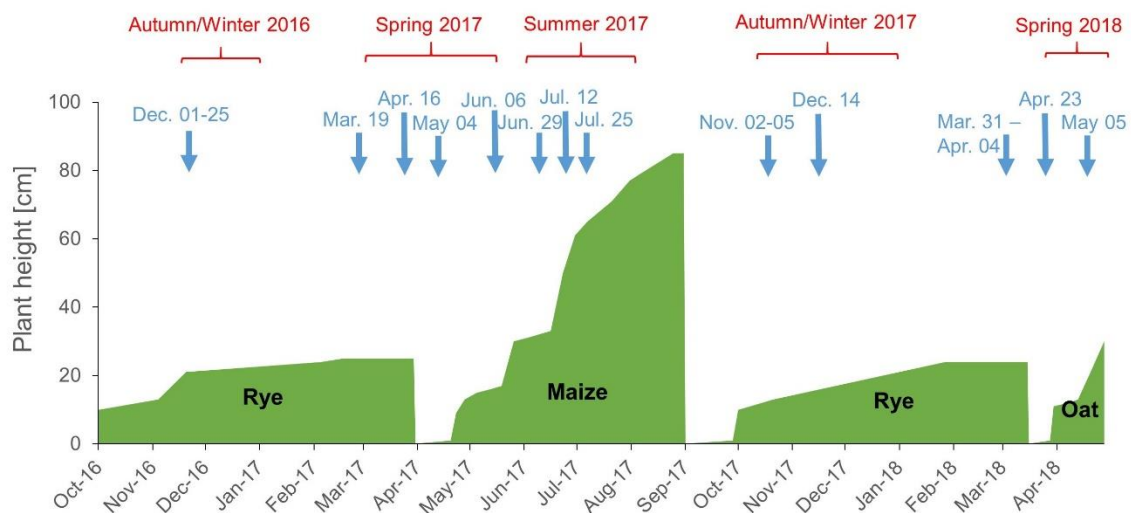
Figure 3.3: Crops and height of vegetation during the investigation period. Blue arrows indicate the occurrence of the analyzed precipitation events. Planting dates are found in Tab. 3.3. Periods of investigation with wavelet coherency analysis are marked with red braces.

3.5   Results

This chapter is structured to first explain results of the WCA and then compare lysimeter and field data for relatively wet (2017) and relatively dry periods (autumn 2016, spring 2018). These periods were without any frost or snow cover in winter, such that any delay in infiltration response to precipitation due to melting of ice snow was unlikely.

3.5.1   Wavelet coherence analyses of the SWC in the wet year (2017)

The water content increased after major precipitation events on the 19 Mar. 2017 and the 16 Apr. 2017 in a soil depth of 15 cm of the lysimeter and field (A1 in Fig. 3.4). Note the different SWC levels for field and lysimeter are not artifacts but related to the differently compacted topsoil regions in which sensors in the field were installed; the lysimeter soil was less compacted due to manual cultivation. All replicate sensors measured similar ranges of SWC values (Fig. 3.4); in the following figures, we therefore focus on mean values from replicate sensors.
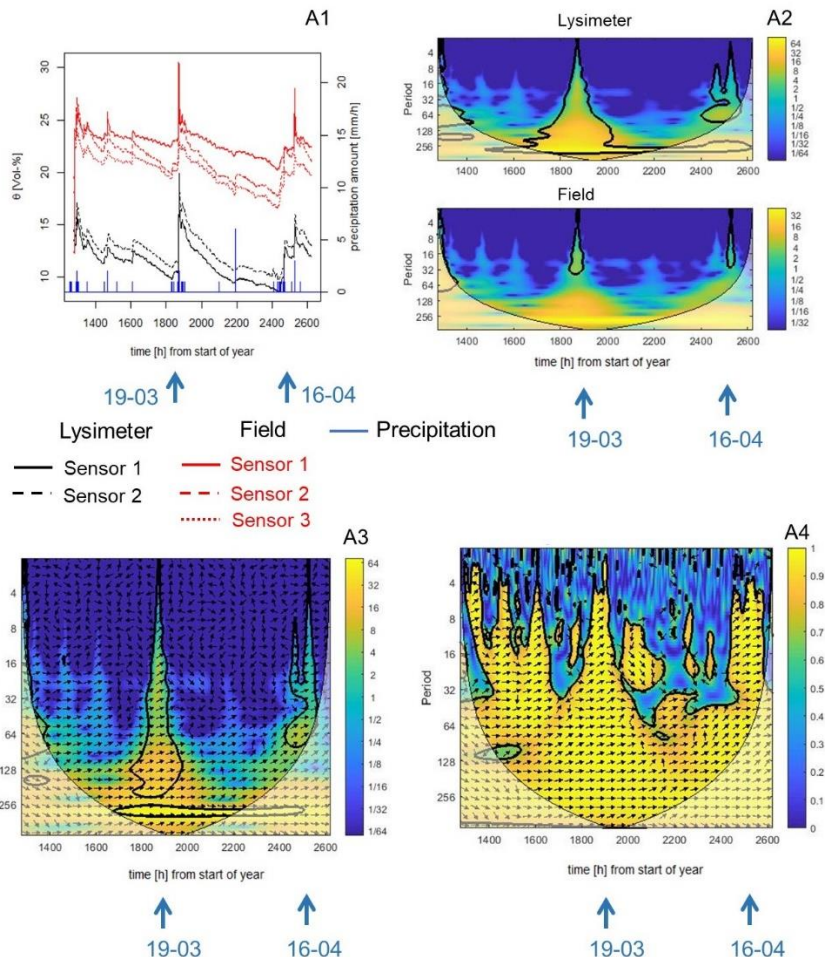
Figure 3.4: (A1) Response of soil water content (SWC, θ) at 15-cm depth (spring 2017) in the lysimeter (black lines) and field (red lines) profile on precipitation events vs. time in hours from the beginning of the year, and plots of (A2) wavelet spectra of SWC (15 cm) in the lysimeter (top) and field (bottom), (A3) cross wavelet spectrum, and (A4) wavelet coherency spectrum (WTC). Major precipitation events that were further analyzed are marked with a blue arrow and a date (day-month) below the plot.

The response of the water content on the precipitation events are reflected in the wavelet spectra as significant deviations (i.e., marked as thick contour lines, significance level: 5%) from the background spectrum (red noise) in lysimeter and field (A2 in Fig. 3.4); the *x* axis is the time in number of hours from the beginning of the year, and the *y* axis depicts the periodicity. The periodicity is in the unit of hours and characterizes temporal significance patterns (e.g., a significant deviation on a daily basis is observed if the thick contour line appears at a periodicity of 24 h). The shaded area outside the COI marks the part of the plot with larger edge effects (see Section 2). The color scale indicates the magnitude of the wavelet power. A high wavelet power (yellow color) denotes a high similarity between the wavelet function and the time series at this point in time and this scale. This means that at scales where the wavelet power is high, this periodicity is also found in the signal.

The interpretation of the wavelet spectra is explained for the example in Fig. 3.4. The wavelet spectrum of the SWC (A2 in Fig. 3.4) during precipitation event on 19 Mar. 2017 deviates significantly from the background spectrum at periodicities ranging for the lysimeter from 4 to 256 h (~11 d) and periodicities of 4–32 h for the field. A similar pattern but without deviations from the background spectrum at periodicities from 72 to 200 h is found for the lysimeter for the precipitation event on 16 Apr. 2017. The cross wavelet spectrum (A3 in Fig. 3.4) contains additional information about the time shift and the covariance between two time series; it here indicates a high covariance during the two precipitation events mentioned before. Arrows pointing upwards indicate a faster reaction to precipitation (i.e., a faster increase in SWC) in the field soil as compared with the lysimeter soil, whereas arrows turned downwards show a faster reaction in the lysimeter. A faster reaction to precipitation in one plot in comparison with another plot refers to a faster increase in SWC or pressure heads in response to precipitation. Since the cross wavelet transform is the product of the two wavelet spectra of the field and lysimeter soil, the color scale of the cross wavelet spectrum (A3 in Fig. 3.4) indicates the strength of the covariance between the spectra at a certain point in time and at a certain scale. The plot of the WTC provides information about the time shift in the correlation between two time series (A4 in Fig. 3.4). For the abovementioned precipitation events, high correlations are indicated across all scales from 6 h to 2 wk. The strength of the correlation (color scale) is here indicated by a relative scale, with 0 indicating no correlation and 1 indicating a perfect correlation. The information on phase shift are similarly provided by the arrows as in the cross wavelet spectrum; arrows pointing upwards indicate a faster reaction to precipitation of SWC in the field soil as compared with the lysimeter. Note that the wavelet spectra and the cross wavelet spectrum of data from lysimeter and field of other depths and seasons are presented in the appendix (Appendix A3.4–A3.6).

Selected seasonal time series in 2017 and WTC plots of SWC dynamics in 15-, 32-, 60-, and 80-cm depths in spring, summer, and autumn 2017 (Fig. 3.5) differ between lysimeter and field soil with respect to the levels and temporal patterns of the SWC. The response to precipitation is generally decreasing with soil depth (A1, B1, and C1 in Fig. 3.5). For the spring period (15-cm depth: 23 Feb. until 20 Apr. 2017; 32-to-80-cm depth: 23 Feb. until 22 May 2017; unfortunately not for all the depths time series with the same length were available due to sensor and logger failures), the WTC plots (A2 in Fig. 3.5) reflect these patterns and indicate that the response of the SWC in the field profile on precipitation is generally faster than that of the SWC in the lysimeter soil. The periodicity of significant relations is between 6 h to 2 wk at the precipitation events in 15-cm depth; this periodicity increases with soil depth to 1 d to 2 wk (32-cm depth) and 2 d to 2 wk (60-cm depth). In 80-cm depth almost no significant correlations between rain and SWC increase in lysimeter and field are found.

Figure 3.5 (next page): Time series of the soil water content (SWC, θ) in lysimeter and field (A1, B1, and C1) and wavelet coherency spectra (WTC plots) of SWC in lysimeter and field (A2, B2, and C2) at 15-cm, 32-cm, 60-cm, and 80-cm depth in spring, summer, and autumn of the wet year 2017. Major precipitation events that were further analyzed are marked with a blue arrow and a date (day-month) below the plot. The x axis of the plots denotes the time in number of hours from the start of the year; the period of the WTC plots is given in hours (more explanations of the WTC plots can be found in the text).
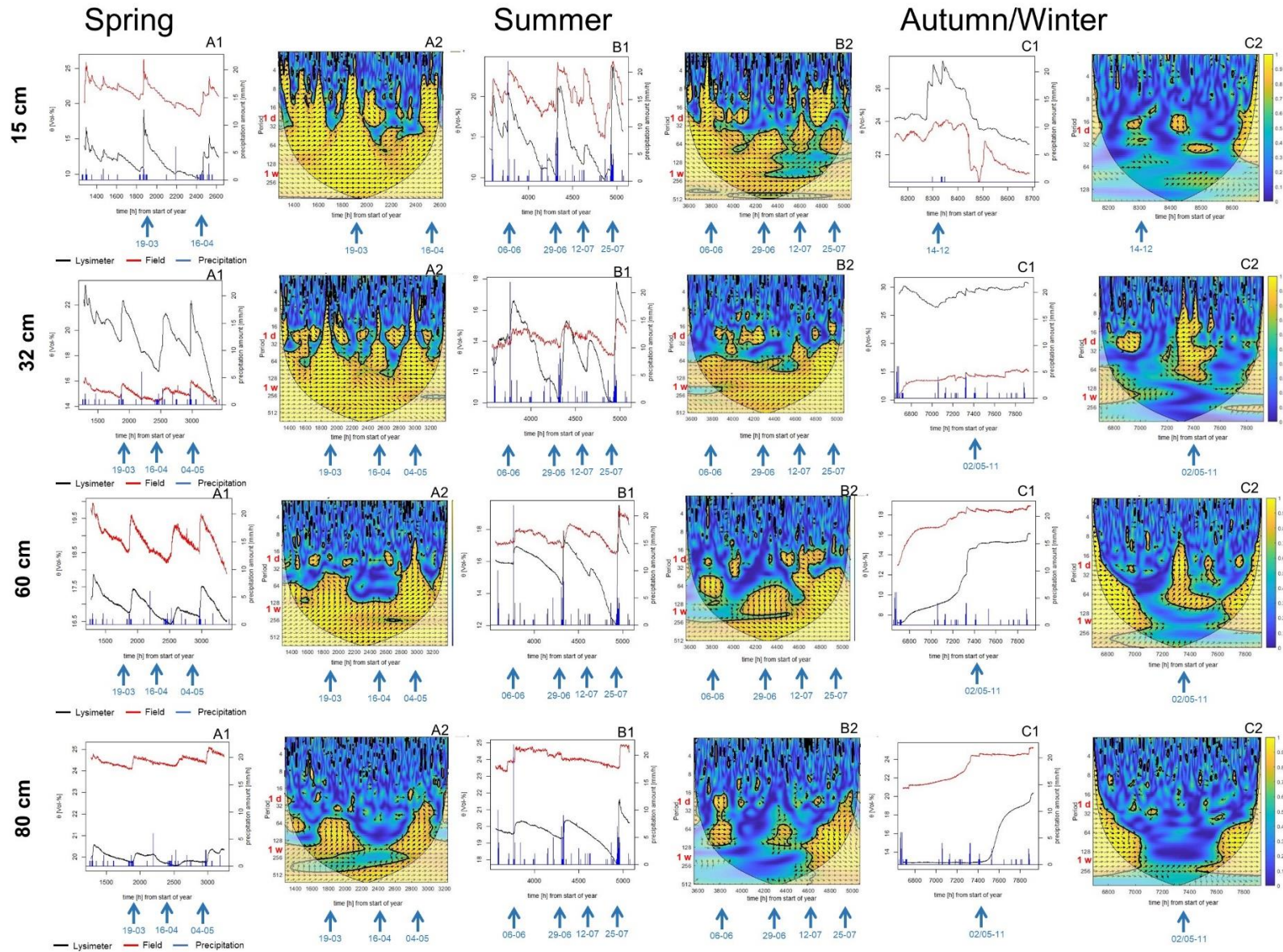
During the summer period (1 June until 31 July 2017), the moisture dynamics (drying–wetting) increased in comparison with spring (B1 in Fig. 3.5). However, the WTC plots (B2 in Fig. 3.5) indicate fewer significant periods at higher periodicities (2 d to 2 wk) as compared with the spring. High correlations at smaller periodicities (6 h to 1 d) are only found in 15 cm at times of precipitation. More significant correlations at precipitation events at 80-cm depth are found in summer than in spring. The field plot moisture sensor at 32-cm depth showed almost no response to precipitation resulting in only a few short correlations at the periodicity of 1 d in the WTC plot (B2 in Fig. 3.5). For the summer season, arrows indicating the phase shift throughout the precipitation events are in phase or point upwards in the shallower depths (15- and 32-cm depth). This marks a simultaneous water content increase in lysimeter and field or a faster water content increase in the field as compared with the lysimeter soil, respectively, similar to the patterns found in spring. In contrast, in the deeper horizons (60- and 80-cm depth) arrows indicating the phase shift point downwards (B2 in Fig. 3.5), denoting a faster response in the lysimeter soil than in the field soil at the corresponding precipitation events.

During the autumn and winter period (32-to-80-cm depth: 10 Oct. until 30 Nov. 2017; 15-cm depth: 1 Dec. until 31 Dec. 2017), the lysimeter and field plot moisture dynamics was mostly uncorrelated and without response to precipitation (C1 and C2 in Fig. 3.5) except perhaps for 32-cm and 60-cm depth, where the WTC plot is significant at periodicities from 6 h to 3 d from 2 until 5 Nov. 2017. Phase shift arrows indicate a faster response of SWC to precipitation in the field soil as compared with the lysimeter soil, similar to the patterns found in spring.

Note that the relatively small SWC values in the lysimeter soil (Fig. 3.5) of about 10 Vol-% (unit of the volumetric soil water content in volume percentage) during summer (all depths) and spring (topsoil) are well above a residual SWC determined earlier of about 3.5 Vol-% at 15-cm depth and 4 Vol-% at 80-cm depth (Rieckh et al., 2012).

3.5.2 Pressure head values in the wet year 2017

Pressure head values increased in the wet year 2017 after precipitation events (A1 to D1 in Fig. 3.6), which is reflected by significant correlations between lysimeter and field soil across all scales from 6 h to 2 wk in the WTC plots (A2 to D2 in Fig. 3.6).

At 15-cm depth, lysimeter and field reacted simultaneously to precipitation on 6 June 2017, whereas for the later events, pressure head values increased faster in the field than in the lysimeter (A2 in Fig. 3.6), similar to the patterns found for the water content in the corresponding depth and season (B2 in Fig. 3.5). At 60-cm depth, the pressure heads increased faster in the field than in the lysimeter soil for all major precipitation events in spring (B2 in Fig. 3.6). Increase in pressure heads in the lysimeter as compared with the

field was faster at 80-cm depth in summer (C2 in Fig. 3.6). At 140-cm depth, the lysimeter showed a faster reaction to precipitation than the field in spring 2017 (D2 in Fig. 3.6).
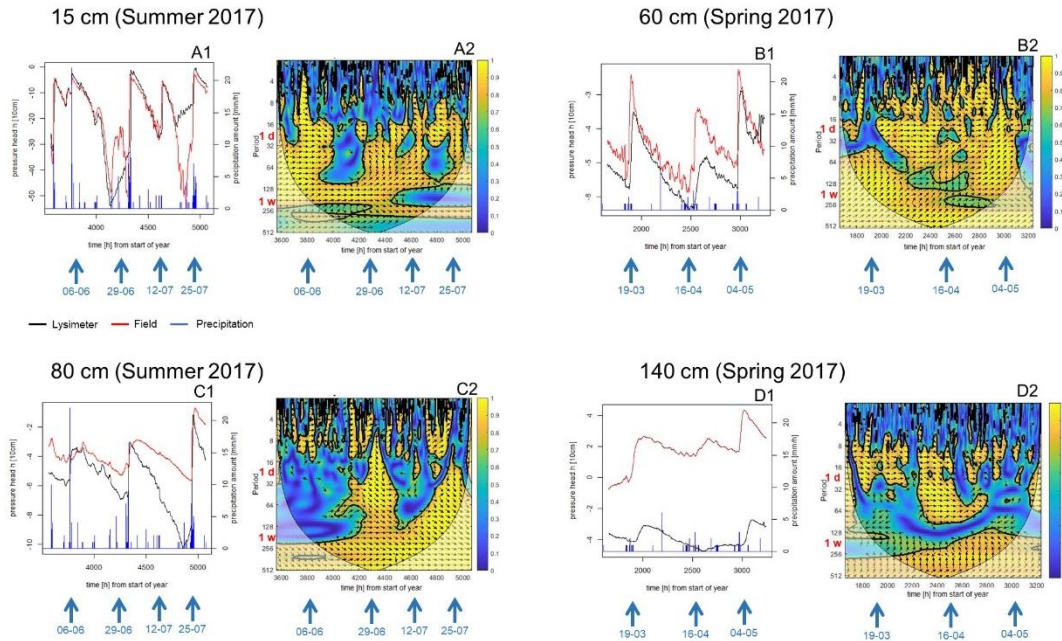
Figure 3.6: Time series of the pressure head values in lysimeter and field (A1, B1, C1, and D1) and wavelet coherency spectra (WTC plots) of pressure head values in lysimeter and field (A2, B2, C2, and D2) at 15-cm (summer 2017), 60-cm (spring 2017), 80-cm (summer 2017), and 140-cm depth (spring 2017). Major precipitation events are marked with a blue arrow and a date (day-month) below the plots; the time is given in hours since the beginning of the year; the period of the WTC plots is given in hours (more explanations of the WTC plots can be found in the text).

3.5.3 SWC values in relatively dry years 2016 and 2018

Selected time series of SWC in lysimeter and field of the dry years 2016 and 2018 show a general increase of water content in autumn and winter 2016 and a decrease in spring 2018 (A1 and B1 in Fig. 3.7). Note that there were no data available during the summer periods. Impacts on SWC increase due to precipitation diminish with depth. The corresponding WTC plots also show a decrease of correlations between SWC changes in lysimeter and field with depth (A2 and B2 in Fig. 3.7). Significant correlations are generally found in connection with precipitation events. The smallest periodicities with significant correlations increase from 6 h at 15-cm depth to 1 d at 60-to-140-cm depth. Arrows representing the phase shift indicate a faster increase in water content in the field soil as compared with the lysimeter soil at almost all precipitation events. Only on 1 Dec. 2016, the lysimeter soil shows a faster increase in water content than the field at 15- and 32-cm depth at periodicities from 2 d to 1 wk (A2 in Fig. 3.7). Note that at 15-cm depth (A2 in Fig. 3.7), the phase shifts on 1 Dec. 2016 are contradictory because they are indicating a faster reaction in the field soil than in the lysimeter at periodicities of 2 d and a slower response at periodicities of 1 wk.
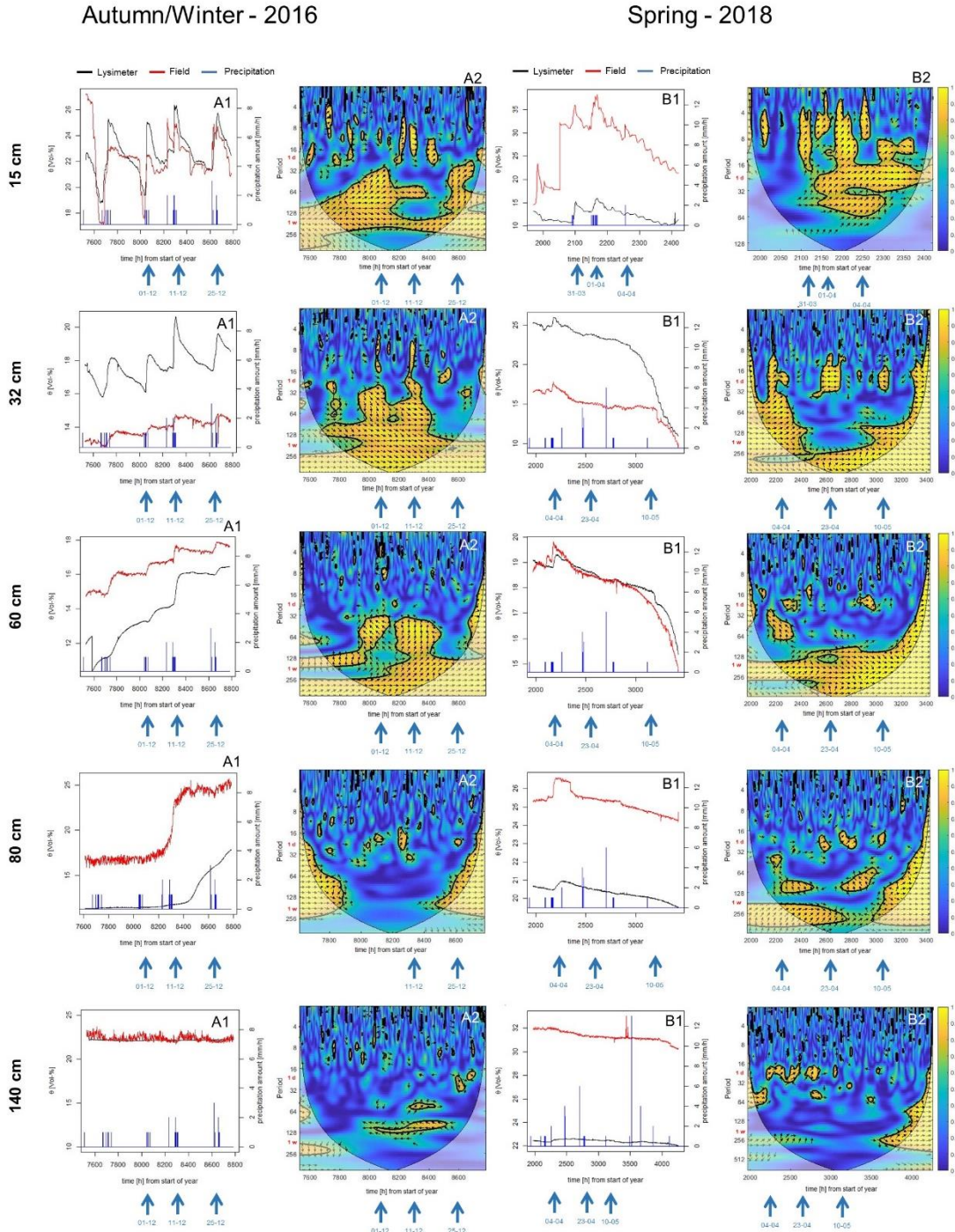
Figure 3.7: Time series of the soil water content (SWC) in lysimeter and field (A1 and B1) and wavelet coherency spectra (WTC plots) of SWC in lysimeter and field (A2 and B2) at 15-, 32-, 60-, 80-, and 140-cm depth in autumn 2016 (dry year) and spring 2018 (dry year). Major precipitation events are marked with a blue arrow and a date (day-month) below the plot. The x axis of the plots is time in number of hours from the beginning of the year; the period of the WTC plots is given in hours (more explanations of the WTC plots can be found in the text).

3.5.4 Response time for SWC to precipitation

The distribution of the precipitation at the site is typically characterized by lower intensity rain and a few higher intensity summer events (Herbrich et al., 2017), as for the selected period, in which precipitation events with higher amount and rate occurred during summer and those with less intensity and lower amounts in spring, autumn, and winter (Tab. 3.4). The response time between the start of the rain and the first SWC reaction seasonally differed when plotted with respect to the maximal rain intensity (Fig. 3.8). Below 32-cm soil depth, the field SWC reacted earlier to precipitation in spring and in autumn, whereas during summer, the SWC in the lysimeter reacted faster than that in the field soil (Fig. 3.8) regardless of the antecedent moisture condition (i.e., for wet and dry years).
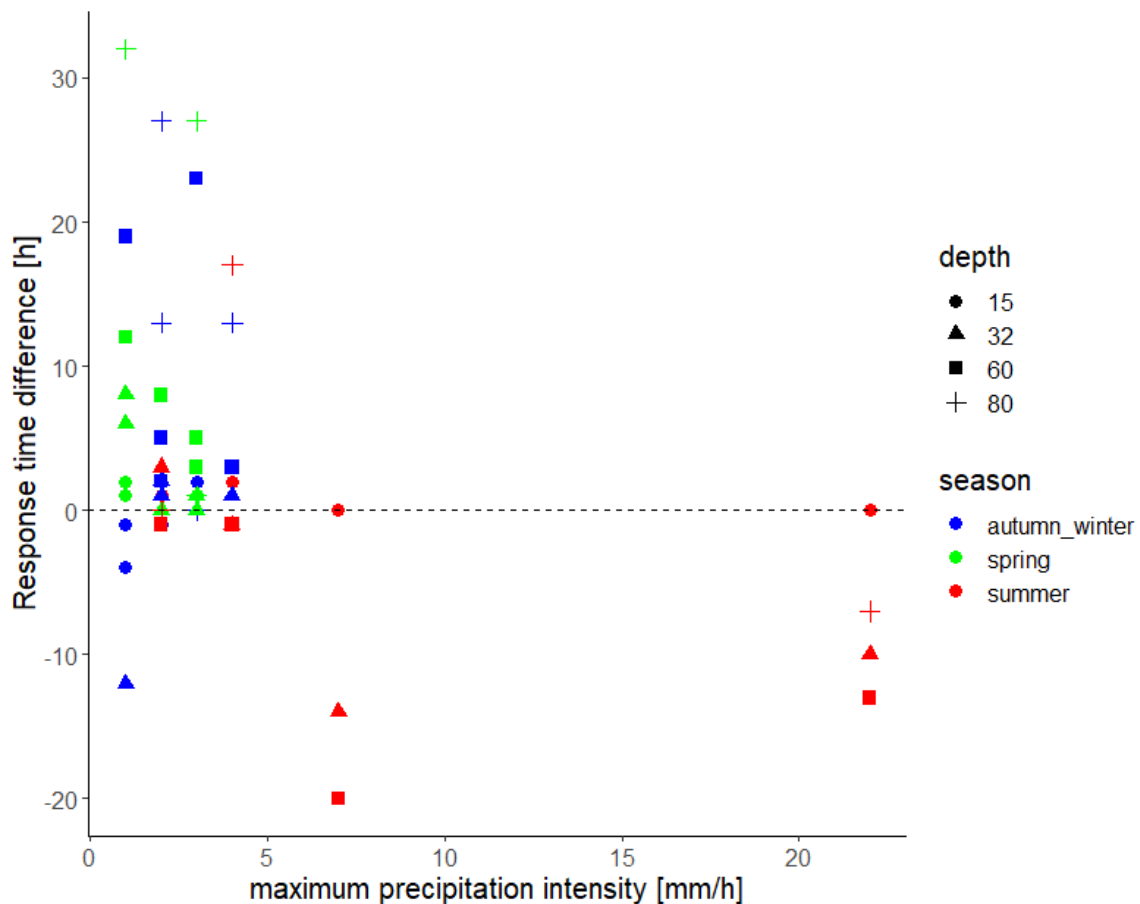
Figure 3.8: Response time difference (i.e., difference in reaction time in hours between lysimeter and field) of soil water content (SWC) increase in lysimeter and field related to maximal precipitation intensity for the four soil depths and the season. If the reaction time is positive, the field soil reacted faster than the lysimeter soil in that same depth. If the reaction time is negative, the field SWC increased later than the lysimeter SWC in response to the rain event.

The sequence of the SWC response to precipitation in field and lysimeter that was found in the WTC plots is also visible in the plots of the single precipitation events (Fig. 3.9 and Appendix A3.7). From the top to the bottom of the profile, the sensors responded

sequentially to precipitation events (i.e., the upper horizons increased in water content before the lower horizons). However, in the field (Fig. 3.9, A–C), a simultaneous reaction to precipitation is found in 32-cm and 60-cm depth. In addition, for at least two events, vertical preferential flow occurred in the soil profile of the lysimeter, as the response of the SWC on the precipitation event at 60-cm depth was faster than the SWC response at 32-cm depth (Fig. 3.9, C and D). On 2 Nov. 2017 (Fig. 3.9, E), we can see a sequential vertical response in the lysimeter, but the increase of SWC in 60 cm was larger and continued longer than the SWC at 32-cm soil depth.

Table 3.4: Characterization of major precipitation events in autumn 2016, 2017, and spring 2018 and sequence of soil water content (SWC) response to precipitation.

Season	Start	Dur	Ra	Ri_av	Ri_max	First reaction				
						15	32	60	80	140
	date (h:min)	[h]	[mm]	[mm h^{-1}]		[cm]				
Autumn/ winter	1 Dec. 2016 07:00	6	6	1	1	L	L	F	/	n.d.
	11 Dec. 2016 04:00	*8*	*9*	*1.1*	*2*	*L*	*F*	*F*	*F*	*F*
	25 Dec. 2016 01:00	1	3	3	3	F	F	F	S	F
Spring	*19 Mar. 2017 15:00*	*9*	*11*	*1.2*	*2*	*F*	*S*	*F*	*L*	n.d.
	16 Apr. 2017 06:00	3	5	1.7	3	F	F	F	F	n.d.
	4 May 17 08:00	12	21	1.8	3	n.d.	S	F	F	n.d.
Summer	*6 June 2017 17:00*	*4*	*31*	*7.8*	*22*	*S*	*L*	*L*	*L*	n.d.
	29 June 2017 09:00	*6*	*11*	*1.8*	*7*	*S*	*L*	*L*	*L*	n.d.
	12 July 2017 13:00	9	12	1.3	2	F	F	L	S	n.d.
	22 July 2017 17:00	3	8	2.7	4	F	L	L	L	n.d.
Autumn/winter	*2 Nov. 2017 00:00*	*8*	*20*	*2.5*	*4*	n.d.	*F*	*F*	*F*	n.d.
	5 Nov. 2017 18:00	6	8	1.3	2	n.d.	*F*	*F*	*F*	n.d.
	14 Dec. 2017 04:00	4	4	1	1	L	n.d.	n.d.	n.d.	n.d.
Spring	*29 Mar. 2018 01:00*	*5*	*3*	*0.6*	*1*	*F*	*F*	*F*	*F*	*F*
	31 Mar. 2018 14:00	3	2	0.7	1	*F*	*F*	*F*	*F*	*F*
	31 Mar. 2018 20:00	2	2	1	1	*F*	*F*	*F*	*F*	*F*
	1 Apr. 2018 02:00	7	5	0.7	1	*F*	*F*	*F*	*F*	*F*

Note. L, lysimeter reacts first; F, field reacts first; S, simultaneous reaction; /, no reaction observed; n.d., no data; numbers and letters in italic indicate precipitation events in Figs. 3.8 and 3.9; other events are depicted in Appendix A3.7. Dur, duration; Ra, precipitation amount; Ri_av, average intensity; Ri_max, maximum precipitation intensity.
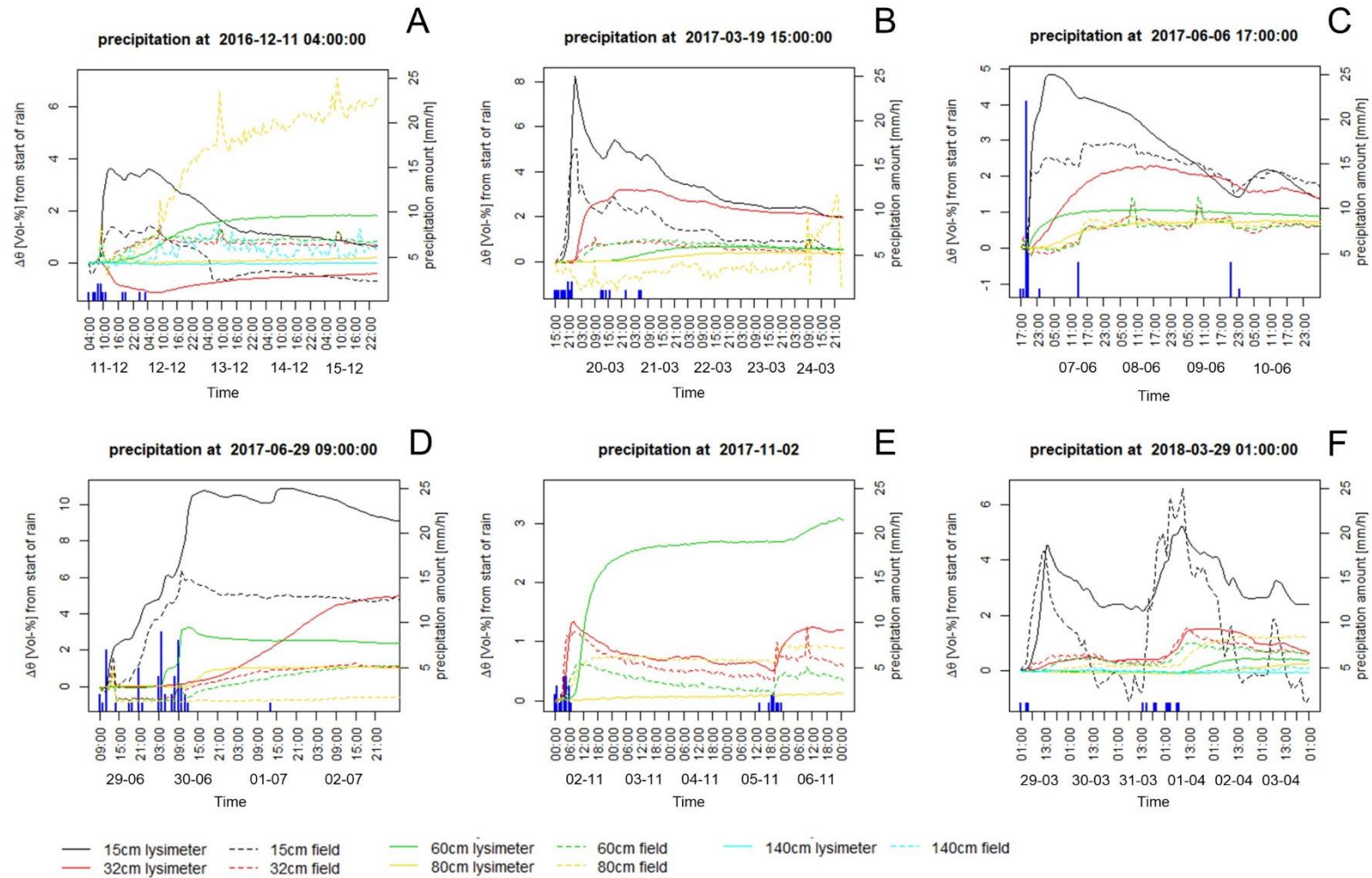
Figure 3.9: Soil water content (SWC, θ) change (increase) in response to selected precipitation events in lysimeter and field at the 15-, 32-, 60-, 80-, and 140-cm depths in 2016, 2017, and 2018.

3.6 Discussion

For identification of LSF based on discrepancies in water dynamics between lysimeter and field, one has to consider that the position of the soil profile in the field is at the toe slope close to the kettlehole depression (Figs. 3.1 and 3.2). A faster and more intensive water content increase in the field in comparison with the lysimeter could indicate lateral flow from the upper slope, if at the same time the SWC of the soil profile in the lysimeter responds sequentially in a vertical direction on infiltration. If the field reacts slower and less intensively to precipitation than the lysimeter, this could be attributed to lateral drainage downslope, whereas in the lysimeter soil, the infiltrating water moves vertically and leads to sequential SWC increase. Under these standard multidimensional flow presumptions (Filipović et al., 2018) and considering combinations with spatial heterogeneity (Guo & Lin, 2018; Lin & Zhou, 2008) and vertical preferential flow effects due to macropore-centred saturation (Newman et al., 2004), we will discuss the WCA results for time series of lysimeter and field state variables to identify periods of deviations that might be interpreted as vertical preferential flow or LSF.

3.6.1 Verification of WCA-derived deviations in time series

Correlations in water dynamics between field and lysimeter were observed across all scales in response to precipitation events (Figs. 3.4–3.7). These correlations occurred regardless of the season or the antecedent SWC conditions. The time lag between SWC increase in the field and in the lysimeter after precipitation indicated by phase shift arrows could be verified when analyzing the water content increase for each single precipitation event (Fig. 3.9). In spring and autumn, the WTC plots (Figs. 3.5 and 3.7) indicated an earlier response in the field as compared with the lysimeter as observed in the time series directly (Fig. 3.9). In summer 2017, the WTC plots showed a faster reaction in SWC increase in response to precipitation in the lysimeter than in the field (Fig. 3.5). Again, this response pattern was found in the plots (Fig. 3.9).

Similar to results reported by Bravo et al. (2020), correlations between water dynamics inside and outside the lysimeter occurred especially in response to heavy precipitation events. This was explained by the decrease in variability of soil hydraulic properties at higher SWC during rain events due to more water connecting pores between the soil inside and outside the lysimeter as compared with times of less precipitation. Unlike our findings, correlations in the study of Bravo et al. (2020) were mostly in phase, indicating a simultaneous increase in water content or pressure heads in response to precipitation. However, the soil profiles in the study of Bravo et al. (2020) were not extracted at a hillslope and had no compacted soil horizons. In our study, LSF was expected because of contrasting hydraulic properties (Laine-Kaulio et al., 2014; Liu & Lin, 2015) with more over

less permeable horizons (Tab. 3.2). The soil of the Ahb horizon was characterized by hydraulic anisotropy with a higher horizontal (23.7 cm d^{-1}) than vertical hydraulic conductivity (14.4 cm d^{-1}) at the 70-to-88-cm depth. The more compact (bulk density of 1.82 g cm^{-3}) subsoil horizon below at the 135-to-147-cm depth had more than 20 times lower hydraulic conductivity values (Tab. 3.2) at the same pressure head of −1 hPa for the vertical (0.7 cm d^{-1}) and horizontal direction (1.0 cm d^{-1}). This supports the presumption that LSF could occur in the field while pressure buildup would occur in the lysimeter, which could lead to differences in soil water dynamics between lysimeter and field.

Bravo et al. (2020) related short-term temporal correlations to rather extreme conditions like heavy precipitation, whereas long-term patterns of periodicities between 1 and 2 mo were ascribed to slower hydraulic processes during continuous drying or wetting periods. In our study, such continuous wetting and drying periods were observed in autumn 2016 and in the spring seasons, which was reflected in the WTC plots by positive correlations between lysimeter and field at higher scales of 2–3 wk (Figs. 3.4–3.7). Thus, similar overall trends in the different seasons in drying and wetting of the soil can be identified by WCA. The coherence at high-frequency periodicities between precipitation and soil moisture also decreases with depth (Liu et al., 2017), which was here more pronounced for the lysimeter than the field soil because of the SWC increase caused by restricted LSF (Figs. 3.5 and 3.7).

3.6.2 Causes for deviations between lysimeter and field data

Although lysimeter and field soil profile were equipped with the same sensors in the diagnostic horizons with similar soil physical properties, the sensors monitor the soil water dynamics of only a small region of the soil. Thus, observed deviations in the SWC and soil water pressure head response between field and lysimeter soil (Fig. 3.4) may be caused by small-scale spatial heterogeneity (Guo & Lin, 2018; Lin & Zhou, 2008) or differences induced during horizontal insertion of sensors. Bravo et al. (2020) attributed periods without correlation between lysimeter and field to effects of small-scale spatial heterogeneity. Here, correlations could be interpreted similarly by heterogeneity effects except that correlations between field and lysimeter were shifted in time (Figs. 3.4–3.7).

The observed time lags between the increase in water content in the lysimeter and field (for example, in Figs. 3.5–3.9) might be explained by differences in the plant development. The lysimeter soil produced almost twice the biomass yield than that of the field in 2017 (Tab. 3.3). This larger yield may be attributed to LSF when assuming that more water can be stored in the lysimeter that could laterally move downwards in the field soil (Newman et al., 2004). However, the SWC in the lysimeter soil was lower than in the field, which is

consistent with a larger crop water use by a more intense plant growth at the lysimeter. Also, especially in winter and early spring (Figs. 3.4–3.7), the field soil could have received additional water by LSF from uphill positions, such that crop and root growth was limited during periods of higher pore water saturation (Herbrich et al., 2018).

The onset of the SWC increase after precipitation could also differ between field and lysimeter soil because of different initial SWC at the beginning of an event (e.g., Fig. 3.4, A1, spring 2017, 15-cm depth). Thus, the hydraulic conductivity of the field soil is initially higher than that of the lysimeter soil, possibly inducing a faster vertical movement as response to precipitation as compared with the lysimeter soil. In fact, the conditions for the onset of LSF, although requiring relatively high water saturation of the soil pore system, are mainly depending on the hydraulic potential gradients as the driving force for water movement in soils. Furthermore and also considering measurement uncertainty of the sensors, the absolute values of the SWC do not inform about pore water saturation (compare 15 and 80 cm in Fig. 3.5, B1, and Fig. 3.6, A1 and C1). Nevertheless, by applying WCA, it is possible to identify the timing of changes in the SWC (Liu et al., 2017), and differences in the flow dynamics between lysimeter and field. A more detailed quantitative analysis (Guo et al., 2018) requires soil water balance calculations considering the nonlinear soil hydraulic properties. The present analysis could help selecting out of long-term time series, the most appropriate periods for the follow-up detailed analysis (Lin & Zhou, 2008).

Despite limitations, the observed differences in soil water dynamics between lysimeter and field soil profile (Fig. 3.5) in the Ahb horizon (sensor in 80-cm depth) and in the colluvic soil horizon above (sensor in 60-cm depth) might be interpreted as LSF in the following way: a faster increase in SWC in the field than in the lysimeter soil in spring and autumn could be caused by water flowing from uphill positions when SWC in the profile increased sequentially. For example, during the event on 2 Nov. 2017, the SWC in 32- and 60-cm depth increased faster in the field as compared with the lysimeter (Fig. 3.5, C2, Tab. 3.4, and Fig. 3.8). For the values at the 60-cm depth, however, the response time between lysimeter and field was greater than at the 32-cm depth (Fig. 3.5, C2), indicated by the stronger deviation from the eastward direction (perfect correlation) of the time gap arrows at 60-cm depth as compared with the 32-cm depth. Since the FDR sensors at the 32- and 60-cm depth in the field responded sequentially, no vertical preferential flow did occur but the water must have entered the subsoil laterally (Lee & Kim, 2019; Xie et al., 2019). Also, the SWC increase at the 60-cm depth was more intense in the lysimeter than in the field (Fig. 3.5 C1, Fig. 3.9, E). Because of the lysimeter construction, infiltrating water could only move vertically downwards to the 60-cm depth, whereas in the field, the smaller increase in SWC could be explained by lateral water movement away from the sensor.

The assumption of LSF occurrence is also supported by analyzing the occurrence of response sequences (Graham & Lin, 2011; Wiekenkamp et al., 2016) in different depths for single precipitation events (Tab. 3.4, Fig. 3.8). On 1 Dec. 2016, the lysimeter increases faster in water content at the 15- and 32-cm depth than in the field, whereas in the deeper horizons, the SWC of field reacts earlier than SWC in the lysimeter (Fig. 3.7, A2). On 12 July 2017 and on 22 July 2017, the field soil reacted earlier than the lysimeter in the upper soil horizons in contrast with the lower horizons, where the SWC and soil water pressure head in the lysimeter increased faster than in the field (Figs.3.4, 3.6 and 3.8; Tab. 3.4). This indicates that in each horizon, different processes influence soil water dynamics such as swelling and shrinking in the upper two soil horizons (15- and 32-cm soil depth). Also, effects of different plant and root developments between the lysimeter and field are more pronounced in the upper soil horizons. A higher root density might favor the development of macropores for vertical preferential flow (Mitchell et al., 1995). The response sequences during the precipitation events (Tab. 3.4, Figs. 3.8 and 3.9), in deeper soil horizons were different from those of the upper ones, which could also be attributed to either LSF or vertical preferential flow.

In summer 2017, vertical preferential flow was also observed in the lysimeter and field soil profile throughout heavy precipitation events (Fig. 3.9, c and d) as in Filipović et al. (2018). It may be assumed that due to shrinkage during summer, the infiltrating water could move vertically through cracks (Greve et al., 2010) or along the cylinder walls (Corwin, 2000), leading to a faster increase in SWC and soil water pressure head in the lysimeter than in the field. The SWC in the field soil increased simultaneously at the 32- and 60-cm depth (Fig. 3.9, c and d). In the lysimeter, the FDR sensor at the 60-cm depth responded earlier than the FDR sensor at the 32-cm depth, indicating nonsequential preferential flow (Graham & Lin, 2011; Wiekenkamp et al., 2016). Since the SWC increase in the lysimeter at both depths was more intense (despite the generally lower total amount of SWC) than in the field, LSF may be assumed in combination with vertical preferential flow (Dasgupta et al., 2006; Xie et al., 2019). In their study on vertical preferential flow in the Wüstebach catchment (Eifel, Germany), Wiekenkamp et al. (2016) observed an increase in the nonsequential SWC responses with the amount of precipitation. Lin and Zhou (2008) could also relate vertical preferential flow to rain intensities in the Shale Hills catchment (Pennsylvania, USA).

The position of the observed soil profile at the hillslope was proposed as yet another factor contributing to the occurrence of lateral flow. Lee and Kim (2019) observed in a hillslope in Korea that vertical preferential flow was dominant in soils at uphill positions, whereas LSF occurred in soils at the lower slope positions. These authors identified LSF by the

wavelet coherency of the SWC between uphill and downhill positions; their coherence spectra revealed stronger relationships between greater than smaller distances and depths to be indicative for either bypass flow or boundary flows along bedrock. Liu and Lin (2015) also identified hilltops and valley floors as topographic controls enhancing preferential flow; here, the SWC time series at slope foot position could be affected by an increased water table (Fig. 3.7, A1, 80- and 140-cm depth).

One major disadvantage of the proposed method to identify LSF is that it is an indirect approach that does not show the soil water flow as for instance when using water tracers (Gerke et al., 2015; Laine-Kaulio et al., 2014; Wienhöfer & Zehe, 2014). Additionally, the analysis was impeded by a rather short time of a few months, where data were available due to sensor and logger failures. A longer uninterrupted time series could have given more insight in the occurrence of LSF on higher scales. Also, deviations in vegetation dynamics in lysimeter and field and differing absolute SWC values restricted the interpretation of the results. The SWC values alone may not be sufficient to conclude whether the conditions of SLF occurrence are met. Nevertheless, the WCA could be for hillslope hydrology (Lee & Kim, 2019) also a tool for soil hydrology applications to identify the timing of SWC changes providing qualitative information about changes in flux dynamics. The advantage is that the approach is nondestructive and applicable to already available larger data series that capture changes in water content and pressure heads, which is not possible if destructive techniques including tracer applications are used for the detection of LSF.

3.7   Conclusions

The aim of this study was to test whether the WCA is able to capture temporal shifts in the correlation between lysimeter and field data in the reaction of soil water state variables to precipitation and to analyze whether these deviations can be attributed to LSF.

The results based on correlation patterns between soil water dynamics in the lysimeter and field after precipitation events indicate that lysimeter and field soil did not react synchronously to precipitation. Thus, it seems possible to identify distinct periods of deviations from a long time series of water content or pressure heads to identify differences in the soil water dynamics with this setup.

In addition to possible LSF events vertical preferential flow could be observed as indicated by an earlier response in the lysimeter as compared with the field on rare events in summer. The phase shifts and periodicities indicated by the wavelet coherency spectra reflected the response times to rain events in the same depth of lysimeter and field soil. In the 3 yr (2016–2018), only a few periods could be identified, in which LSF was likely to occur because of dry weather conditions and limited data. The condensed information in wavelet coherency spectra are providing an overview of the temporal patterns of time shifts and correlations for data time series, and identifying potentially relevant periods for more detailed analyses.

3.8   Acknowledgments

3.9 References

Ad-hoc-Arbeitsgruppe Boden (Ed.) (2006). Bodenkundliche Kartieranleitung. KA5. Stuttgart, Germany: Schweizerbart Science Publishers.

Alaoui, A., Caduff, U., Gerke, H.H., & Weingartner, R. (2011). A Preferential Flow Effects on Infiltration and Runoff in Grassland and Forest Soils. Vadose Zone Journal, 10. https://doi.org/10.2136/vzj2010.0076

Biswas, A., & Si, B. C. (2011). Identifying scale specific controls of soil water storage in a hummocky landscape using wavelet coherency. Geoderma, 165(1), 50–59. https://doi.org/10.1016/j.geoderma.2011.07.002

Bravo, S., González-Chang, M., Dec, D., Valle, S., Wendroth, O., Zúñiga, F., & Dörner, J. (2020). Using wavelet analyses to identify temporal coherence in soil physical properties in a volcanic ash-derived soil. Agricultural and Forest Meteorology, 285-286, 1–10. https://doi.org/10.1016/j.agrformet.2020.107909

Corwin, D.L., 2000. Evaluation of a simple lysimeter-design modification to minimize sidewall flow. Journal of Contaminant Hydrology 42(1):35-49, https://doi.org/10.1016/S0169-7722(99)00088-1

Dasgupta, S., Mohanty, B.P. and Köhne, J.M. (2006), Impacts of Juniper Vegetation and Karst Geology on Subsurface Flow Processes in the Edwards Plateau, Texas. Vadose Zone Journal, 5: 1076-1085. https://doi.org/10.2136/vzj2005.0073

Falge, E., Baldocchi, D., Olson, R., Anthoni, P., Aubinet, M., Bernhofer, C., . . . Dolman, H. (2001). Gap filling strategies for defensible annual sums of net ecosystem exchange. Agricultural and Forest Meteorology, 107(1), 43–69.

Farge, M. (1992). Wavelet transforms and their applications to turbulence. Annual Review of Fluid Mechanics, 24(1), 395–458. https://doi.org/10.1146/annurev.fl.24.010192.002143

Filipović, V., Gerke, H. H., Filipović, L., & Sommer, M. (2018). Quantifying Subsurface Lateral Flow along Sloping Horizon Boundaries in Soil Profiles of a Hummocky Ground Moraine. Vadose Zone Journal, 17(1), 1–12. https://doi.org/10.2136/vzj2017.05.0106

Filipović, V., Coquet, Y., Gerke, H. H. (2019) Representation of plot scale soil heterogeneity in dual-domain effective flow and transport models with mass exchange. Vadose Zone Journal 18 (1), 1-14. https://doi.org/10.2136/vzj2018.09.0174

Gerke, H. H. (2006). Preferential flow descriptions for structured soils. Journal of Plant Nutrition and Soil Science, 169(3), 382–400. https://doi.org/10.1002/jpln.200521955

Gerke, H.H., Koszinski, S., Kalettka, T., and Sommer, M. 2010. Structures and hydrologic function of soil landscapes with kettle holes using an integrated hydropedological approach. J. Hydrol. 393(1–2), 123–132. https://doi.org/10.1016/j.jhydrol.2009.12.047

Gerke, K.M., Sidle, R.C., Mallants, D.(2015). Preferential flow mechanisms identified from staining experiments in forested hillslopes: Preferential Flow Mechanisms Identified from Staining Experiments. Hydrological Processes. 29, 4562–4578. https://doi.org/10.1002/hyp.10468

Graham, C. B., & Lin, H. S. (2011). Controls and Frequency of Preferential Flow Occurrence: A 175-Event Analysis. Vadose Zone Journal, 10(3), 816–831. https://doi.org/10.2136/vzj2010.0119

Greve, A., Andersen, M. S., & Acworth, R. I. (2010). Investigations of soil cracking and preferential flow in a weighing lysimeter filled with cracking clay soil. Journal of Hydrology, 393(1-2), 105–113. https://doi.org/10.1016/j.jhydrol.2010.03.007

Grinsted, A., Moore, J. C., & Jevrejeva, S. (2004). Application of the cross wavelet transform and wavelet coherence to geophysical time series. Nonlinear Processes in Geophysics, 11(5/6), 561–566. https://doi.org/10.5194/npg-11-561-2004

Groh, J., Diamantopoulos, E., Duan, X., Ewert, F., Herbst, M., Holbak, M., . . . Gerke, H. H. (2020). Crop growth and soil water fluxes at erosion-affected arable sites: Using weighing lysimeter data for model intercomparison. Vadose Zone Journal, 19(1). https://doi.org/10.1002/vzj2.20058

Groh, J., Vanderborght, J., Pütz, T., & Vereecken, H. (2016). How to control the lysimeter bottom boundary to investigate the effect of climate change on soil processes? Vadose Zone Journal, 15(7). https://doi.org/10.2136/vzj2015.08.0113

Guo, L., Fan, B., Zhang, J., & Lin, H. (2018). Occurrence of subsurface lateral flow in the Shale Hills Catchment indicated by a soil water mass balance method. European Journal of Soil Science, 69(5), 771–786. https://doi.org/10.1111/ejss.12701

Guo, L., & Lin, H. (2018). Addressing Two Bottlenecks to Advance the Understanding of Preferential Flow in Soils. Advances in Agronomy, 147, 61–117. https://doi.org/10.1016/bs.agron.2017.10.002

Guo, L., Mount, G.J., Hudson, S., Lin, H., Levia, D. (2020). Pairing geophysical techniques improves understanding of the near-surface Critical Zone: Visualization of preferential routing of stemflow along coarse roots. Geoderma, 357,. https://doi.org/10.1016/j.geoderma.2019.113953

Hannes, M., Wollschläger, U., Wöhling, T., & Vogel, H.-J. (2016). Revisiting hydraulic hysteresis based on long-term monitoring of hydraulic states in lysimeters. Water Resources Research, 52(5), 3847–3865. https://doi.org/10.1002/2015WR018319

Hendrickx, J., & Flury, M. (2001). Uniform and preferential flow mechanisms in the vadose zone. In National Research Council (Ed.), Conceptual Models of Flow and Transport in the Fractured Vadose Zone (pp. 149–187). Washington, DC: The National Academies Press.

Herbrich, M., & Gerke, H. H. (2017). Scales of Water Retention Dynamics Observed in Eroded Luvisols from an Arable Postglacial Soil Landscape. Vadose Zone Journal, 16(10), 1-17. https://doi.org/10.2136/vzj2017.01.0003

Herbrich, M., Gerke, H. H., Bens, O., & Sommer, M. (2017) Water balance and leaching of dissolved organic and inorganic carbon of eroded Luvisols using high precision weighing lysimeters. Soil & Tillage Research 165, 144-160.

Herbrich, M., Gerke, H. H., & Sommer, M. (2018). Root development of winter wheat in erosion-affected soils depending on the position in a hummocky ground moraine soil landscape. Journal of Plant Nutrition and Soil Science, 181(2), 147–157. https://doi.org/10.1002/jpln.201600536

Hopp, L., McDonnell, J. J., & Condon, P. (2011). Lateral Subsurface Flow in a Soil Cover over Waste Rock in a Humid Temperate Environment. Vadose Zone Journal, 10(1), 332–344. https://doi.org/10.2136/vzj2010.0094

Hu, W., & Si, B. C. (2013). Soil water prediction based on its scale-specific control using multivariate empirical mode decomposition. Geoderma, 193-194, 180–188. https://doi.org/10.1016/j.geoderma.2012.10.021

IUSS, (2006). World reference base for soil resources 2006: World Soil Resources Reports No. 103. FAO, Rome

Julich, D., Julich, S., & Feger, K.-H. (2017). Phosphorus fractions in preferential flow pathways and soil matrix in hillslope soils in the Thuringian Forest (Central Germany). Journal of Plant Nutrition and Soil Science, 180(3), 407–417. https://doi.org/10.1002/jpln.201600305

Kahl, G., Ingwersen, J., Nutniyom, P., Totrakool, S., Pansombat, K., Thavornyutikarn, P., & Streck, T. (2008). Loss of pesticides from a litchi orchard to an adjacent stream in

northern Thailand. European Journal of Soil Science, 59(1), 71–81. https://doi.org/10.1111/j.1365-2389.2007.00984.x

Kutschera, L., Lichtenegger, E., & Sobotik, M. (2009). Wurzelatlas der Kulturpflanzen gemäßigter Gebiete mit Arten des Feldgemüsebaues: DLG-Verlag.

Lamb, K.J., MacQuarrie, K.T.B., Butler, K.E., Danielescu, S., Mott, E., Grimmet, M., Zebarth, B.J. (2019). Hydrogeophysical monitoring reveals primarily vertical movement of an applied tracer across a shallow, sloping low-permeability till interface: Implications for agricultural nitrate transport. Journal of Hydrology, 573, 616-630, https://doi.org/10.1016/j.jhydrol.2019.03.075.

Laine-Kaulio, H., Backnäs, S., Karvonen, T., Koivusalo, H., & McDonnell, J. J. (2014). Lateral subsurface stormflow and solute transport in a forested hillslope: A combined measurement and modeling approach. Water Resources Research, 50(10), 8159–8178. https://doi.org/10.1002/2014WR015381

Lee, E., & Kim, S. (2019). Wavelet analysis of soil moisture measurements for hillslope hydrological processes. Journal of Hydrology, 575, 82–93. https://doi.org/10.1016/j.jhydrol.2019.05.023

Lin, H., & Zhou, X. (2008). Evidence of subsurface preferential flow using soil hydrologic monitoring in the Shale Hills catchment. European Journal of Soil Science, 59(1), 34–49. https://doi.org/10.1111/j.1365-2389.2007.00988.x

Liu, H., & Lin, H. (2015). Frequency and Control of Subsurface Preferential Flow: From Pedon to Catchment Scales. Soil Science Society of America Journal, 79(2), 362–377. https://doi.org/10.2136/sssaj2014.08.0330

Liu, Q., Hao, Y., Stebler, E., Tanaka, N., & Zou, C. B. (2017). Impact of Plant Functional Types on Coherence Between Precipitation and Soil Moisture: A Wavelet Analysis. Geophysical Research Letters, 44 (24), 12,197-12,207. https://doi.org/10.1002/2017GL075542

Lu, N., Kaya, B. S., & Godt, J. W. (2011). Direction of unsaturated flow in a homogeneous and isotropic hillslope. Water Resources Research, 47(2), 1–15. https://doi.org/10.1029/2010WR010003

Luo, Z., Niu, J., Xie, B., Zhang, L., Chen, X., Berndtsson, R., . . . Zhu, S. (2019). Influence of Root Distribution on Preferential Flow in Deciduous and Coniferous Forest Soils. Forests, 10(11), https://doi.org/10.3390/f10110986

Lv, M., Hao, Z., Liu, Z., & Yu, Z. (2013). Conditions for lateral downslope unsaturated flow and effects of slope angle on soil moisture movement. Journal of Hydrology, 486, 321–333. https://doi.org/10.1016/j.jhydrol.2013.02.013

MATLAB (Version 2019b) (2018). Natick, Massachusetts: The MathWorks Inc.

Mitchell, A. R., Ellsworth, T. R., & Meek, B. D. (1995). Effect of root systems on preferential flow in swelling soil. Communications in Soil Science and Plant Analysis, 26(15-16), 2655–2666. https://doi.org/10.1080/00103629509369475

Newman, B. D., Wilcox, B. P., & Graham, R. C. (2004). Snowmelt-driven macropore flow and soil saturation in a semiarid forest. Hydrological Processes, 18(5), 1035–1042. https://doi.org/10.1002/hyp.5521

Nyquist, J.E., Toran, L., Pitman, L., Guo, L. & Lin, H. 2018. Testing the fill-and-spill model of subsurface flow using GPR and Dye Tracing. Vadose Zone Journal, 17, 1–13.

Pütz, T., R. Kiese, U. Wollschläger, J. Groh, H. Rupp, S. Zacharias, et al. 2016. TERENO-SOILCan: a lysimeter-network in Germany observing soil processes and plant diversity influenced by climate change. Environmental Earth Sciences 75: 1-14.

R: A Language and Environment for Statistical Computing (Version R-3.6.2) (2019). Vienna, Austria. Retrieved from https://www.R-project.org

Rahmati, M., Groh, J., Graf, A., Pütz, T., Vanderborght, J., & Vereecken, H. (2020). On the impact of increasing drought on the relationship between soil water content and

evapotranspiration of a grassland. Vadose Zone Journal, 19(1), 1–20. https://doi.org/10.1002/vzj2.20029

Rieckh, H., Gerke, H. H., Siemens, J., & Sommer, M. (2014). Water and Dissolved Carbon Fluxes in an Eroding Soil Landscape Depending on Terrain Position. Vadose Zone Journal, 13(7), 1-14. https://doi.org/10.2136/vzj2013.10.0173

Rieckh, H., Gerke, H. H., & Sommer, M. (2012). Hydraulic properties of characteristic horizons depending on relief position and structure in a hummocky glacial soil landscape. Soil and Tillage Research, 125, 123–131. https://doi.org/10.1016/j.still.2012.07.004

Ritter, A., Regalado, C. M., & Muñoz-Carpena, R. (2009). Temporal Common Trends of Topsoil Water Dynamics in a Humid Subtropical Forest Watershed. Vadose Zone Journal, 8(2), 437–449. https://doi.org/10.2136/vzj2008.0054

Si, B. C. (2008). Spatial Scaling Analyses of Soil Physical Properties: A Review of Spectral and Wavelet Methods. Vadose Zone Journal, 7(2), 547–562. https://doi.org/10.2136/vzj2007.0040

Si, B. C., & Zeleke, T. B. (2005). Wavelet coherency analysis to relate saturated hydraulic properties to soil physical properties. Water Resources Research, 41(11), 1–9. https://doi.org/10.1029/2005WR004118

Sidle, R. C., Noguchi, S., Tsuboyama, Y., & Laursen, K. (2001). A conceptual model of preferential flow systems in forested hillslopes: evidence of self-organization. Hydrological Processes, 15(10), 1675–1692. https://doi.org/10.1002/hyp.233

Sommer, M., Augustin, J., & Kleber, M. (2016). Feedbacks of soil erosion on SOC patterns and carbon dynamics in agricultural landscapes—The CarboZALF experiment. Soil and Tillage Research, 156, 182–184. https://doi.org/10.1016/j.still.2015.09.015

Torrence, C., & Compo, G. P. (1998). A Practical Guide to Wavelet Analysis. Bulletin of the American Meteorological Society, 79(1), 61–78. https://doi.org/10.1175/1520-0477(1998)079<0061:APGTWA>2.0.CO;2

Torrence, C., & Webster, P. J. (1999). Interdecadal changes in the ENSO–monsoon system. Journal of Climate, 12(8), 2679–2690.

Umwelt-Geräte-Technik GmbH (2013). UGT - Novel Lysimeter-Techiques. Retrieved from www.ugt-online.de

Villazón, M. F., & Willems, P. (2010). Filling gaps and daily disaccumulation of precipitation data for rainfall-runoff model. In MagnaSken, Skopje (Hg.) – Proc. 4th Int, Ohrid, Republic of Macedonia.

Wiekenkamp, I., Huisman, J. A., Bogena, H. R., Lin, H. S., & Vereecken, H. (2016). Spatial and temporal occurrence of preferential flow in a forested headwater catchment. Journal of Hydrology, 534, 139–149. https://doi.org/10.1016/j.jhydrol.2015.12.050

Wienhöfer, J., & Zehe, E. (2014). Predicting subsurface stormflow response of a forested hillslope – the role of connected flow paths. Hydrology and Earth System Sciences, 18(1), 121–138. https://doi.org/10.5194/hess-18-121-2014

Wienhöfer, J., Lindenmaier, F., & Zehe, E. (2011). Challenges in Understanding the Hydrologic Controls on the Mobility of Slow-Moving Landslides. Vadose Zone Journal, 10(2), 496–511. https://doi.org/10.2136/vzj2009.0182

Wilcox, B. P., Newman, B. D., Brandes, D., Davenport, D. W., & Reid, K. (1997). Runoff from a semiarid Ponderosa pine hillslope in New Mexico. Water Resources Research, 10(33), 2301–2314.

Wittenberg, H., Aksoy, H., & Miegel, K. (2019). Fast response of groundwater to heavy rainfall. Journal of Hydrology, 571, 837–842. https://doi.org/10.1016/j.jhydrol.2019.02.037

Wittenberg, H.; Aksoy, H.; & Miegel, K. (2020). The rapid rise of groundwater after heavy rainfalls. (German title: Der schnelle Anstieg des Grundwassers nach Starkregen). Hydrol. Wasserbewirtsch. 2020, 64, 66–74.

Wu, W., Geller, M. A., & Dickinson, R. E. (2002). The Response of Soil Moisture to Long-Term Variability of Precipitation. Journal of Hydrometeorology, 3(5), 604–613. https://doi.org/10.1175/1525-7541(2002)003<0604:TROSMT>2.0.CO;2

Xie, M., Šimůnek, J., Zhang, Z., Zhang, P., Xu, J., Lin, Q. (2019). Nitrate subsurface transport and losses in response to its initial distributions in sloped soils: An experimental and modelling study. Hydrological Processes. 33, 3282– 3296. https://doi.org/10.1002/hyp.13556

Yang, Y., Jia, X., Wendroth, O., & Liu, B. (2018). Estimating Saturated Hydraulic Conductivity along a South-North Transect in the Loess Plateau of China. Soil Science Society of America Journal, 82(5), 1033–1045. https://doi.org/10.2136/sssaj2018.03.0126

Yang, Y., Wendroth, O., & Walton, R. J. (2016). Temporal Dynamics and Stability of Spatial Soil Matric Potential in Two Land Use Systems. Vadose Zone Journal, 15(8), 1-15. https://doi.org/10.2136/vzj2015.12.0157

4   Tracing lateral subsurface flow in layered soils by undisturbed monolith sampling, targeted laboratory experiments, and model-based analysis

4.1   Core Ideas

- A Laboratory method to induce and quantify lateral subsurface flow (LSF) is presented.
- The experimental setup is verified by modeling with HYDRUS 2D.
- Sampling of rectangular soil monoliths for 2D flow experiments is improved.
- LSF and hydraulic nonequilibrium conditions are observed.
- The experimental data allow for improving models on the onset of LSF.

4.2   Abstract

Lateral subsurface flow (LSF) is a phenomenon frequently occurring in the field induced by local water saturation along horizon boundaries under nonequilibrium conditions. However, observations of LSF in undisturbed soils under controlled irrigation in the laboratory are limited but needed for model improvement, prediction, and quantification of LSF. We present a method for extracting an undisturbed soil monolith along a soil horizon boundary and introduce an experimental setup for the measurement of LSF and an irrigation device for simulating rainfall. An experimental test run was simulated using HYDRUS 2D. Water infiltrating into the monolith and flowing either laterally along the horizon boundary or vertically through the bottom horizon could be separately captured by suction discs at the side and the bottom. Thus, a clear distinction between lateral and vertical flow was possible. Pressure heads and water contents were recorded by tensiometers and frequency domain reflectometry (FDR) sensors distributed across the monolith in a regular two-dimensional, vertical, cross-sectional pattern. Sensor readings indicated the presence of nonequilibrium conditions within the monolith. Modeling results could reproduce the lateral and vertical outflow of the monolith under constant irrigation, thus showing that water flow within the monolith under steady-state conditions can be explained by the Richards equation and the van Genuchten–Mualem model. The presented method can be used to improve and verify models designed for the prediction of the onset of LSF including that induced by local nonequilibrium conditions.

4.3 Introduction

A lateral redirection of water flow can occur along textural and other boundaries in the subsoil of sloping landscapes (Guo & Lin, 2018) or as interflow in forested hillslopes (Sidle et al., 2001). The lateral subsurface flow (LSF) can be a highly efficient shortcut for the movement of water and solutes such as plant nutrients and pesticides (Julich et al., 2017; Kahl et al., 2008; Potter et al., 2015). Despite ample evidence (H. H. Gerke et al., 2010; K. M. Gerke et al., 2015; Hardie et al., 2012; Laine-Kaulio et al., 2014; Liu & Lin, 2015; McNamara et al., 2005; Schwärzel et al., 2012; Wienhöfer & Zehe, 2014; Wöhling et al., 2012), observation and modeling of LSF are challenging due to the highly nonlinear, threshold-like onset of LSF, especially when based on local changes in the water potential (Filipović et al., 2018; Lv et al., 2013).

Water infiltration in unsaturated soil is mainly vertical (Hillel, 1987), because the hydraulic gradient is composed of nondirectional capillary forces and gravity pointing downwards. When the soil gets saturated (pressure heads approaching zero), capillary forces vanish and lateral downslope flows may be initiated above waterlogging layers (Lin et al., 2006). Because of preferential flow and local hydraulic nonequilibrium conditions, the critical point of zero water potential might be reached well before the soil is completely water saturated (Hannes et al., 2016).

Previous studies assumed that preferential flow along macropores (e.g., H. H. Gerke, 2006; Jarvis, 2007) could lead to local water saturation in regions where these pores were ending, and thus, such nonequilibrium flow conditions may initiate higher saturation above impeding soil horizons (Newman et al., 2004; Noguchi et al., 1999; Redding & Devito, 2010). The resulting transient local saturations in these soil regions could initiate LSF when located in sloping soil landscapes (Lin et al., 2006).

Experimental verifications are still limited because the subsurface flow field cannot easily be detected in situ (e.g., Allaire et al., 2009; Ehrhardt et al., 2021). Attempts made by geophysical approaches to identify LSF are limited in the spatial resolution to identify the onset (Di Prima et al., 2020; Guo et al., 2014; Leslie & Heinse, 2013; Nyquist et al., 2018). Also, the scale of observation needs to be accounted for: despite LSF occurring in hillslopes at the field scale (Buttle & McDonald, 2002; Lin et al., 2006; Redding & Devito, 2010; Wöhling et al., 2012), the onset of LSF was only observed in the laboratory at smaller scales (Lv et al., 2013; Sinai & Dirksen, 2006). Lateral subsurface flow may occur at various scales; however, capturing it experimentally seems to be more challenging, especially for the larger scales that are difficult to reproduce in the laboratory.

In the laboratory, several problems are strongly limiting the observation of LSF. For sampling of intact soil samples of the relevant size, special extraction equipment and encasings need to be constructed (Germer & Braun, 2015). One of the main issues is the separate collection of vertically and laterally moving soil water. The design of a laboratory setup for the model-based analyses requires a controllable irrigation system for water and tracer solutions (e.g., Sobotkova & Snehota, 2014) together with special spatial arrangements and sensor resolutions to be able to identify the local nonequilibrium conditions and separately control and quantify the vertical and lateral soil water fluxes (Fox et al., 2018).

In several studies, samples consisting of artificially compacted soil of homogeneous grain size have been used to observe LSF under controlled conditions in the laboratory (Fox et al., 2018; Guertault & Fox, 2020; Miyazaki, 1988; Sakaki et al., 2011). Miyazaki (1988) proved the occurrence of LSF along textural boundaries in layered, sloped, and artificially compacted sandy loam soil samples with a layer of less compacted plant material. Evidence for LSF in artificially packed unsaturated sands was observed by Sinai and Dirksen (2006). Guertault and Fox (2020) observed LSF induced by artificial macropores in a homogeneous soil over a gravel layer. Percolation experiments using soil columns with artificial macropores have also been conducted by Köhne and Mohanty (2005) and Castiglione et al. (2003) to quantify macropore and matrix flow, as well as the interdomain water transfer. Macropore induced flow along texture contrasting layers (Lin et al., 2006) was observed in the field (Noguchi et al., 1999) and has also been observed in laboratory experiments after drilling artificial macropores down to the horizon boundary (Guertault & Fox, 2020). Sakaki et al. (2011) developed an experimental scheme to simultaneously determine the two-dimensional (2D) distribution of soil water content (SWC) and soil water potential in a soil monolith to assess water retention during wetting and drainage cycles. As presented above, most of the experimental studies focusing on LSF quantification have been done on artificially constructed soils, which certainly affect soil pore network and architecture that play an important role under field conditions, especially in arable soils.

For quantifying LSF dynamics, numerical models have been developed and applied. Guo et al. (2019) studied preferential flow in unsaturated saprock in forested hillslopes and proposed a three-dimensional (3D) fill-and-spill model that described the importance of subsurface flow. These authors identified shallow saprock and concave hillslopes as essential controls governing the hillslope subsurface flow. Dušek and Vogel (2014) presented two modeling approaches (one-dimensional [1D] vs. 2D) for quantification of hillslope discharge data (subsurface runoff) collected in an experimental trench. The two model approaches resulted in similar hillslope discharge hydrographs, characterized by

short-term runoff peaks followed by zero-discharge periods, but the 2D model showed closer agreement between observed and simulated soil water pressure heads near the trench (subsurface runoff collection system). In a similar study, Dušek et al. (2012) studied preferential subsurface flow on a hillslope scale by combining a 1D vertical dual-continuum approach with a 1D Boussinesq-type lateral flow equation. They concluded that the physically based combined modeling allows for a reliable description of both preferential flow in a 1D vertical soil profile and lateral subsurface hillslope flow. In their study, Filipović et al. (2018) used HYDRUS 2D to quantify the potential for subsurface lateral flow depending on the erosion-affected spatial hydropedological complexity. It was shown that lateral flow was increasing with decreasing solum thickness, indicating an erosion-induced feedback on LSF, which was sensitive to the soil moisture regime prior to rainstorms during which LSF occurred. These modeling examples proved the necessity to design experiments for LSF quantification, which could help understanding of LSF in arable fields and improving modeling capabilities in reproducing LSF numerically.

An experimental setup that allows generating LSF in natural soil monoliths under local nonequilibrium conditions is still needed because data are missing to parameterize and test models that incorporate non-equilibrium conditions. Such conditions could be induced by macropores continuing vertically through compacted layers in the subsurface.

The objectives of the present study were to develop and test an experimental 2D setup that allows a quantitative investigation of LSF in intact unsaturated soil monoliths with particular emphasis on the initiation of local nonequilibrium conditions to provide datasets for model-based analysis under controlled conditions. The idea of the novel experimental setup was to combine the bottom suction plate with a suction-plate drainage system at the expected lateral flow side, and an irrigation system complemented by a relatively dense arrangement of water content and pressure head sensors (c.f., Sakaki et al., 2011) to obtain spatially distributed information about local soil hydraulic properties. The setup required extraction of intact soil monolith samples with contrasting soil horizons in sloping field soil and the transfer of the monolith into transparent casings without disturbance of the pore structure. The experimental data of LSF should allow the simulation with a 2D numerical model to verify the experimental setup. With this measurement setup, we want to determine whether it is possible to measure and visualize LSF in undisturbed soil monoliths under equilibrium and nonequilibrium conditions. Modeling with HYDRUS 2D is carried out in order to test the experimental setup under steady-state flow.

4.4 Materials and Methods

4.4.1 Soil sampling

The soil was extracted at the CarboZalf-D experimental field of the Leibniz-Centre for Agricultural Landscape Research (ZALF), Müncheberg (Sommer et al., 2016), as a subsequent study of Filipović et al. (2018). The field site is located in a hummocky ground moraine soil landscape (53°23′ N, 13°47′ E; 50–60 m asl). The horizon boundary from a CBkg to a Bgk1 horizon of a Haplic Regosol (calcaric) was chosen for the analysis of LSF because of higher vertical and horizontal hydraulic conductivities in the CBkg horizon in contrast with the Bgk1-horizon, as we noted that on this specific boundary LSF could occur in specific conditions (Filipović et al., 2018).

The soil in both horizons was classified as a loamy sand (Rieckh et al., 2012). The horizontal hydraulic conductivity, K_h (cm d^{-1}), at a pressure head, h (cm), of $h = -1$ cm, close to saturation was 18.4 cm d^{-1} for the CBkg horizon (26-to-48-cm depth). The value was about three times larger than that of the Bgk1 horizon (48-to-85-cm depth). The K_h values were larger in both horizons than those of their respective vertical hydraulic conductivity, K_v (cm d^{-1}) (Tab. 4.1). The hydraulic conductivities were determined by throughflow experiments with tension disc infiltrometers.

Table 4.1: Soil physical characteristics of the sampled horizons of the Haplic Regosol (calcaric): classification according to FAO classification (IUSS, 2006); equivalent particle size of organic carbon-free and carbonate-free sieved (<2 mm) soil for sand (2--0.063 mm), silt (0.063--0.002 mm), and clay (<0.002 mm) (Rieckh et al., 2012); soil bulk density, ρ_b; soil hydraulic conductivity in vertical, K_v, and horizontal, K_h, direction measured at pressure head of h = −1 cm; and anisotropy ratio K_v/K_h

Hori-zon	Depth	Sand	Silt	Clay	ρ_b	K_h	K_v	K_v/K_h
	[cm]		[g kg^{-1}]		[g cm^{-3}]	[cm d^{-1}]		
CBkg	26--48	614	267	118	1.76 (0.06)	18.4 (19.5)	11.0 (10.3)	0.59
Bgk1	48--85	612	270	118	1.73 (0.07)	5.9 (9.5)	2.7 (0.8)	0.36

4.4.2 Soil monolith extraction procedure

For the soil monolith extraction procedure a 12-cm × 24-cm × 10-cm steel frame was constructed with sharpened chamfered edges at the bottom. A carbonate glass box was attached on top of the steel frame with metal angles and screws. Between the metal frame and the carbonate glass box, a 6-mm space was left with a bold nut for insertion of a bottom plate (Fig. 4.1a).

The sample was taken on 19 Oct. 2019 at 22-to-72-cm depth below the ground surface. A 3-m-long, 1.5-m-wide, and 1-m-deep pit was dug at the edge of the adjacent agricultural field. At the 3-m-long edge of the pit, the upper 22 cm of soil was removed to capture the horizon boundary approximately in the middle of the carbonate glass box. The soil around

the soil monolith sample was excavated manually at the three sides, and the fourth side was the soil pit (already open). The metal frame with the attached carbonate glass box was carefully pressed vertically downwards (Fig. 4.1a), such that the intact soil monolith progressively entered the 24-cm × 25-cm × 12-cm box (Fig. 4.1b). After reaching the targeted depth, the soil monolith was cut at the bottom from the intact soil by inserting a chamfered steel plate (Fig. 4.1c) that was then tightly attached to the monolith in the box using a strap.
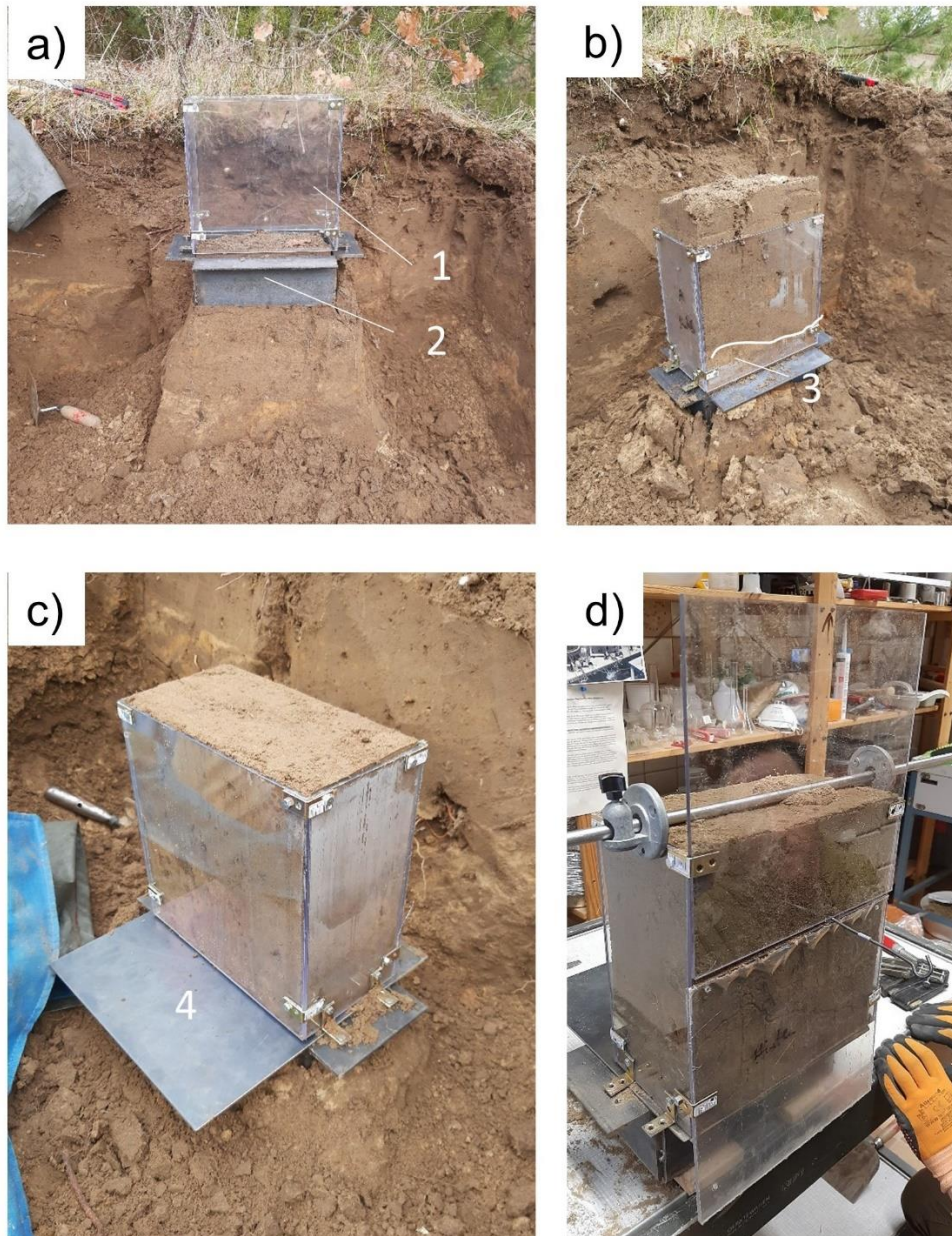
Figure 4.1: Extraction procedure of the soil monolith: (a) pressing of the carbonate glass box (1) on top of the metal frame (2) into the ground; (b) carbonate glass box filled with soil but still attached at the bottom to the ground with the horizon boundary (3); (c) cutting of the soil from the ground at the bottom of the carbonate glass box with the bottom plate (4); (d) exchanging of the side walls for sensor installation.

In addition, three intact 100-cm³ soil cores (5-cm diam.) were sampled in the two soil horizons to gravimetrically determine the volumetric SWC at the time of extraction, θ (cm^3 cm^{-3}), and the soil bulk density, ρ_b (cm d^{-1}), after oven drying for 24 h at 105 °C.

In the laboratory, the final positions for installing the sensors were determined after checking the proposed, regularly spaced locations for stones or other obstructions (e.g., at tensiometers between artificial macropores in the upper and lower row, stones were found so that the sensors had to be moved). Then, carbonate glass plates with holes for the sensors were prepared according to the scheme and the location of the soil horizons (i.e., CBkg and Bgk1). Finally, the carbonate glass plates at the sides were replaced by those with the holes for the sensors by carefully sliding the old plate downwards and at the same time inserting the new plate from the top (Fig. 4.1d).

4.4.3   Monolith setup

After the monolith was transferred into the carbonate glass box, it was placed on a bottom tension disc (inner edges: 15 cm × 30 cm × 0.6 cm) to drain the soil monolith (Appendix A4.1). At the left side, a second tension disc (inner edges: 10 cm × 10 cm × 1.0 cm) was attached in a distance of 6 cm from the bottom near the horizon boundary in order to drain water flowing laterally (Fig. 4.2). This tension disc was used to capture the LSF above the CBkg/Bgk1 horizon boundary. The tension discs (Walter Weissig) covered a total area of 100 cm² and were connected via silicon pipes to leveling vessels that allowed for the adjustment of soil water pressure head at the side and the bottom of the monolith. The leveling vessels could be moved upward and downward by laboratory lifting tables. Water was removed from the leveling vessels via a side outlet and pipes to containers placed on scales to measure the rate of water drained from the monolith (Fig. 4.2). The measurements were recorded in 3-min intervals by a DELTA data logger (DN Meßtechnik).

The tension discs consisted of a Plexiglas disc with a rectangular Plexiglas frame glued on top. Within this frame, a gridded polyvinyl chloride (PVC) mesh similar to a fly screen was laid in several layers (later proven to be problematic due to the flexible structure, see Section 3). The tension discs were sealed on top of the Plexiglas frame by a fine gaze material (Saatifil polyamide, PA31/21, mesh size = 31 µm, air permeability [20-mm water column] = 2,300.l m^{-2} s^{-1}). The gaze material was glued to the Plexiglas frame with epoxy resin. Both Plexiglas discs contained two holes: one in the middle of the disc for filling the disc with water and discharging the water from the monolith, and a second hole in one corner of the Plexiglas disc to remove the air from the disc while it was drained (Fig. 4.2). The air entry point of the plates is dependent on the pore size of the gaze material and lies between −30 and −50 cm. The construction of the tension discs was carried out, which

were similar to the tension disc infiltrometer described by Cook (2006), who used a Buchner funnel to apply a certain pressure head at the bottom of a soil core.
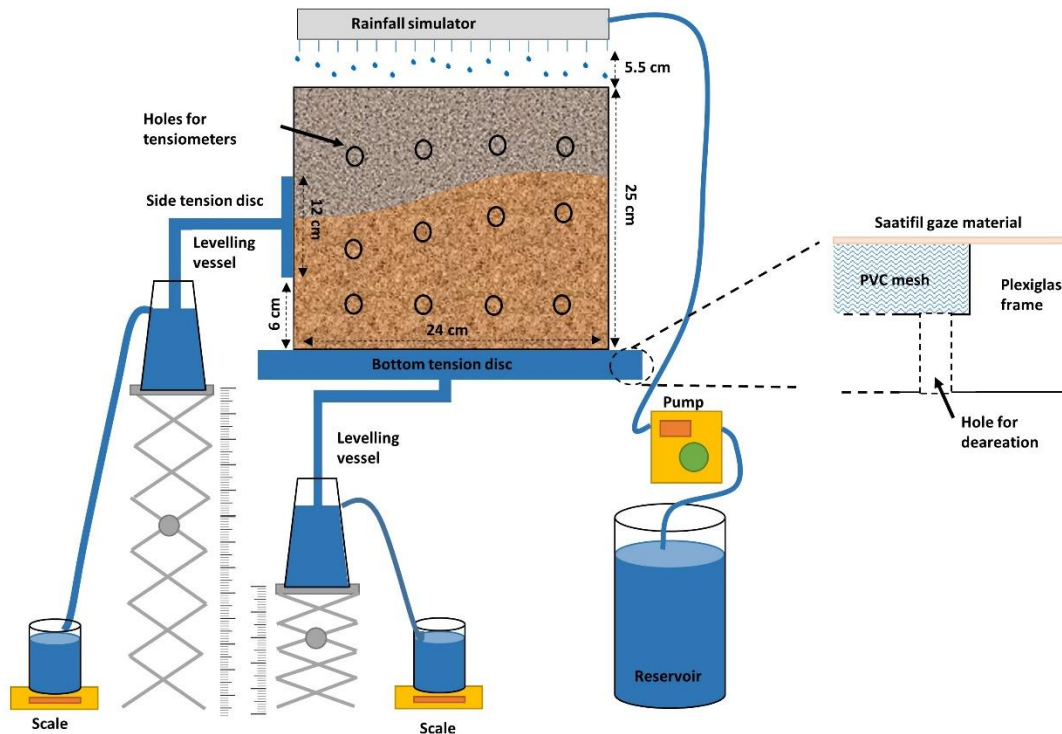
Figure 4.2: Scheme of the monolith measurement setup. The soil monolith is supplied with water via a capillary rainfall simulator connected to a water reservoir and a pump. The water is drained from the soil at the side and at the bottom by tension discs. Tension is adjusted by the leveling vessels. The amount of the drained water is captured with a container placed on the scale. PVC, polyvinyl chloride.

Twelve tensiometers (T5, METER Group) with a shaft length of 7 cm, a shaft diameter of 0.5 cm, and a ceramic tip surface area of 0.5 cm² were installed horizontally at one side of the monolith by carefully drilling the holes (diameter = 0.5 cm, depth = 6 cm) in the soil monolith, so the sensor tips were placed in the middle of the monolith (Appendix A4.1). Three rows of tensiometers were installed with four tensiometers in each row. The upper row was located above the horizon boundary and the other two rows below the horizon boundary (Fig. 4.3). On the opposite side of the monolith, six frequency domain reflectometry (FDR) sensors (ECH$_2$O EC-5 volumetric water content sensors, METER Group; length = 8.9 cm, width = 1.8 cm, height = 0.7 cm) were installed horizontally with the narrow side up in the spaces between the tensiometers (see Fig. 4.3 for the exact positions). The sensor placement was carried out in order to avoid the disruption of vertical flow as minimal as possible and to fit more tensiometers between the FDR sensors

(Appendix A4.1). The number of tensiometers installed at the horizon boundary (four) was constrained by the space required for FDR sensor placement while minimizing the disturbance of the soil structure. In addition, the space for the artificial macropore had to be reserved in the monolith. Both, FDR sensors and tensiometers were connected to a DT80 Series 4 data logger (dataTaker). Measurements were recorded at 1-min intervals.
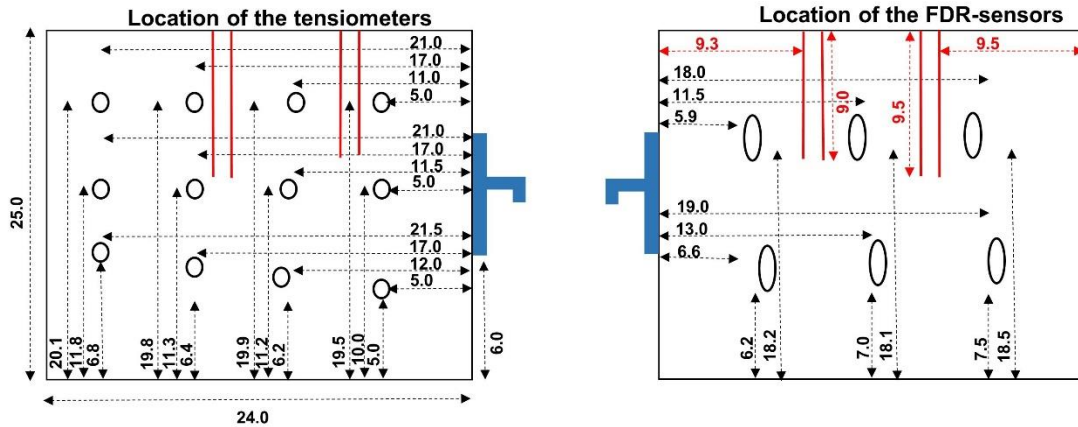
Figure 4.3: Scheme of the exact sensor placement in the soil monolith for the tensiometers (T5) (left) and the frequency domain reflectometry (FDR) sensors (EC5, right).

To supply the soil monolith with water, a rainfall simulator was constructed, similar to the one proposed by Sobotkova and Snehota (2014). It consisted of a distributor vessel that was connected to a water reservoir. "Heidelberg" elongations with capillary needles (diameter = 0.4 mm, length = 25 mm) were screwed into the 35 openings of the distributor vessel with a Luer-lock system. The needles were placed into holes in a regular grid in a carbonate glass plate mounted on top of the soil monolith. The distance between the lower end of the needles and the monolith was 5.5 cm. The water was pumped from the water reservoir into the distributor vessel by a peristaltic pump (LAMBDA MAXIFLOW, LAMBDA CZ, s.r.o.).

4.4.4 Sensor calibration procedures

The ECH$_2$O EC-5 volumetric water content sensors (EC5 sensors) were calibrated by installing the sensors horizontally into sieved, air-dried soil from the two soil layers, where the monolith was extracted (PVC cylinder volume = 424.74 cm³; height = 5 cm; inner diameter = 10.4 cm). The soil was saturated for 6 d and exposed to evaporation on a scale CP 2202 S (Satorius; precision = 0.01 g) to determine the gravimetric water content. The FDR sensor readings and gravimetric volumetric water content were related in a quadratic relationship to derive the sensor calibration curve.

The T5 tensiometers were calibrated by applying well defined pressures in the range from 0 to −100 cm using a calibration unit. Applied pressures and sensor readings were used to determine the offset between the actual pressure and the values measured by the tensiometers and used for bias correction.

4.4.5 Experimental procedures and data analysis

First, the monolith was subjected to a constant precipitation rate of 1,200 ml d^{-1} (41.7 L m^{-2} d^{-1}). The rainfall rate was adjusted, so the vertical and horizontal saturated conductivity of the lower horizon was reached. In the long run, this should lead to water saturation in the lower layer and lateral flux on top of it. The constant rate of rainfall was applied until steady state (the sensor readings did not change anymore for 24 h).

The water level of the bottom tension disc was adjusted to −5 cm with the leveling vessel (Fig. 4.2). The side tension disc was set to −20 cm in order to create a sufficient gradient that would lead to the discharge of water flow laterally along the soil horizon boundary. This pressure was determined experimentally. It corresponds to the value at which the first lateral water flow could be measured in our experimental setup. This experiment should demonstrate the ability of the measurement setup to discharge LSF along the horizon boundary.

In a second experiment, two holes (diameter = 0.8 cm) were drilled into the monolith from above representing earthworm burrows reaching down to the horizon boundary (Fig. 4.3) similar to Guertault and Fox (2020). By only filling the holes with water, an artificial local saturation was created, possibly leading to LSF. The macropores had a length of 9–9.5 cm and were located in the middle of the monolith (9.3–9.5 cm from each end). The distance between the macropores was approximately 3.6 cm. Before the experiment, the soil was close to saturation, with pressure heads around −11 to −12 cm in the lower part of the monolith (close to bottom suction plate) and −15 to −17 cm in the uppermost row of the tensiometers. Contour plots of the hydraulic potential were calculated from the measurements of pressure head indicating the direction of water flow. In each hole, 7 ml of 5 g L^{-1} Brilliant Blue dye was inserted and flushed with 48 ml of deionized water to facilitate the propagation of the dye while the rainfall simulator was turned off. The monolith was cut afterwards in 5-mm slices from the top to −11.5 cm to document the distribution of the dye. The cutting was performed with a diamond cutting wire (diameter = 0.2 mm) fastened in a clamping device. To make sure that even slices of 0.5-cm thickness were cut in every step, PVC discs with the size of the monolith cross-section and a height of 0.5 cm were inserted from the bottom of the monolith. Thus, the monolith was pushed 0.5 cm up and above the upper edge of the carbonate glass box, which served as a frame

for cutting the soil evenly. To verify the calibration of the FDR sensors, small (4 cm × 5 cm × 0.5 cm) samples in the layer where the FDR sensors were installed were analyzed for the SWC of the upper row of FDR sensors.

After each slice was removed, a photo was taken with Canon EOS 1000D (10 MPx and 72 dpi). Photos were taken on an illuminated desk with the camera adjusted in a frame to achieve for each photo similar illumination conditions and a similar distance from the camera to the monolith surface. From each slice, a defined volume of the soil was cut and dried at 105 °C to analyze the SWC.

Data analysis and visualization of the contour plots and gradients was carried out with the software R version 3.6.2 (R Core Team, 2019). The hydraulic head was calculated from the sum of the pressure heads and the gravitational potential. Interpolation between the 12 points of the hydraulic potential was performed by bivariate interpolation according to Akima (1978) available in R in the akima package version 0.6-2.1. To visualize the flow direction, gradients of the hydraulic potentials were calculated in *x* and *z* direction and plotted as arrows with the ggplot2 package version 3.3.2. The evaluation of the tracer experiment pictures were downsized from 10 to 1 MPx with FastStone Photo Resizer version 4.3 (FastStone Corporation, 2019). The images were loaded into the image processing tool Fiji (ImageJ 1.53c, National Institutes of Health; Schindelin et al., 2012). Pixels in the images were classified into three classes: noncolored soil, colored soil, and pore system (i.e., holes and cracks in order to separate the colored soil from the noncolored areas). The images were scaled, and the blue-stained area was reconstructed as a 3D representation with the 3D Viewer plugin.

4.4.6 Numerical modeling

Simulation of water flow was performed using the HYDRUS-2D software (Šimůnek et al., 2016; version 2.04.0580, released April 2015). Water flow was simulated according to the Richards equation:

$$\frac{\partial \theta}{\partial t} = \frac{\partial}{\partial x_i}\left[K(h)\left(K_{i,j}^{\mathrm{A}}\frac{\partial h}{\partial x_j} + K_{i,z}^{\mathrm{A}} \right) \right] \tag{4.1}$$

with θ as the volumetric water content [L³ L^{-3}], *t* as time [T], *h* as the pressure head [L], x_i (*i* = 1, 2) as the spatial coordinates [L] with $x_1 = x$ and $x_2 = z$ (vertical), $K_{i,j}^{\mathrm{A}}$ are components of the dimensionless hydraulic conductivity anisotropy tensor, $\mathbf{K}^{\mathrm{A}}$, $K(h)$ is the unsaturated hydraulic conductivity function [L T^{-1}]. The single porosity model according to van Genuchten–Mualem with an air-entry value of −2 cm was chosen. As demonstrated by

Ippisch et al. (2006), such a modification is required for the application of the van Genuchten–Mualem model in case the *n* parameter is <2, as is the case here. This modification is a very minor change in the shape of the water retention curve near saturation but significantly affects the shape of the conductivity function close to water saturation, leading to an improved stability of the numerical solution of Richards' equation as demonstrated by Vogel et al. (2001). Hysteresis was neglected in the simulation scenarios, and root water uptake was set to zero as no plants were involved in the experiment.

Because the hydraulic conductivity anisotropy tensor, K^A, is assumed to be symmetric, it is possible to define at any point in the flow domain a local coordinate system for which the tensor K^A is diagonal. The diagonal entries K_1^A and K_2^A of K^A are referred to as the principal components of K^A and represent scaling factors for the hydraulic conductivity in the *x* and *z* direction.

The soil hydraulic functions θ(*h*) and *K*(*h*) are described with the constraint single porosity van Genuchten–Mualem model with air entry of $h_a = -2$ cm as

$$\theta(h) = \theta_r + \frac{\theta_s - \theta_r}{\left(1 + |\alpha h|^n\right)^m} \text{ for } h < h_a$$

$$\theta(h) = \theta_s \text{ for } h \geq h_a \tag{4.2}$$

$$K(h) = K_s K_r^l \left[1 - \left(1 - S_e^{\frac{1}{m}} \right)^m \right]^2 \tag{4.3}$$

$$S_e = \frac{\theta - \theta_r}{\theta_s - \theta_r} \tag{4.4}$$

$$m = 1 - \frac{1}{n}; n > 1 \tag{4.5}$$

where θ_r and θ_s denote residual and saturated volumetric water content [L^3 L^{-3}], respectively, K_s is the saturated hydraulic conductivity [L T^{-1}], as stated above, S_e is the effective saturation, α [L^{-1}] and *n* [–] are shape parameters, and the preconnectivity parameter is *l* = 0.5.

The two layers of the monolith were parametrized as shown in Tab. 4.2. Parameter estimates (θ_r, θ_s, α, and *n*) were derived from soil textural information using a neural-

network-based pedotransfer function approach (i.e., Rosetta Lite DLL implemented into HYDRUS code; Schaap et al., 2001) with few parameters optimized throughout the model adaption (i.e., θ_s). K_1^A was derived from the ratio of hydraulic conductivities in the horizontal and vertical direction experimentally determined (Tab. 4.1).

Table 4.2: Manually adjusted soil hydraulic model parameters for the water flow simulation scenarios.

Horizon	θ_r	θ_s	α	*n*	K_s	K_1^A
	[cm³ cm⁻³]		[cm⁻¹]	[]	[cm d⁻¹]	[]
CBkg	0.037	0.26	0.0431	1.3	11.0	1.670
Bgk1	0.033	0.21	0.0552	1.2	2.7	2.185

At the top soil surface of the monolith, an atmospheric surface boundary condition was assumed. A rainfall rate of 4.17 cm d⁻¹ was applied similar to the laboratory experiments. At the bottom, a seepage face condition was applied. No-flow boundary conditions were imposed at the left and right sides of the monolith except for the location of suction disc where a variable flux condition with a pressure head of −20 cm was applied. The initial conditions for the hydraulic potential were set to −5 cm at the bottom with a hydrostatic equilibrium distribution along the soil profile. The simulation was carried out until approaching steady-state flow conditions in the soil, which was after 24 h.

4.5 Results and Discussion

4.5.1 Infiltration under constant precipitation

For the constant irrigation rate of 1,200 ml d⁻¹, the steady-state amount of water drained by the side tension disc was 935 ml d⁻¹, whereas 278 ml d⁻¹ were discharged by the bottom tension disc resulting in a balanced water budget (the difference between in- and outflow was only 13 ml; Tab. 4.3).

Table 4.3: Comparison of measured and simulated outflow (HYDRUS 2D) from the monolith during steady-state infiltration

Source	Inflow	Outflow (side)		Outflow (bottom)		Difference error
	[ml d⁻¹]		[%]	[ml d⁻¹]	[%]	[ml d⁻¹]
Data	1,200	935	77.9	278	23.2	13
Model	1,200	872	72.7	327.6	27.3	0

The contour plot of the hydraulic potential shows a relatively homogeneous downward infiltration of the water indicated by the little blue arrows in the gradient plot (Fig. 4.4b). This is similar to the observations of Sinai and Dirksen (2006), who found that under constant precipitation (infiltration), the flow is directed vertically downward, however, for a

homogeneous sand soil. Only at the left side where the side tension disc is located, lateral movement of water is observed. This shows that the installation of a lateral tension disc and the application of a pressure head in a modified setup according to Sakaki et al. (2011) induced a suction that was sufficient to drain and quantify water moving laterally due to the applied lateral pressure gradients. Also, in the upper right part of the monolith, a lateral flow direction is observed, possibly caused by stones that were found after cutting the monolith. The magnitude of the gradient in hydraulic potential decreases from top to bottom and increases towards the side suction disc.

Unlike in the experiments of Miyazaki (1988), no clear deviation of flow along the horizon boundary is observed, which was evident from the hydraulic potential and SWC profiles. Miyazaki (1988) found an increase in water content and suction just along the boundary of a sandy loam layer over a gravel–plant layer that led to a lateral subsurface downhill flow on top of the coarser layer. In our experiment, the horizontal conductivity of the upper layer was three times higher than in the lower layer (Tab. 4.1). Also, secondary cracks during sensor installation (Fig. 4.1) might have led to allow for vertical flow in the monolith. These cracks could only be observed due to the use of a transparent encasement of the monolith facilitating the monitoring of the occurrence of such cracks during or after sensor installation instead of a wooden box (Germer & Braun, 2015). The transparent encasement was useful also for the identification of the horizon boundary and the resulting placement of the sensors (Fig. 4.1). Thus, the vertical hydraulic conductivity K_s might have been larger than 2.7 cm d^{-1} due to these cracks or heterogeneity during sampling and measurement of K_s, preventing the lower layer from being saturated and leading to lateral flow on top of it.

The pressure head of the side tension disc was set to −20 cm. This pressure head was experimentally derived as to where to first lateral flow would occur. It is assumed that this rather low pressure head was needed, because the contact between the soil and the side tension disc was poor. The side tension disc is filled with a flexible PVC mesh that will be dented towards the Plexiglas-encasing of the plate, if low pressure heads are applied. Thus, a high resistance must be overcome before the water can enter the plate. In the future, this might be avoided by using a less flexible filling material for the plate, like sinter glass plates that will not be dented by low pressure heads. Also, the size of the side suction plate is rather large in comparison with the size of the monolith. Thus, the pressure field within the box might be disturbed. To counteract this effect, the size of the monolith could be increased or the size of the side suction plate could be reduced. Because the size of the monolith is defined by the steel frame, it is handier to reduce the size of the side suction plate. This would also help to minimize the vertical gradient within the plate.

4.5.2 Comparison of steady-state infiltration to model

Simulated and measured outflow at the bottom and at the side have the same ratio of ~75% of the outflow leaving the monolith via the side suction plate and 25 % of the outflow being discharged via the bottom suction plate (Tab. 4.3). The higher discharge at the side suction disc indicates a strong lateral component of the flow along the horizon boundary. This is also observed in the direction of the velocity vectors (model, Fig. 4.5a) and gradients (measurement, Fig. 4.4b). Infiltration is mainly directed vertical in the upper and lower part of the monolith, whereas along the horizon boundary close to the side suction disc, water is flowing laterally. Below the horizon boundary, vertical flow is observed, similar to the hillslope study of Dušek and Vogel (2014).

A decrease in pressure heads towards the side suction disc is observed in the model (Fig. 4.5b). The highest observed pressure heads are found in the upper left part that decrease towards the side suction disc (Fig. 4.4a), similar to the model. Modeled and observed pressure heads (colored dots at the sensor positions in Fig. 4.5b) are almost similar. Only the right sensor in the middle row of the tensiometers differs strongly from the simulated value, possibly due to a crack.
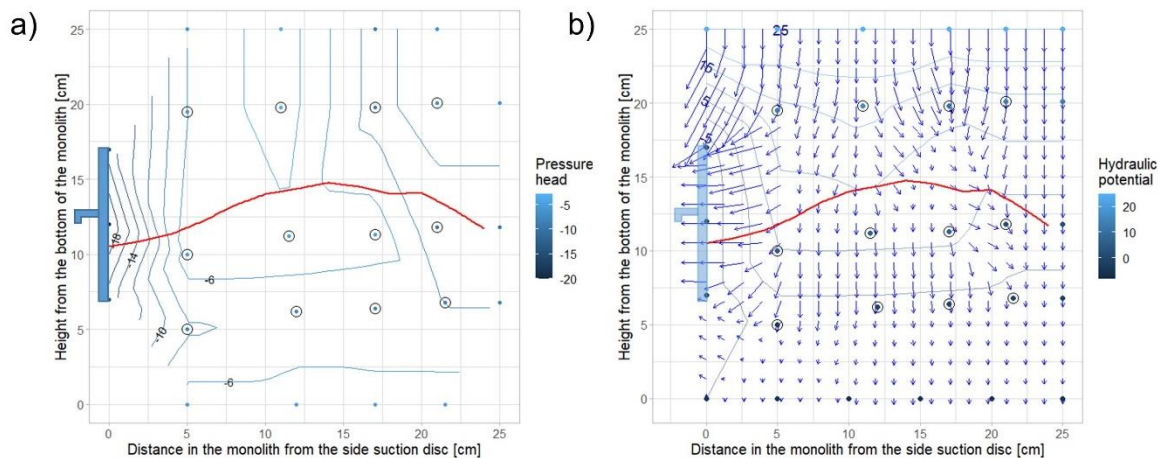
Figure 4.4: Contour plots of the (a) pressure head (cm) and (b) hydraulic potential (cm) with correspondent gradients under constant rain (1,200 ml d⁻¹). The length of the arrow in Plot b indicates the magnitude of the gradient. The red line indicates the horizon boundary, and the blue structure on the left indicates the position of the side tension disc.

For the water content, a clear distinction between the upper and the lower layer is observed, with higher water contents of around 25% (v/v) in the CBkg horizon as compared with the lower layer, with water contents around 19% (v/v) (Fig. 4.5 c). In the measurements, no such boundary is found. Still, the water content is higher in the upper layer as compared with the lower layer, with values reaching 40% (v/v) in the upper left corner (colored dots in Fig. 4.5c).
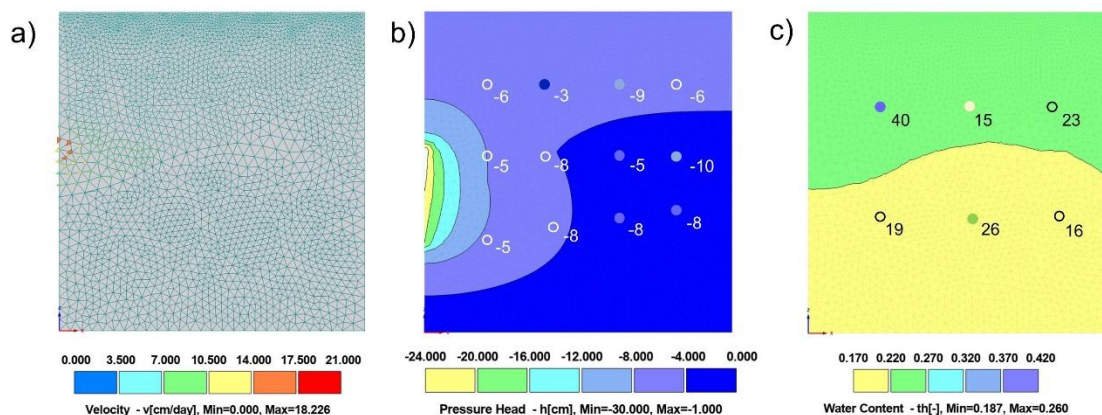
Figure 4.5: Modeling results using HYDRUS 2D showing (a) flow direction, (b) pressure head (cm), and (c) soil water content; circles within Plots b and c indicate the measured values (same color range as modeled values), and white circles indicate no difference between modeled and measured values. Figures show the steady state conditions 96 h after simulation start under constant rain (1,200 ml d⁻¹).

The idea of the model setup was to show that the observed water flow within the monolith under steady-state conditions can be explained by established models like the Richards equation and the van Genuchten–Mualem model. The model matched the observed outflow at the side and bottom suction discs reasonably well. The local pressure heads and the water contents in the two soil horizons were also reproduced by the model. These modeling results successfully validated the experimental setup for the quantification of LSF under steady-state conditions.

4.5.3   Reproducing preferential flow: Infiltration into macropores

To induce local saturation conditions, two artificial macropores were supplied with 7 ml of Brilliant Blue and 48 ml of water (total fluid application = 110 ml) within 30 h. Within the time of the tracer and the water application, 93 ml was drained via the side tension disc. The discrepancy between input and output might be attributed to evaporation during the fluid application.

The contour plots clearly show the position of the two macropores by an elevated hydraulic potential (Fig. 4.6b). The water infiltrates laterally around the holes into the matrix (blue strings in the middle top of the monolith in Fig. 4.6), similar to what was observed by Buttle and McDonald (2002) and Noguchi et al. (1999) and proposed by Lin et al. (2006) in a sloped forest soil. Also, below the holes, a sideward movement of water is observed towards the edge of the monolith, especially next to the right hole (Fig. 4.6b). Below the horizon boundary, the water flows vertically downwards to bottom tension disc. The lateral movement towards the side tension disc is much stronger than towards the bottom tension disc, as indicated by the larger magnitude of the gradient towards the left (longer arrows

in Fig. 4.6b). This is in accordance with the observation that all water leached from the monolith via the side tension disc throughout the tracer experiment. Due to the installation of the small tensiometers according to Sakaki et al. (2011), a fine resolution in the visualization of the gradients in the hydraulic potential was achieved, especially in the areas around the macropores. Placing a tensiometer closer to the side tension disc would probably give further insights about the flow passages of such small amounts of water added to the macropores.
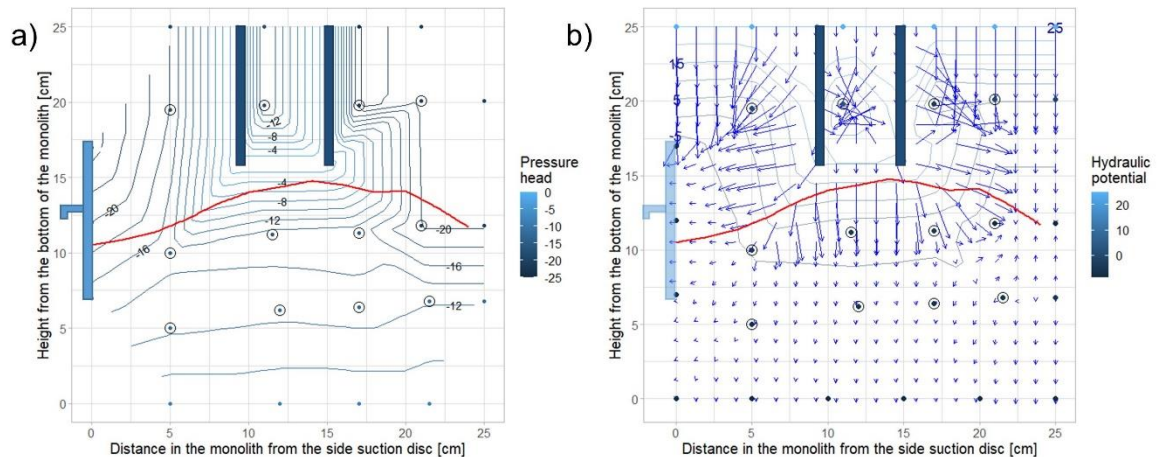
Figure 4.6: Contour plots of the (a) pressure head (cm) and (b) hydraulic potential (cm) with correspondent gradients when only the macropores are infiltrated. The length of the arrow in Plot b indicates the magnitude of the gradient. The red line indicates the horizon boundary, the blue structure on the left indicates the position of the side tension disc, and the blue strings in the middle top of the monolith show the position of the macropores.

4.5.4 Verification of flow direction with tracer experiment

To verify the flow behavior observed by the tensiometers and FDR sensors, 7 ml of the tracer Brilliant Blue were inserted into each hole followed by 48 ml of deionized water to spread the tracer. The dye was laterally distributed around the holes (3D visualization of dye spread in Fig. 4.7), as already observed in the contour plots (Fig. 4.6). At the top of the monolith, the dye was spread widely due to ponding during the water application. At the left hole, the dye was concentrated around the upper part of the hole. In contrast, the right hole showed a lateral spread of the tracer at the lower end of the hole that was also observed in the contour plots (Fig. 4.6b). Despite infiltrating vertically the Brilliant Blue was also distributed laterally around the right macropore indicating the LSF occurrence. The dye was also spread at the bottom of the right macropore further to the left in the direction of the side tension disc. This can be attributed to LSF of water along the horizon boundary as observed by Redding and Devito (2010) and Buttle and McDonald (2002) for the soil–bedrock interface. This supports the conceptual model, proposed by Lin et al. (2006), of

LSF also occurring along soil horizon boundaries as found by Noguchi et al. (1999) in a forest soil and by Hardie et al. (2012) in texture-contrast soils in Australia.
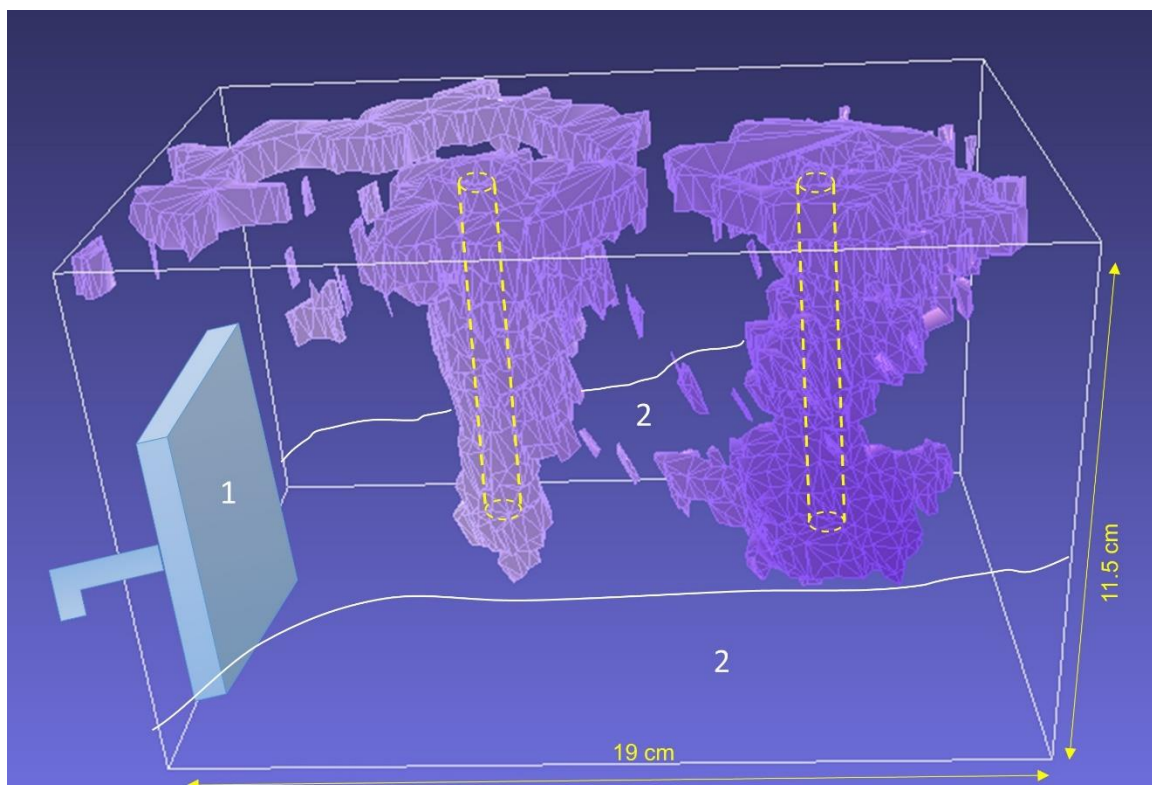
Figure 4.7: Three-dimensional representation of the dye stained areas after the Brilliant Blue tracer was applied. The holes representing macropores where the tracer was applied are marked in yellow. The side tension disc (1) is located at left side of the cuboid. The horizon boundary (2) is marked by two white lines.

The SWC was overestimated by the left and the middle sensor, whereas the sensor on the right underestimated the water content (Tab. 4.4) compared with the gravimetric water content. The middle sensor showed the highest SWC in both cases, whereas the left sensor had higher SWC than the right sensor in case of the FDR measurement and vice versa in the gravimetrical SWC measurement. Thus, despite the calibration of the sensors, deviations of 2–6% (v/v) were still found between the two measurement procedures. As for the gravimetric method, possible sources for errors are the time gap between FDR sensor removal and sampling and the small volume of the sample. Samples from the layer were taken ~24 h after the FDR sensors were removed and infiltration was stopped. The volume of the samples was only 10 cm³, such that small measurement errors could have already affected the value of the volumetric SWC. Also the EC5 sensor readings were sensitive to temperature and electrical conductivity of the soil water (Rosenbaum et al., 2011), not accounted for during the calibration procedure.

Table 4.4: Comparison of the soil water content measured by the frequency domain reflectometry sensors (SWC$_{FDR}$) in the upper part of the monolith and the mean and SD of the soil water content determined gravimetrically (FDR$_{grav}$) during the cutting of the monolith in the depths from 3 to 7 cm.

Sensor location	SWC$_{FDR}$	SWC$_{grav}$	SD (SWC$_{grav}$)
		[% (v/v)]	
Left	28.8	26.6	3.4
Middle	31.3	27.6	1.7
Right	23.1	27.0	0

4.5.5 Interrelation between experiments and nonequilibrium conditions

The experimental setup as presented above was capable of draining LSF from the monolith as well as vertical flow. Lateral subsurface flow occurred under constant rainfall and macropore infiltration. It was assumed that equilibrium conditions were present in the monolith under constant rainfall. The water retention curves of the CBkg and Bgk1 horizons under equilibrium conditions according to the laboratory measurements of Rieckh et al. (2012) and the model results of this study are presented in Fig. 4.8. The water retention curves measured in the monolith during a wetting process vary according to the sensor position within the monolith, indicating a heterogeneous soil structure of the soil monolith. The curves were extracted at the FDR sensor positions by interpolation of the measured pressure heads of the tensiometers surrounding each FDR sensor (for time series of sensors, see Appendix A4.2 and A4.3). In particular, the measured water retention curves of the CBkg horizon differ in their inclination as compared with the equilibrium curves. This might indicate the presence of nonequilibrium conditions within the monolith, because the steeper curves show that the water content lags behind the pressure head increase during irrigation (Hannes et al., 2016). For the water retention curve and timeseries of pressure head and water content under drying of the monolith, see Appendix A4.4–A4.6. These findings show the ability of the measurement setup to capture nonequilibrium conditions and thus provide data for model improvement and verification of nonequilibrium models.
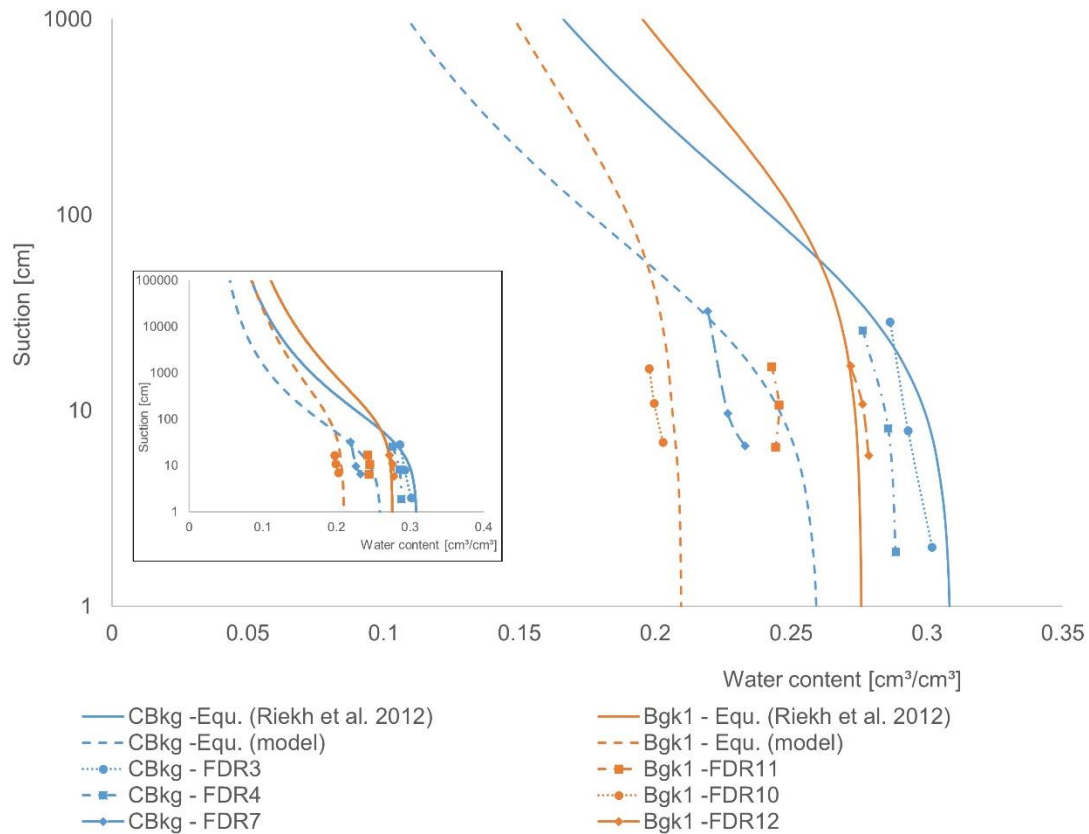
Figure 4.8: Modeled curves of the CBkg (blue) and the Bgk1 (orange) horizons from this paper (brokenlines) and from Rieckh et al. (2012) (solid lines), and the measured values from the monolith experiment under irrigation (short curves). Equ., equilbrium; FDR, frequency domain reflectometry.

4.5.6 Experimental setup to enhance the understanding of the mechanisms of LSF

According to Hardie et al. (2012), the mechanisms of LSF occurrence along texture-contrast soils are still poorly understood. So far structural variability (McNamara et al., 2005; Wöhling et al., 2012), vertical preferential flow through macropores (Guertault & Fox, 2020; Schwärzel et al., 2012), hydraulic gradients in highly permeable layers beneath kettleholes (H. H. Gerke et al., 2010), and connected flow paths within hillslopes (Guo et al., 2014; Laine-Kaulio et al., 2014; Wienhöfer & Zehe, 2014) have been reported as possible triggers for the onset of LSF. In particular, the widespread phenomenon of vertical preferential flow (K. M. Gerke et al., 2015; Liu & Lin, 2015; Newman et al., 2004) is an important mechanism for the onset of LSF even before the soil is water saturated (Guo et al., 2018), and that needs more detailed investigation. A better understanding of the processes leading to the onset of LSF due to vertical preferential flow will improve the prediction and modeling of agrochemical leaching from agricultural areas into the groundwater (Janssen et al., 2010) and adjacent streams (Kahl et al., 2008).

The presented experimental setup provides the means to further explore the onset of LSF along texture-contrast soil horizon boundaries. The transparent encasing allows for the

visual inspection of heterogeneities that might be responsible for LSF (McNamara et al., 2005; Wöhling et al., 2012). Additionally, by installing artificial macropores or capturing natural macropores, the effects of local saturation and hydraulic nonequilibrium on the onset of LSF can be investigated.

4.6 Conclusions

With the experimental setup for the detection of LSF, it was possible to visualize and quantify the water movement within an undisturbed soil monolith sampled from a Haplic Regosol (calcaric). We could distinguish between lateral flow along horizon boundaries and vertical flow. With sensors for measuring the water contents and pressure heads in regular spatial intervals within the monolith, it was possible to capture water flow under local nonequilibrium conditions that could occur at impeding soil horizons (e.g., during macropore infiltration). Thus the measurement setup could be useful to provide data for the verification of modeling results.

Under constant rainfall, an equilibrium model could reproduce the flow diversion within the monolith, with the amount of outflow at the bottom and at the side of the sample proving the successful operation of the experimental setup. In comparison with the model predictions, the measured water content and pressure heads varied greatly and indicated the presence of heterogeneities within the monolith that were not implemented in the model.

The observed LSF that was experimentally induced by local pressure head nonequilibrium during preferential flow through artificial macropores proved that the experimental setup was able to capture assumed flow phenomena. The data provided could be used to explore water dynamics under transient conditions for the development of improved model concepts including nonequilibrium phenomena that allow to predict the onset of LSF in macroscopically unsaturated soil.

4.7 Acknowledgments

4.8   References

Akima, Hiroshi (1978): A method of bivariate interpolation and smooth surface fitting for irregularly distributed data points. In: ACM Transactions on Mathematical Software (TOMS) 4 (2), S. 148–159.

Allaire, Suzanne E.; Roulier, Stéphanie; Cessna, Allan J. (2009): Quantifying preferential flow in soils: A review of different techniques. In: Journal of Hydrology 378 (1-2), S. 179–204. DOI: 10.1016/j.jhydrol.2009.08.013.

Buttle, J. M.; McDonald, D. J. (2002): Coupled vertical and lateral preferential flow on a forested slope. In: Water Resour. Res. 38 (5), 18-1-18-16. DOI: 10.1029/2001WR000773.

Castiglione, Paolo; Mohanty, B. P.; Shouse, P. J.; Simunek, J.; van Genuchten, M. Th; Santini, A. (2003): Lateral water diffusion in an artificial macroporous system: Modeling and experimental evidence. In: Vadose Zone Journal 2 (2), S. 212–221.

Cook, F. J. (2006): Unsaturated hydraulic conductivity: Laboratory tension infiltrometer. In: Soil Sampling and Methods of Analysis.

Di Prima, Simone; Winiarski, Thierry; Angulo-Jaramillo, Rafael; Stewart, Ryan D.; Castellini, Mirko; Abou Najm, Majdi R. et al. (2020): Detecting infiltrated water and preferential flow pathways through time-lapse ground-penetrating radar surveys. In: The Science of the total environment 726, S. 138511. DOI: 10.1016/j.scitotenv.2020.138511.

Dušek, Jaromir; Vogel, Tomas (2014): Modeling Subsurface Hillslope Runoff Dominated by Preferential Flow: One- vs. Two-Dimensional Approximation. In: Vadose Zone Journal 13 (6), vzj2013.05.0082. DOI: 10.2136/vzj2013.05.0082.

Dušek, Jaromir; Vogel, Tomas; Dohnal, Michal; Gerke, Horst H. (2012): Combining dual-continuum approach with diffusion wave model to include a preferential flow component in hillslope scale modeling of shallow subsurface runoff. In: Advances in water resources 44, S. 113–125. DOI: 10.1016/j.advwatres.2012.05.006.

Ehrhardt, Annelie; Groh, Jannis; Gerke, Horst H. (2021): Wavelet analysis of soil water state variables for identification of lateral subsurface flow: Lysimeter vs. field data. In: Vadose zone j. 20 (3), S. 149. DOI: 10.1002/vzj2.20129.

FastStone Photo Resizer (Version 4.3) (2019). Retrieved from https://www.faststone.org

Filipović, Vilim; Gerke, Horst H.; Filipović, Lana; Sommer, Michael (2018): Quantifying Subsurface Lateral Flow along Sloping Horizon Boundaries in Soil Profiles of a Hummocky Ground Moraine. In: Vadose Zone Journal 17 (1), S. 170106. DOI: 10.2136/vzj2017.05.0106.

Fox, Garey A.; Muñoz-Carpena, Rafael; Purvis, Rebecca A. (2018): Controlled laboratory experiments and modeling of vegetative filter strips with shallow water tables. In: Journal of Hydrology 556 (3), S. 1–9. DOI: 10.1016/j.jhydrol.2017.10.069.

Gerke, Horst H. (2006): Preferential flow descriptions for structured soils. In: J. Plant Nutr. Soil Sci. 169 (3), S. 382–400. DOI: 10.1002/jpln.200521955.

Gerke, Horst H.; Koszinski, Sylvia; Kalettka, Thomas; Sommer, Michael (2010): Structures and hydrologic function of soil landscapes with kettle holes using an integrated hydropedological approach. In: Journal of Hydrology 393 (1-2), S. 123–132. DOI: 10.1016/j.jhydrol.2009.12.047.

Gerke, Kirill M.; Sidle, Roy C.; Mallants, Dirk (2015): Preferential flow mechanisms identified from staining experiments in forested hillslopes. In: Hydrol. Process. 29 (21), S. 4562–4578. DOI: 10.1002/hyp.10468.

Germer, Kai; Braun, Jürgen (2015): Determination of Anisotropic Saturated Hydraulic Conductivity of a Macroporous Slope Soil. In: Soil Science Society of America Journal 79 (6), S. 1528–1536. DOI: 10.2136/sssaj2015.02.0071.

Guertault, Lucie; Fox, Garey. A. (2020): Performance of preferential flow models in predicting infiltration through a remolded soil with artificial macropores. In: Vadose zone j. 19 (1). DOI: 10.1002/vzj2.20055.

Guo, L.; Fan, B.; Zhang, J.; Lin, H. (2018): Occurrence of subsurface lateral flow in the Shale Hills Catchment indicated by a soil water mass balance method. In: Eur J Soil Sci 69 (5), S. 771–786. DOI: 10.1111/ejss.12701.

Guo, Li; Chen, Jin; Lin, Henry (2014): Subsurface lateral preferential flow network revealed by time-lapse ground-penetrating radar in a hillslope. In: Water Resour. Res. 50 (12), S. 9127–9147. DOI: 10.1002/2013WR014603.

Guo, Li; Lin, Henry (2018): Addressing Two Bottlenecks to Advance the Understanding of Preferential Flow in Soils. In: Advances in Agronomy, Bd. 147: Elsevier (Advances in Agronomy, 147), S. 61–117.

Guo, Li; Lin, Henry; Fan, Bihang; Nyquist, Jonathan; Toran, Laura; Mount, Gregory J. (2019): Preferential flow through shallow fractured bedrock and a 3D fill-and-spill model of hillslope subsurface hydrology. In: Journal of Hydrology 576 (1–2), S. 430–442. DOI: 10.1016/j.jhydrol.2019.06.070.

Hannes, M.; Wollschläger, U.; Wöhling, T.; Vogel, H.-J. (2016): Revisiting hydraulic hysteresis based on long-term monitoring of hydraulic states in lysimeters. In: Water Resour. Res. 52 (5), S. 3847–3865. DOI: 10.1002/2015WR018319.

Hardie, Marcus; Lisson, Shaun; Doyle, Richard; Cotching, William (2012): Determining the frequency, depth and velocity of preferential flow by high frequency soil moisture monitoring. In: Journal of contaminant hydrology 144 (1), S. 66–77.

Hillel, Daniel (1987): Unstable flow in layered soils: A review. In: Hydrol. Process. 1 (2), S. 143–147. DOI: 10.1002/hyp.3360010203.

Ippisch, O.; Vogel, H-J; Bastian, P. (2006): Validity limits for the van Genuchten–Mualem model and implications for parameter estimation and numerical simulation. In: Advances in water resources 29 (12), S. 1780–1789.

IUSS, (2006). World reference base for soil resources 2006: World Soil Resources Reports No. 103. FAO, Rome

Janssen, Manon; Lennartz, Bernd; Wohling, Thomas (2010): Percolation losses in paddy fields with a dynamic soil structure: model development and applications (24) (7).

Jarvis, N. J. (2007): A review of non-equilibrium water flow and solute transport in soil macropores: Principles, controlling factors and consequences for water quality. In: European Journal of Soil Science 58 (3), S. 523–546.

Julich, Dorit; Julich, Stefan; Feger, Karl-Heinz (2017): Phosphorus fractions in preferential flow pathways and soil matrix in hillslope soils in the Thuringian Forest (Central Germany). In: J. Plant Nutr. Soil Sci. 180 (3), S. 407–417. DOI: 10.1002/jpln.201600305.

Kahl, G.; Ingwersen, J.; Nutniyom, P.; Totrakool, S.; Pansombat, K.; Thavornyutikarn, P.; Streck, T. (2008): Loss of pesticides from a litchi orchard to an adjacent stream in northern Thailand. In: European Journal of Soil Science 59 (1), S. 71–81.

Köhne, J. Maximilian; Mohanty, Binayak P. (2005): Water flow processes in a soil column with a cylindrical macropore: Experiment and hierarchical modeling. In: Water Resour. Res. 41 (3), S. 1234. DOI: 10.1029/2004WR003303.

Laine-Kaulio, Hanne; Backnäs, Soile; Karvonen, Tuomo; Koivusalo, Harri; McDonnell, Jeffrey J. (2014): Lateral subsurface stormflow and solute transport in a forested hillslope: A combined measurement and modeling approach. In: Water Resour. Res. 50 (10), S. 8159–8178. DOI: 10.1002/2014WR015381.

Leslie, I. N.; Heinse, R. (2013): Characterizing Soil-Pipe Networks with Pseudo-Three-Dimensional Resistivity Tomography on Forested Hillslopes with Restrictive Horizons. In: Vadose Zone Journal 12 (4), vzj2012.0200. DOI: 10.2136/vzj2012.0200.

Lin, H. S.; Kogelmann, W.; Walker, C.; Bruns, M. A. (2006): Soil moisture patterns in a forested catchment: A hydropedological perspective. In: Geoderma 131 (3-4), S. 345–368. DOI: 10.1016/j.geoderma.2005.03.013.

Liu, Hu; Lin, Henry (2015): Frequency and Control of Subsurface Preferential Flow: From Pedon to Catchment Scales. In: Soil Science Society of America Journal 79 (2), S. 362–377. DOI: 10.2136/sssaj2014.08.0330.

Lv, Meixia; Hao, Zhenchun; Liu, Zhen; Yu, Zhongbo (2013): Conditions for lateral downslope unsaturated flow and effects of slope angle on soil moisture movement. In: Journal of Hydrology 486 (1), S. 321–333. DOI: 10.1016/j.jhydrol.2013.02.013.

McNamara, James P.; Chandler, David; Seyfried, Mark; Achet, Shiva (2005): Soil moisture states, lateral flow, and streamflow generation in a semi-arid, snowmelt-driven catchment. In: Hydrol. Process. 19 (20), S. 4023–4038.

Miyazaki, Tsuyoshi (1988): Water flow in unsaturated soil in layered slopes. In: Journal of Hydrology 102 (1-4), S. 201–214.

Newman, Brent D.; Wilcox, Bradford P.; Graham, Robert C. (2004): Snowmelt-driven macropore flow and soil saturation in a semiarid forest. In: Hydrol. Process. 18 (5), S. 1035–1042. DOI: 10.1002/hyp.5521.

Noguchi, S.; Tsuboyama, Y.; Sidle, R. C.; Hosoda, I. (1999): Morphological Characteristics of Macropores and the Distribution of Preferential Flow Pathways in a Forested Slope Segment. In: Soil Science Society of America Journal (63), S. 1413–1423.

Nyquist, Jonathan E.; Toran, Laura; Pitman, Lacey; Guo, Li; Lin, Henry (2018): Testing the Fill-and-Spill Model of Subsurface Lateral Flow Using Ground-Penetrating Radar and Dye Tracing. In: Vadose zone j. 17 (1), S. 1–13. DOI: 10.2136/vzj2017.07.0142.

Potter, Thomas L.; Bosch, David D.; Strickland, Timothy C. (2015): Tillage impact on herbicide loss by surface runoff and lateral subsurface flow. In: The Science of the total environment 530-531, S. 357–366. DOI: 10.1016/j.scitotenv.2015.05.079.

R: A Language and Environment for Statistical Computing (Version R-3.6.2) (2019). Vienna, Austria. Retrieved from https://www.R-project.org

Redding, Todd; Devito, Kevin (2010): Mechanisms and pathways of lateral flow on aspen-forested, Luvisolic soils, Western Boreal Plains, Alberta, Canada. In: Hydrol. Process. 24 (21), S. 2995–3010. DOI: 10.1002/hyp.7710.

Rieckh, Helene; Gerke, Horst H.; Sommer, Michael (2012): Hydraulic properties of characteristic horizons depending on relief position and structure in a hummocky glacial soil landscape. In: Soil and Tillage Research 125, S. 123–131. DOI: 10.1016/j.still.2012.07.004.

Rosenbaum, U.; Huisman, J. A.; Vrba, J.; Vereecken, H.; Bogena, H. R. (2011): Correction of Temperature and Electrical Conductivity Effects on Dielectric Permittivity Measurements with ECH 2 O Sensors. In: Vadose Zone Journal 10 (2), S. 582–593. DOI: 10.2136/vzj2010.0083.

Šimůnek, J., M.Th. van Genuchten, and M. Šejna. (2016). Recent Developments and Applications of the HYDRUS Computer Software Packages. Vadose Zone J. 15(7). doi:10.2136/vzj2016.04.0033

Sakaki, Toshihiro; Limsuwat, Anuchit; Cihan, Abdullah; Frippiat, Christophe C.; Illangasekare, Tissa H. (2011): Water Retention in a Coarse Soil Pocket under Wetting and Drainage Cycles. In: Vadose Zone Journal 11 (1), S. 223. DOI: 10.2136/vzj2011.0028.

Schindelin, Johannes; Arganda-Carreras, Ignacio; Frise, Erwin; Kaynig, Verena; Longair, Mark; Pietzsch, Tobias et al. (2012): Fiji: an open-source platform for biological-image analysis. In: Nature methods 9 (7), S. 676–682.

Schwärzel, Kai; Ebermann, Sebastian; Schalling, Nico (2012): Evidence of double-funneling effect of beech trees by visualization of flow pathways using dye tracer. In: Journal of Hydrology 470-471 (6), S. 184–192. DOI: 10.1016/j.jhydrol.2012.08.048.

Schaap, Marcel G.; Leij, Feike J.; van Genuchten, Martinus Th (2001): Rosetta: A computer program for estimating soil hydraulic parameters with hierarchical pedotransfer functions. In: Journal of Hydrology 251 (3-4), S. 163–176.

Sidle, Roy C.; Noguchi, Shoji; Tsuboyama, Yoshio; Laursen, Karin (2001): A conceptual model of preferential flow systems in forested hillslopes: evidence of self-organization. In: Hydrol. Process. 15 (10), S. 1675–1692. DOI: 10.1002/hyp.233.

Sinai, G.; Dirksen, C. (2006): Experimental evidence of lateral flow in unsaturated homogeneous isotropic sloping soil due to rainfall. In: Water Resour. Res. 42 (12), S. 964. DOI: 10.1029/2005WR004617.

Sobotkova, Martina; Snehota, Michal (2014): Method of In-Line Bromide Breakthrough Curve Measurements for Column Leaching Experiments. In: Vadose Zone Journal 13 (8), vzj2013.11.0192. DOI: 10.2136/vzj2013.11.0192.

Sommer, M.; Augustin, J.; Kleber, M. (2016): Feedbacks of soil erosion on SOC patterns and carbon dynamics in agricultural landscapes—The CarboZALF experiment. In: Soil and Tillage Research 156 (Issue 6235), S. 182–184. DOI: 10.1016/j.still.2015.09.015.

Vogel, T.; van Genuchten, M. Th; Cislerova, M. (2001): Effect of the shape of the soil hydraulic functions near saturation on variably-saturated flow predictions. In: Advances in water resources 24 (2), S. 133–144.

Wienhöfer, J.; Zehe, E. (2014): Predicting subsurface stormflow response of a forested hillslope – the role of connected flow paths. In: Hydrol. Earth Syst. Sci. 18 (1), S. 121–138. DOI: 10.5194/hess-18-121-2014.

Wöhling, Thomas; Bidwell, Vincent J.; Barkle, Gregory F. (2012): Dual-tracer, non-equilibrium mixing cell modelling and uncertainty analysis for unsaturated bromide and chloride transport. In: Journal of contaminant hydrology 140-141, S. 150–163. DOI: 10.1016/j.jconhyd.2012.08.001.

5 Synthesis and Conclusions

The aim of this thesis was to improve the understanding of mechanisms causing LSF and factors influencing the onset of LSF in agricultural landscapes. This will help to develop a conceptual model for LSF occurrence providing the basis for numerical modeling of water flow along agricultural hillslopes and determining the susceptibility of these landscapes to LSF.

5.1 First conceptual findings on lateral subsurface flow occurrence in agricultural hillslopes

5.1.1 Possible influences of soil surface structure on subsurface flow development

The soil surface structure and its evolvement over time is not only an important parameter for soil erosion modeling in order to derive soil losses and possible water pollution (Eltner et al., 2015; Meinen and Robinson, 2020). It may also provide information about the local onset of LSF. By analyzing the soil structure, the soil's tendency towards ponding during precipitation can be derived: for example, dells in the soil surface lead to local accumulation of water and thus to local saturation of the upper soil horizons that might initiate LSF along impeding layers in the subsurface (Newman et al., 2004).

The first objective was to enable finding this relationship between soil surface structure and LSF. This was achieved by firstly demonstrating the applicability of the SfM photogrammetry for detecting small-scale soil surface structural changes along a soil erosion measurement slope with widely available camera equipment and freely available software. Secondly, the technique was improved by attributing the different soil structural changes at different parts of the hillslope to the processes of soil erosion and soil settlement via measurement and modeling of bulk density changes (Fig. 5.1). Thus, the dominating processes for each plot and slope part could be identified.

However, it was shown that these observations in fine resolution are only possible at smaller plots and not for complete slopes. In order to relate soil loss measurements from smaller plots to larger plots the problem of upscaling needs to be solved. The quality of the 3D-soil surface models generated by SfM could be improved by processing images with a higher resolution which is not possible at the moment due to computational limits. Also, improvements of the accuracy and the calibration of the empirical bulk density model are still needed.
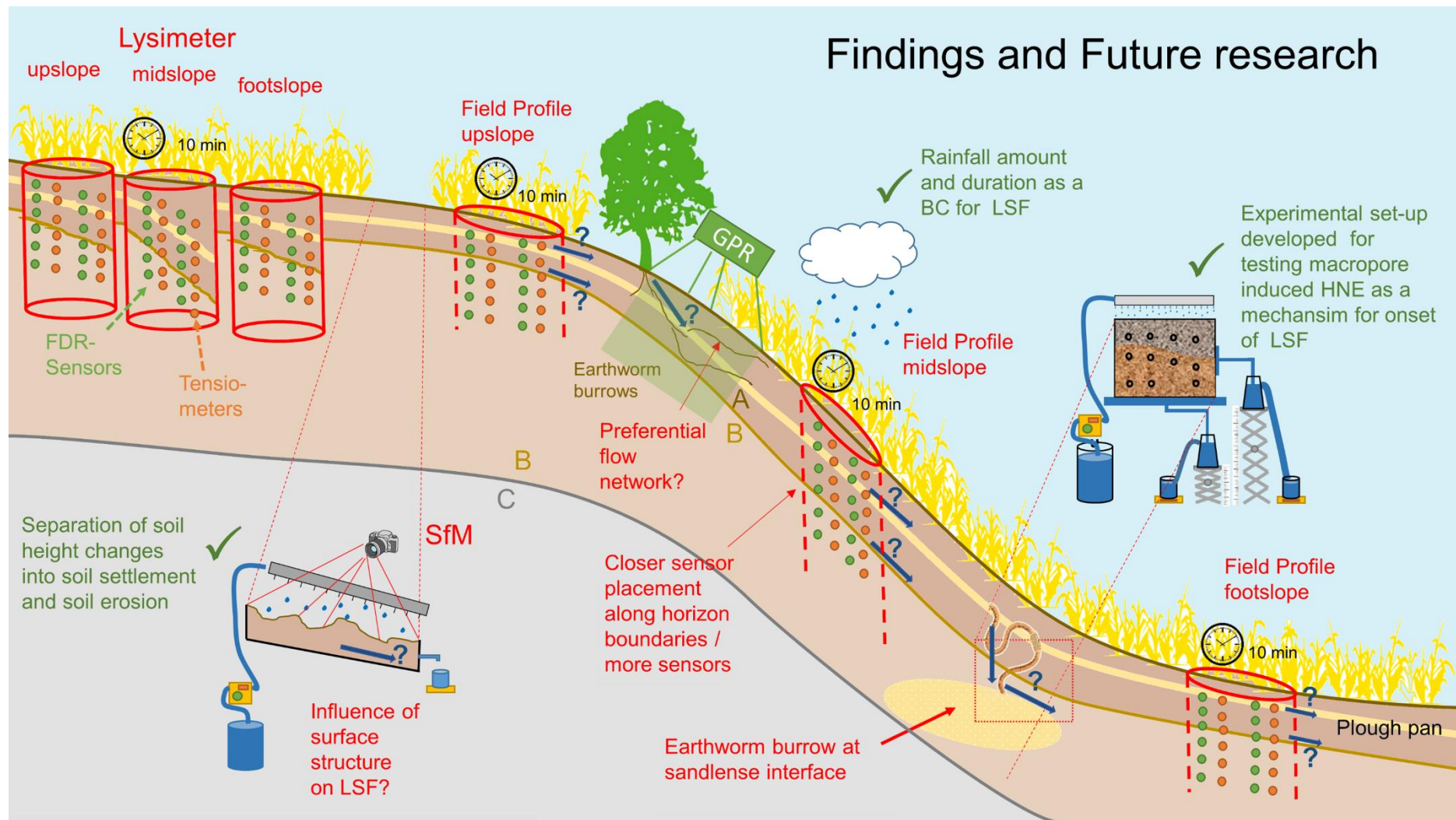
Figure 5.1: Complementary experiments to derive a concept for LSF occurrence in agricultural landscapes (BC … boundary condition)

To derive how soil structural changes and the observations of soil settlement and soil erosion are possibly related to LSF, the processes observed at the upper, middle and lower slope of the experimental site in Müncheberg could be compared to subsurface flow patterns at similar positions of other slopes. For instance, Laine-Kaulio et al. (2015) observed different flow patterns at different slope positions in the subsurface of forested hillslopes. Also, Groh et al. (2020) showed differing vertical fluxes in agricultural landscapes according to the slope position.

In the upper slope area of the plots observed in chapter 2 most of the soil height changes observed with SfM photogrammetry were attributed to soil settlement. One of the main causes for soil settlement is the vertical infiltration of water: when the soil pores are filled with water, menisci between the soil particles lead to a reduction in soil height (Hartge et al., 2014). This is supported by the findings of Laine-Kaulio et al. (2015), Lee and Kim (2019b) and Groh et al. (2020), who found vertical flow dominant in the upper areas of hillslopes as compared to middle slope positions.

For the footslope mainly deposition from upper slope parts was reported in chapter 2. Surface dells were filled by soil material and the roughness of the area declined. Deposition of soil particles is only found if surface water loaded with sediment is flowing downhill. Thus, overland flow must have occurred possibly indicating the saturation of upper soil layers (Holden, 2005). The saturation of the upper horizons might lead to the development of perched water tables initiating LSF in macropores in the Bt-horizon like it was found by Newman et al. (2004). Also, Lee and Kim (2019b) found more precipitation events that lead to LSF at footslope positions than at upper slope parts.

5.1.2 Boundary conditions for the onset of LSF in agricultural landscapes

The second objective was to deduce boundary conditions leading to the initiation of LSF in agricultural soils. The number of existing methods for detecting LSF with subsurface sensor networks was extended by the application of wavelet coherence analysis (WCA) on water content time series of a lysimeter and a corresponding field soil. The hypothesis was that time shifts in the correlation of water content data during and after precipitation events in a lysimeter and the corresponding field site will indicate LSF. Additional water travelling laterally along horizon boundaries might lead to a faster water content increase at the field site in comparison to the lysimeter, where the water is only allowed to travel vertically.

The analysis showed that WCA derived asynchronous correlation patterns between the water content time series of the lysimeter and the field plot during precipitation events are possibly related to LSF. Precipitation amount and duration are suggested as important boundary conditions for the occurrence of LSF in spring and autumn and VPF during summer (Fig. 5.1). VPF events were detected in the lysimeter during heavy precipitation events in summer. The occurrence of VPF under heavy precipitation was also reported by Liu and Lin (2015), Wiekenkamp et al. (2016) and Demand et al. (2019) for forested hillslopes. It confirms the theory of Hardie et al. (2012) that in agricultural soils macropore flow through shrinkage cracks might lead to bypass flow of horizon boundaries in summer. This impedes the development of perched water tables along the horizon interfaces that would initiate LSF.

LSF events, characterized by a faster soil water content increase in the field as compared to the lysimeter, were more likely to occur in spring and autumn during prolonged precipitation events with high precipitation amounts. This is in accordance with the results of Tang et al. (2010) and Lee and Kim (2021) who found that LSF occurred along an impeding layer after heavy precipitation events in agricultural soils and forested soils, respectively. The persistent infiltration might lead to a pressure head build-up and thus the creation of a perched water table along the horizon boundaries (McNamara et al., 2005).

The lengths and the number of time series analyzed here for the occurrence of LSF are too small to statistically derive precipitation amount and duration as controlling factors of LSF. This analysis can only give a first insight on boundary conditions for the onset of LSF in agricultural landscapes.

Despite LSF several other factors might have led to asynchronous water content increases in response to precipitation in the lysimeter and field soil: Sensors might be placed along different small-scale heterogeneities in the lysimeter and the field soil. Also, differences in plant development were observed between the two plots that might lead to differing infiltration patterns. Additionally, different initial water contents before the precipitation events were found in the lysimeter and the field influencing the proceeding of the infiltration front. Thus, it is necessary to critically assess the infiltration events with possible LSF occurrence that were deduced by WCA.

The application of WCA is limited to long uninterrupted time series of water content data. Gap filling procedures are needed to close data gaps larger than a few hours. For example, modeling or machine learning could help closing these data gaps (e.g., Liu et al., 2022).

5.1.3 Mechanisms of LSF occurrence in agricultural landscapes: Macropore induced HNE

The third objective was to enhance the understanding of mechanisms causing LSF in agricultural soils. An experimental set-up providing evidence of LSF in undisturbed soil monoliths under HNE conditions of macropore infiltration was designed. The hypothesis was that local pore water saturation, i.e., water potentials close to zero, is a critical trigger for the onset of lateral and preferential flow. A laboratory experiment was developed that allows for the direct observation of LSF induced by HNE conditions along horizon boundaries. Also, a new method for the excavation of rectangular soil monoliths was established for modeling the experiment in a 2D model set-up. LSF was observed under hydraulic equilibrium conditions and macropore induced HNE conditions. Thus, the hypothesis was confirmed for the first tested soil monolith sampled along a B-C-horizon boundary of a Haplic Regosol. First modeling results confirm the lateral and vertical water flow observed within the soil monolith by tensiometer measurements.

The presented method of measuring LSF along horizon boundaries with a high-resolution tension and water content monitoring might help closing the link between VPF and LSF (Allaire et al., 2009). It may provide experimental evidence for macropore induced LSF as modelled by Dušek et al. (2012). However, the method presented in chapter 4 has just been tested for one soil monolith. The application of this measurement set-up to a greater variety of soils and horizon boundaries is still needed.

One limitation of the experimental set-up is the strong hydraulic potential of the side suction plate that needs to be induced for the initiation of LSF as found in the first tested monolith sample. LSF was not observed without such a strong gradient and thus the experimental set-up might not represent conditions as they are found in field soils. Also, only experiments close to saturation have been conducted so far. At matric potentials smaller than -30 cm the air entry point of the bottom suction plate hinders further desiccation.

In the tested monolith it was hypothesized that LSF would be generated along a B-C-horizon boundary contrast with less conductive layer situated below a higher conductive horizon. However, macropore induced LSF along sand lenses due to funnel effects (Kung, 1990) might be more common in highly heterogeneous morainic soils than flow along impeding layers. Thus, to generate reliable results, more experiments need to be conducted with undisturbed soil monoliths excavated from texture contrast horizon boundaries in agricultural soils, especially along sand lenses (Kung, 1990; Fig. 5.1).

5.2   Outlook

The analysis of LSF occurrence in agricultural soils of hummocky ground moraines led to a first idea for a conceptual model. However, more questions need to be answered in order to derive a more elaborate understanding of processes influencing the occurrence of LSF in agricultural landscapes. For example, the direct link between soil surface structures and the onset of LSF is still unknown. Other boundary conditions like antecedent soil moisture need to be assessed as possible indicators for LSF initiation. Finally, more evidence is needed in order to resolve, if HNE induced macropore flow is a possible mechanism for LSF occurrence.

To analyze the direct impact of different surface structures and soil settlement or soil erosion on the onset of subsurface flow processes, it is necessary to combine observations of LSF and soil structural changes in laboratory and field experiments.

In the field SfM could be used in combination with the VAMOS experimental set-up. By analyzing soil surface structural changes of the VAMOS-lysimeter and –field plots throughout precipitation, the onset of LSF might be related to surface structural features. For example, the relation between soil surface roughness and the onset of LSF could be explored directly in the field.

To derive the direct impact of individual soil surface structures on LSF occurrence, laboratory experiments could be conducted. For instance, soil boxes similar to Ma et al. (2022) could be prepared containing an impeding layer below a loose soil layer instrumented with funneling devices to collect LSF and tensiometers to assess the local onset of LSF (Fig. 5.1). On the soil surface different structures like wheel tracks and seed rows could be created. Under controlled precipitation simulation experiments the timing and onset of LSF influenced by these surface structures can be assessed. SfM can be applied to quantify the change of these structures over time. It could be tested directly whether surface ponding indicates the local onset of LSF. Bulk density measurements or modeling is used to distinguish between soil erosion and soil settlement. Also, thermo-time domain reflectometry sensors can be applied to measure soil bulk density continuously and nondestructively (Lu et al., 2020).

To gain a more profound understanding of boundary conditions initiating LSF along agricultural hillslopes more soil profiles with differing horizon boundaries should be analyzed (Fig. 5.1). In chapter 3 only the profile of an Endogleyic Colluvic Regosol was examined to test the applicability of WCA to derive the temporal onset of LSF. Two other profiles, an eroded Haplic Luvisol and a Haplic Regosol with a similar experimental set-up could be used for further analysis at the CarboZALF-D experimental site (Fig. 5.1). Also, the fourth VAMOS set-up in Schäfertal (Lower Harz Mountains, central Germany) with

higher annual precipitation amounts could be analyzed to compare LSF occurrence under different climatic conditions. However, water content and water tension data time series are subject to severe data gaps that impede the application of WCA. This problem could be solved by employing other types of more continuous data, like temperature time series. Different soil temperature changes in lysimeter and field due to infiltration of warm or cold precipitation water might indicate LSF.

Since the application of WCA is limited to uninterrupted time series, other methods for time series analysis could be deployed, like the soil water mass balance method (SWMB) (Guo et al., 2018; Lee and Kim, 2019a). However, the applicability of the SWMB method has been only demonstrated for areas with an annual precipitation more than 1000 mm, whereas in the average annual precipitation at the CarboZALF-D field amounts to approximately 500 mm. This low amount of precipitation might lead to smaller precipitation induced increases in soil moisture and even no responses in soil moisture in greater soil depths. Also, principal component analysis (PCA) (e.g., Hohenbrink et al., 2016) could be used to derive a component that can be attributed to LSF. Thus, time series could be "denoised" by other influencing factors mentioned in chapter 3.

Ideally, the sensor placement in the lysimeter and the field profile could be optimized to analyze the occurrence of LSF in other horizons and the existence of a perched water table (Fig. 5.1). Tensiometers and FDR-sensors might be placed in smaller depth increments, for example, 10 cm, so a better spatial resolution is achieved, especially closer to the surface, for instance, just above the plough pan (Sander and Gerke, 2007; Tang et al., 2010). Also, LSF induced by a perched water table just above the horizon boundary might not be detected if the sensors are placed in the vertical center of a soil horizon. This can be avoided if the sensors are inserted closer to the horizon boundary like in the laboratory experiments (chapter 4).

Lysimeter and field profile data were logged in rather large time increments of 1 h. Thus, very fast preferential flow events (lateral or vertical) might be missed during heavy precipitation events. Logging the data in smaller time increments like 10 min could help to detect those fast changes as it has been demonstrated by Liu and Lin (2015).

Whether HNE induced LSF is a possible subsurface flow mechanism in agricultural landscapes can only be verified if more experiments on soil monoliths are conducted with the methodological approach presented in chapter 4. As already suggested, LSF due to the texture contrast along sand lenses needs to be further investigated (Fig. 5.1).

In forest soils LSF is often observed along a network of pipes parallel to the impeding layer that gets connected and activated when water infiltrates into the soil (e.g., Redding and Devito, 2010; Nyquist et al., 2018). However, during the excavation of the monolith and

throughout the experiments no such network of pipes along the B-C-horizon interface was observed. As indicated above, the existence of such a network needs to be checked, for example, by time-lapse ground penetrating radar (GPR) analysis according to Guo et al. (2014) or by conducting tracer experiments (Fig. 5.1). Dye tracing experiments and subsequent excavation of the soil similar to Laine-Kaulio et al. (2015) may display such a macropore network over shorter distances (1-3 m). Salt tracer experiments, for example, with KBr, in combination with electrical resistivity tomography (ERT) might reveal such a network over longer slope distances. For example, Scaini et al. (2017) were able to cover a slope length of up to 60 m with this technique. Similarly, Robinson et al. (2020) were able to analyze subsurface flow patterns over a slope length of 10 m to a depth of 5 m by salt tracer application in combination with electrical resistivity imaging (ERI).

LSF is a ubiquitous phenomenon that enhances pesticide and nutrient transport to surface and groundwater bodies, especially in agricultural landscapes. Further developing conceptual models and numerical models for the prediction of LSF will help to reduce risks to the environment and human life.

References for Introduction and Synthesis

Allaire, S.E., Roulier, S., Cessna, A.J., 2009. Quantifying preferential flow in soils: A review of different techniques. Journal of Hydrology 378, 179–204. https://doi.org/10.1016/j.jhydrol.2009.08.013.

Biswas, A., Si, B.C., 2011. Identifying scale specific controls of soil water storage in a hummocky landscape using wavelet coherency. Geoderma 165, 50–59. https://doi.org/10.1016/j.geoderma.2011.07.002.

Buttle, J.M., McDonald, D.J., 2002. Coupled vertical and lateral preferential flow on a forested slope. Water Resour. Res. 38. https://doi.org/10.1029/2001WR000773.

Christiansen, J.S., Thorsen, M., Clausen, T., Hansen, S., Refsgaard, J.C., 2004. Modelling of macropore flow and transport processes at catchment scale. Journal of Hydrology 299, 136–158. https://doi.org/10.1016/j.jhydrol.2004.04.029.

Claes, N., Paige, G.B., Parsekian, A.D., 2019. Uniform and lateral preferential flows under flood irrigation at field scale. Hydrological Processes 33, 2131–2147. https://doi.org/10.1002/hyp.13461.

Dai, Z., Ma, C., Miao, L., Li, M., Wu, J., Wang, X., 2022. Initiation conditions of shallow landslides in two man-made forests and back estimation of the possible rainfall threshold. Landslides 19, 1031–1044. https://doi.org/10.1007/s10346-021-01823-1.

Dasgupta, S., Mohanty, B.P., Köhne, J.M., 2006. Impacts of Juniper Vegetation and Karst Geology on Subsurface Flow Processes in the Edwards Plateau, Texas. Vadose zone j. 5, 1076–1085. https://doi.org/10.2136/vzj2005.0073.

Demand, D., Blume, T., Weiler, M., 2019. Spatio-temporal relevance and controls of preferential flow at the landscape scale. Hydrol. Earth Syst. Sci. 23, 4869–4889. https://doi.org/10.5194/hess-23-4869-2019.

Dušek, J., Vogel, T., Sanda, M., 2012. Hillslope hydrograph analysis using synthetic and natural oxygen-18 signatures. Journal of Hydrology 475, 415–427. https://doi.org/10.1016/j.jhydrol.2012.10.025.

Eltner, A., Kaiser, A., Castillo, C., Rock, G., Neugirg, F., Abellan, A., 2015. Image-based surface reconstruction in geomorphometry – merits, limits and developments of a promising tool for geoscientists. Earth Surface Dynamics Disscussions, 1445–1508. https://doi.org/10.5194/esurfd-3-1445-2015.

Filipović, V., Gerke, H.H., Filipović, L., Sommer, M., 2018. Quantifying Subsurface Lateral Flow along Sloping Horizon Boundaries in Soil Profiles of a Hummocky Ground Moraine. Vadose Zone Journal 17. https://doi.org/10.2136/vzj2017.05.0106.

Gerke, K.M., Sidle, R.C., Mallants, D., 2015. Preferential flow mechanisms identified from staining experiments in forested hillslopes. Hydrol. Process. 29, 4562–4578. https://doi.org/10.1002/hyp.10468.

Germer, K., Braun, J., 2015. Determination of Anisotropic Saturated Hydraulic Conductivity of a Macroporous Slope Soil. Soil Science Society of America Journal 79, 1528–1536. https://doi.org/10.2136/sssaj2015.02.0071.

Graham, C.B., Lin, H.S., 2011. Controls and Frequency of Preferential Flow Occurrence: A 175-Event Analysis. Vadose zone j. 10, 816–831. https://doi.org/10.2136/vzj2010.0119.

Groh, J., Diamantopoulos, E., Duan, X., Ewert, F., Herbst, M., Holbak, M., Kamali, B., Kersebaum, K.-C., Kuhnert, M., Lischeid, G., Nendel, C., Priesack, E., Steidl, J., Sommer, M., Pütz, T., Vereecken, H., Wallor, E., Weber, T.K.D., Wegehenkel, M., Weihermüller, L., Gerke, H.H., 2020. Crop growth and soil water fluxes at erosion-affected arable sites: Using weighing lysimeter data for model intercomparison. Vadose zone j. 19, 1–18. https://doi.org/10.1002/vzj2.20058.

Guo, L., Chen, J., Lin, H., 2014. Subsurface lateral preferential flow network revealed by time-lapse ground-penetrating radar in a hillslope. Water Resources Research 50, 9127–9147. https://doi.org/10.1002/2013WR014603.

Guo, L., Fan, B., Zhang, J., Lin, H., 2018. Occurrence of subsurface lateral flow in the Shale Hills Catchment indicated by a soil water mass balance method. Eur J Soil Sci 69, 771–786. https://doi.org/10.1111/ejss.12701.

Guo, L., Lin, H., 2018. Addressing Two Bottlenecks to Advance the Understanding of Preferential Flow in Soils. Advance in Agronomy 147, 61–117. https://doi.org/10.1016/bs.agron.2017.10.002.

Hannes, M., Wollschläger, U., Wöhling, T., Vogel, H.-J., 2016. Revisiting hydraulic hysteresis based on long-term monitoring of hydraulic states in lysimeters. Water Resour. Res. 52, 3847–3865. https://doi.org/10.1002/2015WR018319.

Hänsel, P., Schindewolf, M., Eltner, A., Kaiser, A., Schmidt, J., 2016. Feasibility of High-Resolution Soil Erosion Measurements by Means of Rainfall Simulations and SfM Photogrammetry. Hydrology 3, 38. https://doi.org/10.3390/hydrology3040038.

Hardie, M.A., Doyle, R.B., Cotching, W.E., Lisson, S., 2012. Subsurface Lateral Flow in Texture-Contrast (Duplex) Soils and Catchments with Shallow Bedrock. Applied and Environmental Soil Science 2012. https://doi.org/10.1155/2012/861358.

Hardie, M., Lisson, S., Doyle, R., Cotching, W., 2013a. Determining the frequency, depth and velocity of preferential flow by high frequency soil moisture monitoring. Journal of contaminant hydrology 144, 66–77. https://doi.org/10.1016/j.jconhyd.2012.10.008.

Hardie, M., Doyle, R., Cotching, W., Holz, G., Lisson, S., 2013b. Hydropedology and Preferential Flow in the Tasmanian Texture-Contrast Soils. Vadose Zone Journal 12. https://doi.org/10.2136/vzj2013.03.0051.

Hartge, K.H., Horn, R., Bachmann, J., Peth, S., 2014. Einführung in die Bodenphysik. Schweizerbart, Stuttgart.

Hendrickx, J.M.H., and M. Flury. (2001). Uniform and preferential flow, mechanisms in the vadose zone, Conceptual Models of Flow and Transport in the Fractured Vadose Zone, National Research Council, National Academy Press, Washington, DC, pp. 149–187.

Hohenbrink, T.L., Lischeid, G., Schindler, U., Hufnagel, J., 2016. Disentangling the Effects of Land Management and Soil Heterogeneity on Soil Moisture Dynamics. Vadose Zone Journal 15. https://doi.org/10.2136/vzj2015.07.0107.

Holden, J., 2005. Surface Runoff and Subsurface Drainage, in: Lehr, J.H., Keeley, J. (Eds.), Water Encyclopedia, vol. 14. John Wiley & Sons, Inc, Hoboken, NJ, USA, p. 451-454.

Holz, D.J., Williard, K.W.J., Edwards, P.J., Schoonover, J.E., 2015. Soil erosion in humid regions: a review. Journal of Contemporary Water Research & Education 154, 48–59.

Jarvis, N.; Koestel, J.; and Larsbo, M. (2016). Understanding preferential flow in the vadose zone: Recent advances and future prospects. Vadose Zone J. 15(12). https://doi.org/10.2136/vzj2016.09.0075

Kahl, G., Ingwersen, J., Nutniyom, P., Totrakool, S., Pansombat, K., Thavornyutikarn, P., Streck, T., 2008. Loss of pesticides from a litchi orchard to an adjacent stream in northern Thailand. Eur J Soil Sci 59, 71–81.

Koch, J.C., Toohey, R.C., Reeves, D.M., 2017. Tracer-based evidence of heterogeneity in subsurface flow and storage within a boreal hillslope. Hydrol. Process. 31, 2453–2463. https://doi.org/10.1002/hyp.11205.

Kung, K.S.J., 1990. Preferential flow in a sandy vadose zone: 1. Field observation. Geoderma 46, 51–58.

Laine-Kaulio, H., Backnäs, S., Koivusalo, H., Laurén, A., 2015. Dye tracer visualization of flow patterns and pathways in glacial sandy till at a boreal forest hillslope. Geoderma 259-260, 23–34. https://doi.org/10.1016/j.geoderma.2015.05.004.

Laine-Kaulio, H., Koivusalo, H., 2018. Model-based exploration of hydrological connectivity and solute transport in a forested hillslope. Land Degrad Dev 29, 1176–1189. https://doi.org/10.1002/ldr.2823.

Lee, E., Kim, S., 2019a. Seasonal and spatial characterization of soil moisture and soil water tension in a steep hillslope. Journal of Hydrology 568, 676–685. https://doi.org/10.1016/j.jhydrol.2018.11.027.

Lee, E., Kim, S., 2019b. Wavelet analysis of soil moisture measurements for hillslope hydrological processes. Journal of Hydrology 575, 82–93. https://doi.org/10.1016/j.jhydrol.2019.05.023.

Lee, E., Kim, S., 2021. Characterization of soil moisture response patterns and hillslope hydrological processes through a self-organizing map. Hydrol. Earth Syst. Sci. 25, 5733–5748. https://doi.org/10.5194/hess-25-5733-2021.

Leslie, I.N., Heinse, R., 2013. Characterizing Soil-Pipe Networks with Pseudo-Three-Dimensional Resistivity Tomography on Forested Hillslopes with Restrictive Horizons. Vadose Zone Journal 12. https://doi.org/10.2136/vzj2012.0200.

Lin, H.S., Kogelmann, W., Walker, C., Bruns, M.A., 2006. Soil moisture patterns in a forested catchment: A hydropedological perspective. Geoderma 131, 345–368. https://doi.org/10.1016/j.geoderma.2005.03.013.

Linden, van Doren Jr, D.M., 1987. Simulation of interception, surface roughness, depression storage, and soil settling. NTRM, a soil crop simulation model for nitrogen, tillage, and crop-residue management. USDA-ARS, Conservation Research Rep, 90-93.

Liu, H., Lin, H., 2015. Frequency and Control of Subsurface Preferential Flow: From Pedon to Catchment Scales. Soil Science Society of America Journal 79, 362–377. https://doi.org/10.2136/sssaj2014.08.0330.

Liu, H., Yu, Y., Zhao, W., Guo, L., Liu, J., Yang, Q., 2020. Inferring Subsurface Preferential Flow Features From a Wavelet Analysis of Hydrological Signals in the Shale Hills Catchment. Water Resour. Res. 56, 1. https://doi.org/10.1029/2019WR026668.

Liu, K., Li, X., Wang, S., Zhang, H., 2022. A robust gap-filling approach for ESA CCI soil moisture by integrating satellite observations, model-driven knowledge and spatiotemporal machine learning. Hydrol. Earth Syst. Sci. https://doi.org/10.5194/hess-2022-76.

Liu, L., Ye, S., Chen, C., Pan, H., Ran, Q., 2021. Nonsequential Response in Mountainous Areas of Southwest China. Front. Earth Sci. 9. https://doi.org/10.3389/feart.2021.660244.

Logsdon, S.D., 2007. Subsurface lateral transport in glacial till soils. Transactions of the ASABE 50, 875–883.

Lu, Y., Liu, X., Zhang, M., Heitman, J., Horton, R., Ren, T., 2020. Thermo–time domain reflectometry method: Advances in monitoring in situ soil bulk density. Soil Sci. Soc. Am. j. 84, 1354–1360. https://doi.org/10.1002/saj2.20147.

Luo, Z., Niu, J., Xie, B., Zhang, L., Chen, X., Berndtsson, R., Du, J., Ao, J., Yang, L., Zhu, S., 2019. Influence of Root Distribution on Preferential Flow in Deciduous and Coniferous Forest Soils. Forests 10. https://doi.org/10.3390/f10110986.

Ma, Y., Li, Z., Deng, C., Yang, J., Tang, C., Duan, J., Zhang, Z., Liu, Y., 2022. Effects of tillage-induced soil surface roughness on the generation of surface–subsurface flow and soil loss in the red soil sloping farmland of southern China. CATENA 213, 106230. https://doi.org/10.1016/j.catena.2022.106230.

Maier, F., Meerveld, I., Weiler, M., 2021. Long-Term Changes in Runoff Generation Mechanisms for Two Proglacial Areas in the Swiss Alps II: Subsurface Flow. Water Resources Research 57. https://doi.org/10.1029/2021WR030223.

Martini, E., Wollschläger, U., Kögler, S., Behrens, T., Dietrich, P., Reinstorf, F., Schmidt, K., Weiler, M., Werban, U., Zacharias, S., 2015. Spatial and Temporal Dynamics of Hillslope-Scale Soil Moisture Patterns: Characteristic States and Transition Mechanisms. Vadose Zone Journal 14. https://doi.org/10.2136/vzj2014.10.0150.

McCord, J.T., Stephens, D.B., 1987. Lateral moisture flow beneath a sandy hillslope without an apparent impeding layer. Hydrol. Process. 1, 225–238.

McNamara, J.P., Chandler, D., Seyfried, M., Achet, S., 2005. Soil moisture states, lateral flow, and streamflow generation in a semi-arid, snowmelt-driven catchment. Hydrol. Process. 19, 4023–4038. https://doi.org/10.1002/hyp.5869.

Meinen, B.U., Robinson, D.T., 2020. Where did the soil go? Quantifying one year of soil erosion on a steep tile-drained agricultural field. The Science of the total environment 729. https://doi.org/10.1016/j.scitotenv.2020.138320.

Miyazaki, T., 1988. Water flow in unsaturated soil in layered slopes. Journal of Hydrology 102, 201–214.

Newman, B.D., Wilcox, B.P., Graham, R.C., 2004. Snowmelt-driven macropore flow and soil saturation in a semiarid forest. Hydrol. Process. 18, 1035–1042. https://doi.org/10.1002/hyp.5521.

Noguchi, S., Tsuboyama, Y., Sidle, R.C., Hosoda, I., 1999. Morphological characteristics of macropores and the distribution of preferential flow pathways in a forested slope segment. Soil Science Society of America Journal 63, 1413–1423.

Nyquist, J.E., Toran, L., Pitman, L., Guo, L., Lin, H., 2018. Testing the Fill-and-Spill Model of Subsurface Lateral Flow Using Ground-Penetrating Radar and Dye Tracing. Vadose zone j. 17. https://doi.org/10.2136/vzj2017.07.0142.

Patil, M.D., Das, B.S., 2013. Assessing the effect of puddling on preferential flow processes through under bund area of lowland rice field. Soil and Tillage Research 134, 61–71. https://doi.org/10.1016/j.still.2013.07.008.

Peyrard, X., Liger, L., Guillemain, C., Gouy, V., 2016. A trench study to assess transfer of pesticides in subsurface lateral flow for a soil with contrasting texture on a sloping vineyard in Beaujolais. Environmental science and pollution research international 23, 14–22. https://doi.org/10.1007/s11356-015-4917-5.

Pirastru, M., Marrosu, R., Di Prima, S., Keesstra, S., Giadrossich, F., Niedda, M., 2017. Lateral Saturated Hydraulic Conductivity of Soil Horizons Evaluated in Large-Volume Soil Monoliths. Water 9. https://doi.org/10.3390/w9110862.

Redding, T.E., Devito, K.J., 2008. Lateral flow thresholds for aspen forested hillslopes on the Western Boreal Plain, Alberta, Canada. Hydrol. Process. 22, 4287–4300. https://doi.org/10.1002/hyp.7038.

Redding, T., Devito, K., 2010. Mechanisms and pathways of lateral flow on aspen-forested, Luvisolic soils, Western Boreal Plains, Alberta, Canada. Hydrol. Process. 24, 2995–3010. https://doi.org/10.1002/hyp.7710.

Rieckh, H., Gerke, H.H., Sommer, M., 2012. Hydraulic properties of characteristic horizons depending on relief position and structure in a hummocky glacial soil landscape. Soil and Tillage Research 125, 123–131. https://doi.org/10.1016/j.still.2012.07.004.

Robinson, J., Buda, A., Collick, A., Shober, A., Ntarlagiannis, D., Bryant, R., Folmar, G., Andres, S., Slater, L., 2020. Electrical monitoring of saline tracers to reveal subsurface flow pathways in a flat ditch-drained field. Journal of Hydrology 586. https://doi.org/10.1016/j.jhydrol.2020.124862.

Sander, T., Gerke, H.H., 2007. Preferential Flow Patterns in Paddy Fields Using a Dye Tracer. Vadose Zone Journal 6, 105–115. https://doi.org/10.2136/vzj2006.0035.

Scaini, A., Audebert, M., Hissler, C., Fenicia, F., Gourdol, L., Pfister, L., Beven, K.J., 2017. Velocity and celerity dynamics at plot scale inferred from artificial tracing experiments and time-lapse ERT. Journal of Hydrology 546, 28–43. https://doi.org/10.1016/j.jhydrol.2016.12.035.

Schlüter, S., Vanderborght, J., Vogel, H.-J., 2012. Hydraulic non-equilibrium during infiltration induced by structural connectivity. Advances in Water Resources 44, 101–112. https://doi.org/10.1016/j.advwatres.2012.05.002.

Schneider, P., Pool, S., Strouhal, L., Seibert, J., 2014. True colors – experimental identification of hydrological processes at a hillslope prone to slide. Hydrol. Earth Syst. Sci. 18, 875–892. https://doi.org/10.5194/hess-18-875-2014.

Schwärzel, K., Ebermann, S., Schalling, N., 2012. Evidence of double-funneling effect of beech trees by visualization of flow pathways using dye tracer. Journal of Hydrology 470-471, 184–192. https://doi.org/10.1016/j.jhydrol.2012.08.048.

Sidle, R.C., Noguchi, S., Tsuboyama, Y., Laursen, K., 2001. A conceptual model of preferential flow systems in forested hillslopes: evidence of self-organization. Hydrol. Process. 15, 1675–1692. https://doi.org/10.1002/hyp.233.

Tang, X.-Y., Seuntjens, P., Cornelis, W.M., Boënne, W., Verbist, K., van Hoey, S., 2010. Preferential pathways for subsurface and overland flow on a sloped farmland: field evaluation, in: EGU General Assembly Conference Abstracts, p. 4074.

Tao, Y., Zou, Z., Guo, L., He, Y., Lin, L., Lin, H., Chen, J., 2020. Linking soil macropores, subsurface flow and its hydrodynamic characteristics to the development of Benggang erosion. Journal of Hydrology 586. https://doi.org/10.1016/j.jhydrol.2020.124829.

Tobón, C., Bruijnzeel, L.A., 2021. Near-surface water fluxes and their controls in a sloping heterogeneously layered volcanic soil beneath a supra-wet tropical montane cloud forest (NW Costa Rica). Hydrological Processes 35. https://doi.org/10.1002/hyp.14426.

Tromp-van Meerveld, H.J., McDonnell, J.J., 2006. Threshold relations in subsurface stormflow: 2. The fill and spill hypothesis. Water Resour. Res. 42. https://doi.org/10.1029/2004WR003800.

Uchida, T., Asano, Y., Mizuyama, T., McDonnell, J.J., 2004. Role of upslope soil pore pressure on lateral subsurface storm flow dynamics. Water Resour. Res. 40. https://doi.org/10.1029/2003WR002139.

Wales, N.A., Gomez-Velez, J.D., Newman, B.D., Wilson, C.J., Dafflon, B., Kneafsey, T.J., Soom, F., Wullschleger, S.D., 2020. Understanding the relative importance of vertical and horizontal flow in ice-wedge polygons. Hydrol. Earth Syst. Sci. 24, 1109–1129. https://doi.org/10.5194/hess-24-1109-2020.

Walter, M.T., Kim, J.-S., Steenhuis, T.S., Parlange, J.-Y., Heilig, A., Braddock, R.D., Selker, J.S., Boll, J., 2000. Funneled flow mechanisms in a sloping layered soil. Water Resour. Res. 36, 841–849.

Weiler, M., McDonnell, J.J., 2007. Conceptualizing lateral preferential flow and flow networks and simulating the effects on gauged and ungauged hillslopes. Water Resour. Res. 43. https://doi.org/10.1029/2006WR004867.

Wiekenkamp, I., Huisman, J.A., Bogena, H.R., Lin, H.S., Vereecken, H., 2016. Spatial and temporal occurrence of preferential flow in a forested headwater catchment. Journal of Hydrology 534, 139–149. https://doi.org/10.1016/j.jhydrol.2015.12.050.

Wienhöfer, J., Lindenmaier, F., Zehe, E., 2011. Challenges in Understanding the Hydrologic Controls on the Mobility of Slow-Moving Landslides. Vadose Zone Journal 10, 496–511. https://doi.org/10.2136/vzj2009.0182.

Wilcox, B.P., Newman, B.D., Brandes, D., Davenport, D.W., Reid, K., 1997. Runoff from a semiarid ponderosa pine hillslope in New Mexico. Water Resour. Res. 33, 2301–2314.

Wöhling, T., Bidwell, V.J., Barkle, G.F., 2012. Dual-tracer, non-equilibrium mixing cell modelling and uncertainty analysis for unsaturated bromide and chloride transport. Journal of contaminant hydrology 140-141, 150–163. https://doi.org/10.1016/j.jconhyd.2012.08.001.

Xie, M., Šimůnek, J., Zhang, Z., Zhang, P., Xu, J., Lin, Q., 2019. Nitrate subsurface transport and losses in response to its initial distributions in sloped soils: An experimental and modelling study. Hydrological Processes 33, 3282–3296. https://doi.org/10.1002/hyp.13556.

Zhang, B., Tang, J.L., Gao, C., Zepp, H., 2011. Subsurface lateral flow from hillslope and its contribution to nitrate loading in streams through an agricultural catchment during subtropical rainstorm events. Hydrol. Earth Syst. Sci. 15, 3153–3170. https://doi.org/10.5194/hess-15-3153-2011.

Zhu, Q., Lin, H.S., 2009. Simulation and validation of concentrated subsurface lateral flow paths in an agricultural landscape. Hydrol. Earth Syst. Sci. 13, 1503–1518.

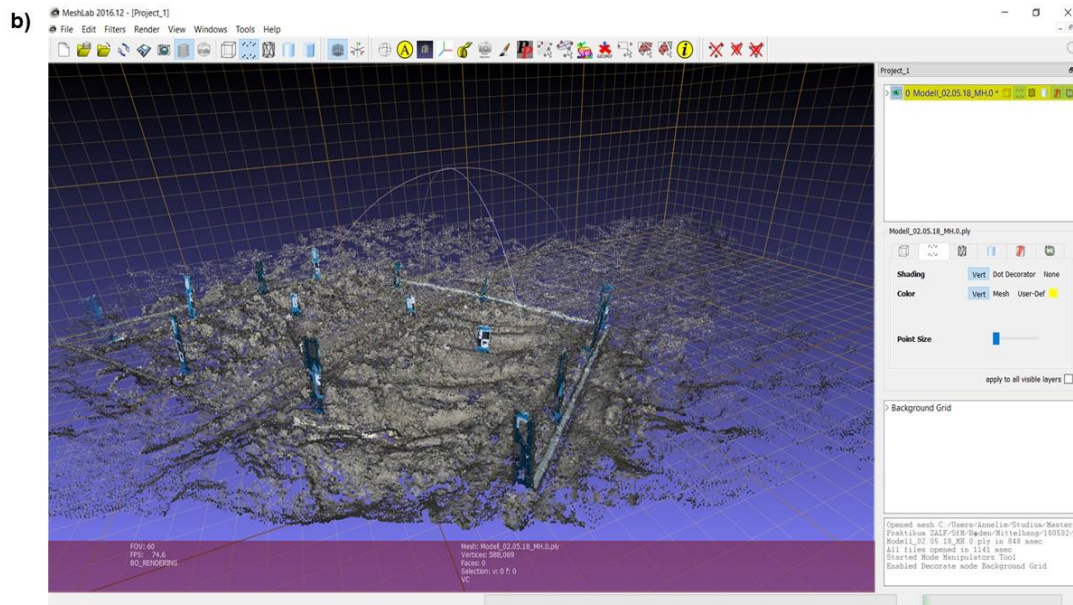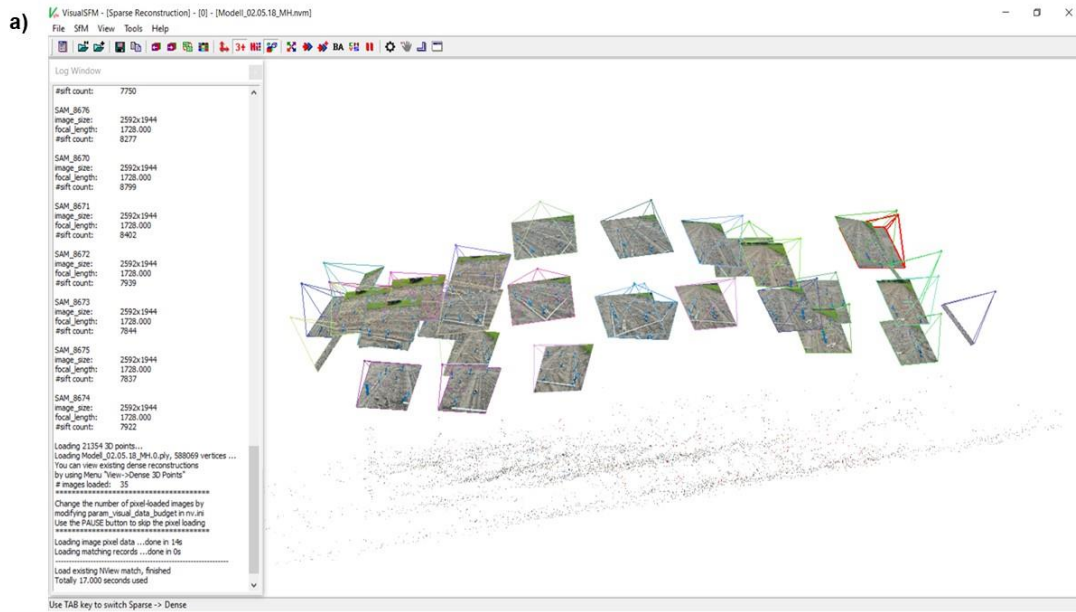# Appendix

Appendix for Chapter 2

A2.1: Potential flow lines at the soil surface of the hillslope runoff experiment determined from a digital elevation model (GlobalMapper 19.0, LiDAR, 2018, resolution: 1.2 cm x 1.2 cm).
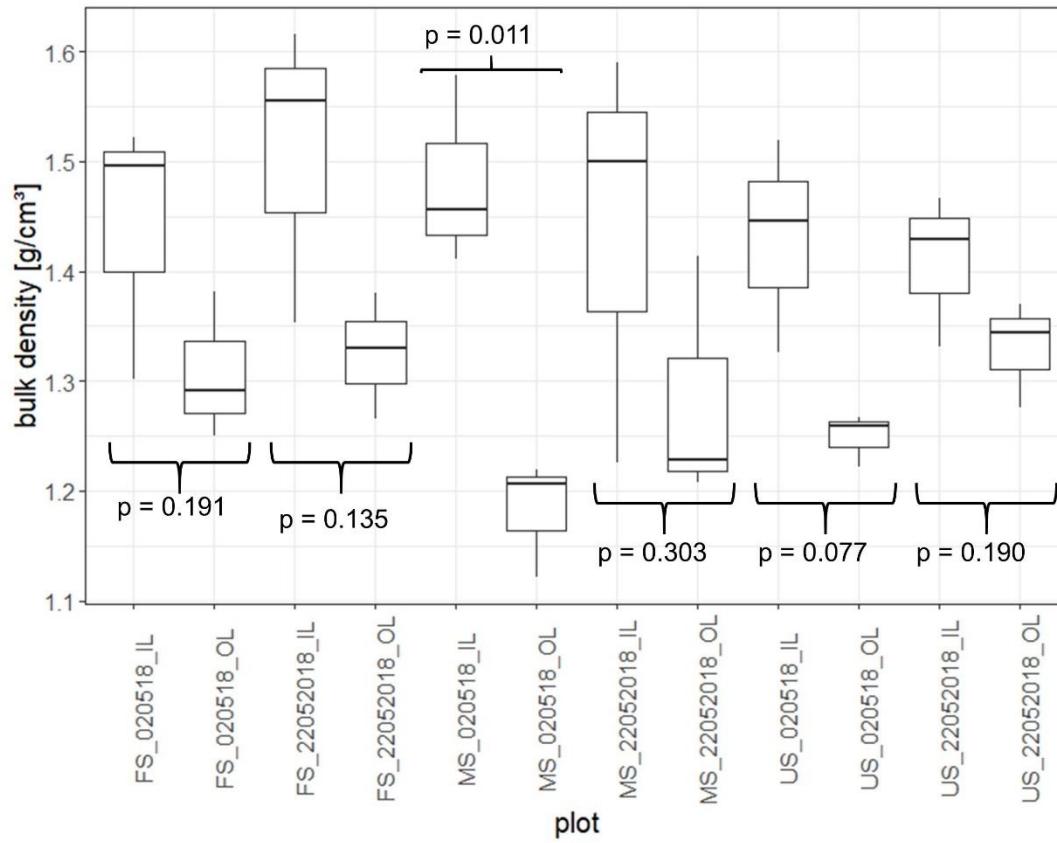
A2.2: Boxplots and p-values of Welch's t-test of bulk density differences between inside (IL) and outside (OL) the tractor lane; FS: footslope, MS: middle slope, US: upper slope; dates of bulk density measurement: 02052018 – May 02, 2018; 22052018 – May 22, 2018
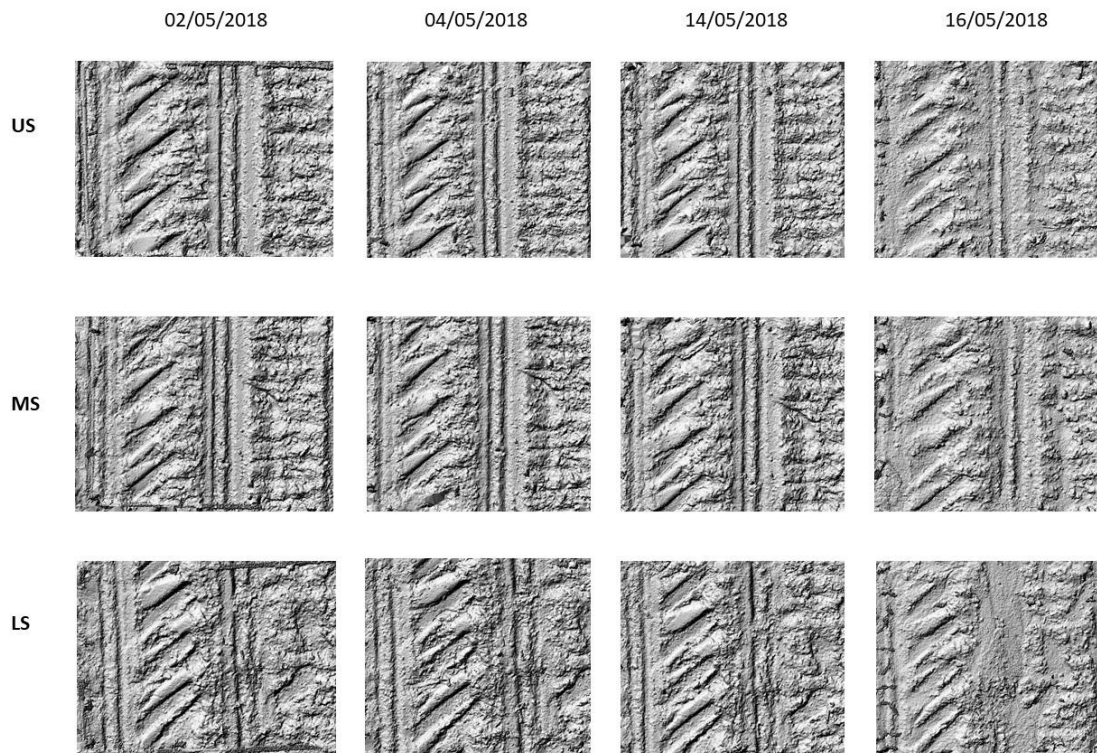
A2.3: Soil collected at the footslope collector station on May 16, 2018. (Photo: A. Ehrhardt)

Appendix

A2.4: Processing of the 3D-models in (a) VisualSfM and (b) MeshLab.

A2.5: DEMs of the upper-, middle- and footslope (US, MS and FS, respectively) from May 02 till May 16, 2018.

Appendix for Chapter 3

A3.1: Dates of cultivation and cropping from autumn 2016 to spring 2018 (Gernot Verch, ZALF, personal communication, November 2019).

Date	Measurement
19 Sept. 2016	Seed furrow for winter rye (breed: SU Performer)
7 Oct. 2016	Sowing winter rye
14 Mar. 2017	Herbicide application (4.5 L ha^{-1} Round up)
20 Apr. 2017	Fertilization (110 kg ha^{-1} P$_2$O$_5$, 300 kg ha^{-1} K$_2$O)
21 Apr. 2017	Heavy grubber (Incorporation of liquid manure)
24 Apr. 2017	Heavy grubber (treatment dead winter rye), seedbed preparation with circular grubber, sowing maize (breed: Zoey)
2 May 2017	Fertilization (160 kg N ha^{-1})
22 May 2017	Herbicide application (1.2 L ha^{-1} Calaris + 1.25 L ha^{-1} Dual Gold + 16 g ha^{-1} Peak)
25 Sept. 2017	Manual harvest lysimeters
26 Sept. 2017	Harvest field
27 Sept. 2017	Incorporation of maize stubbles with mulcher
28 Sept. 2017	Seed furrow for winter rye (breed: SU Cossanni)
13 Oct. 2017	Sowing winter rye
19 Mar. 2018	Herbicide application (3.0 L ha^{-1} Round up)
27 Mar. 2018	Fertilization (50 kg ha^{-1} P$_2$O$_5$)
09 Apr. 2018	Soil cultivation with heavy grubber and circular grubber, sowing oat (breed: Apollon)
19–20 Apr. 2018	Fertilization (1 dt ha^{-1} Kieserit, 100 kg N ha^{-1})
4 May 2018	Herbicide application (70 g ha^{-1} Biathlon + 1.0 L ha^{-1} Dash)
30 Aug. 2018	Harvest

A3.2: Precipitation measurement equipment at the experimental field site "Holzendorf" CarboZalf-D; see Fig 3.2 for the location of sensors of numbers 1–5.
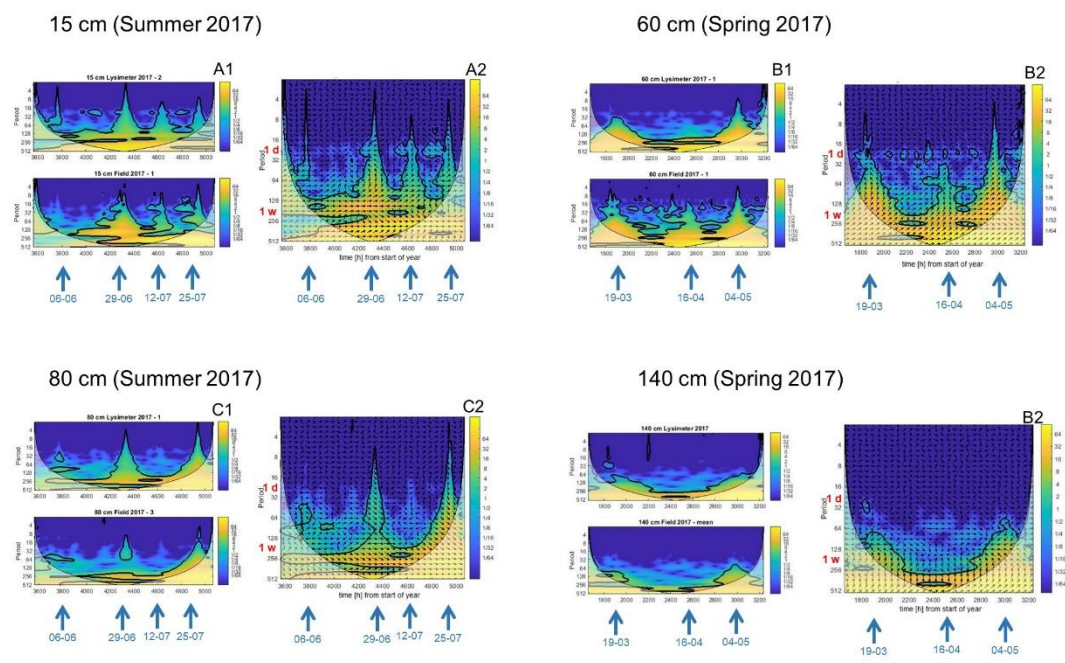
No.	RS	Type	Product	Manufacturer	Start date
	min				
1	1	Usc	WXT520	Vaisala (Finland)	11 June 2009
		TP_h	52202	Young (USA)	
2	30	TP_nh	RG50	Seba (Germany)	18 Sept. 2009
3	10	Usc	WXT520	Vaisala	25 Sept. 2014
4	30	TP_h	SBS500H	Campbell (USA)	07 Nov. 2014 to Sept. 2015
5	30	TP_h	SBS500H	Campbell	3 Nov. 2011

A3.3: Gap-filling procedure

The data time series of the pressure head and volumetric SWC were quality controlled by an automatic and by a manual "flagging" procedure to remove sensor errors (Hans-Jörg Vogel and Ralf Gründling, UFZ, Halle, personal communication 2019). In this procedure, all values outside measurement ranges (i.e., +200 to −850 hPa for pressure heads, 5 to 60 Vol-% for volumetric SWC) and errors indicated by "999" or negative SWC readings were automatically removed. Isolated spikes or noise was identified and removed by calculating the moving median of 13 values and defining a tolerance interval of ±20 hPa for pressure heads. For the SWC the moving medians of 5, 7, and 25 values were computed and tolerance intervals of ±1, ±3, and ±5 Vol-% were chosen to remove sharp, medium, and coarse spikes (sudden, implausible changes in SWC), respectively. Residual data steps such as short-term offsets in the level of measured SWC values due to automatic signal interpretation were identified by calculating the absolute change between two consecutive values and limiting this difference to +15 and −5 Vol-%. For the pressure heads also, shorter measurement periods were removed, if there were data gaps of 1 d and the number of values was smaller than 342 in 3 d. These short measurement periods occurred sometimes in summer between intermittent sensor failures. Gaps in the time series of the two soil moisture state variables, pressure head and SWC, were filled according to Groh et al. (2020) by calculating linear models of the time series of parallel measurements (Villazón & Willems, 2010), if only one sensor failed. If the gaps could not be filled by using data from similar lysimeter or field measurements that were operating in parallel and the missing period was shorter than 1 d, a linear interpolation procedure between the last and the first correct data points was applied (Falge et al., 2001).
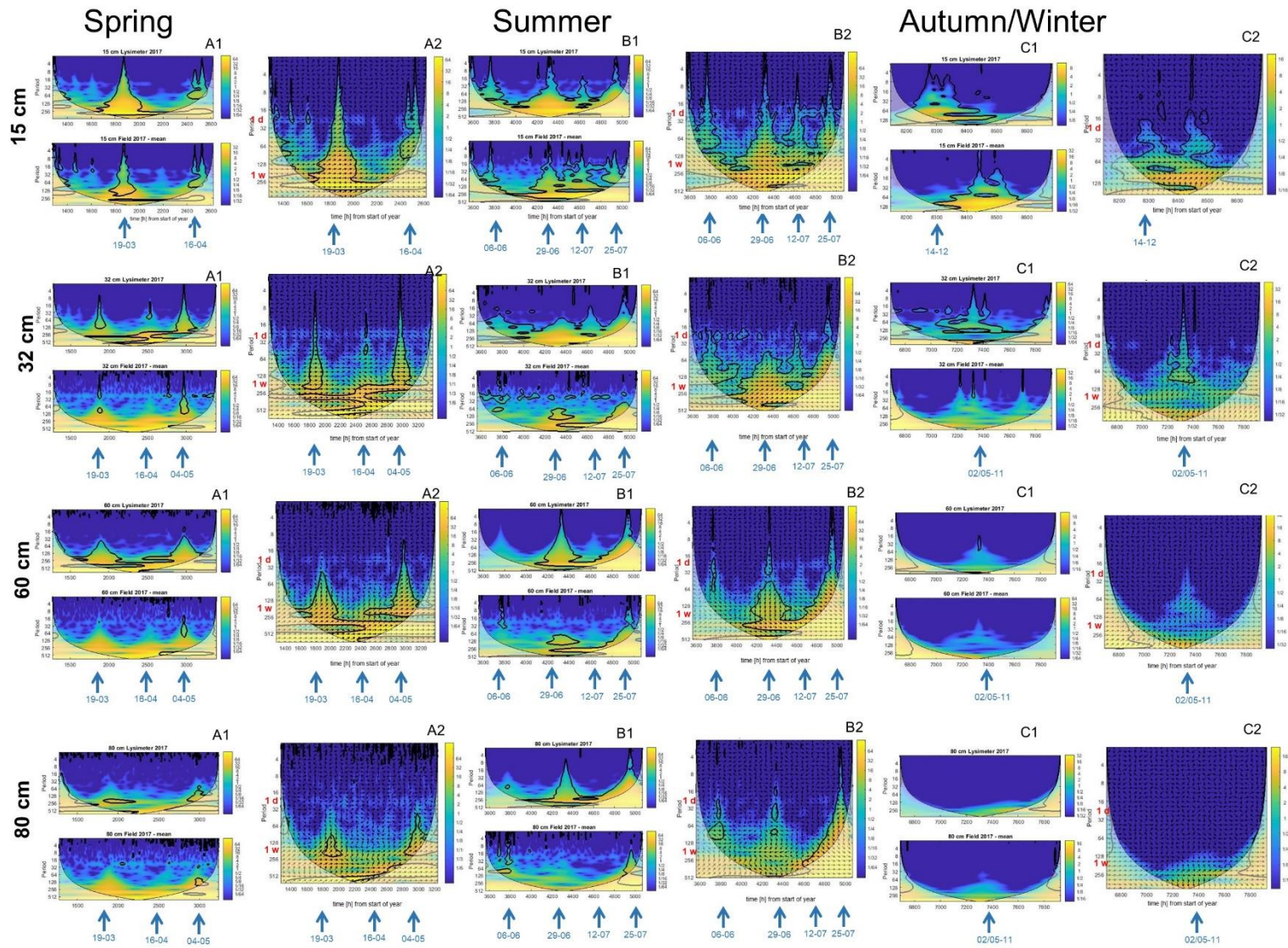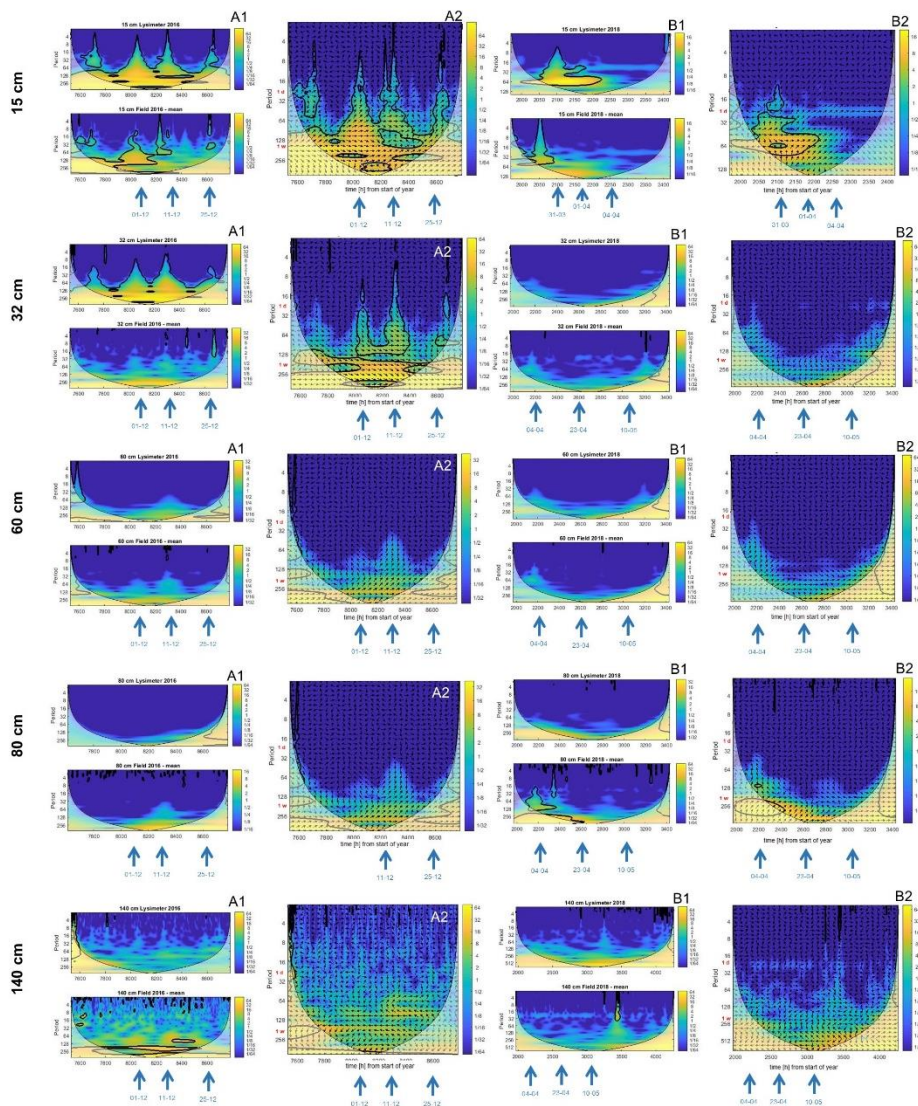
A3.4: Wavelet spectra in lysimeter and field (A1, B1, C1) and cross-wavelet spectra of soil water content (SWC) in lysimeter and field (A2, B2, and C2) at 15-, 32-, 60-, and 80-cm depth in spring, summer, and autumn of the wet year 2017. Major precipitation events that were further analyzed are marked with a blue arrow and a date below the plot. Time is given at the x axis in the number of hours from the start of the year. The period of the spectra is given in hours. The area outside the cone of influence (COI) is shaded and mark the part of the plot where edge effects influence the data. Areas in the wavelet and cross wavelet spectra that differ significantly (significance level = 5%) from a background power spectrum are shown as thick contour lines. Arrows in the cross wavelet spectrum illustrate the time shifts of the water content in response to precipitation between lysimeter and field. Arrows that are turned right (east) indicate a perfect correlation. If they are turned left (west), the time series show anti-correlation. Arrows pointing upwards indicate a faster reaction to precipitation in the field soil as compared with the lysimeter soil, whereas arrows turned downwards show a faster reaction in the lysimeter.
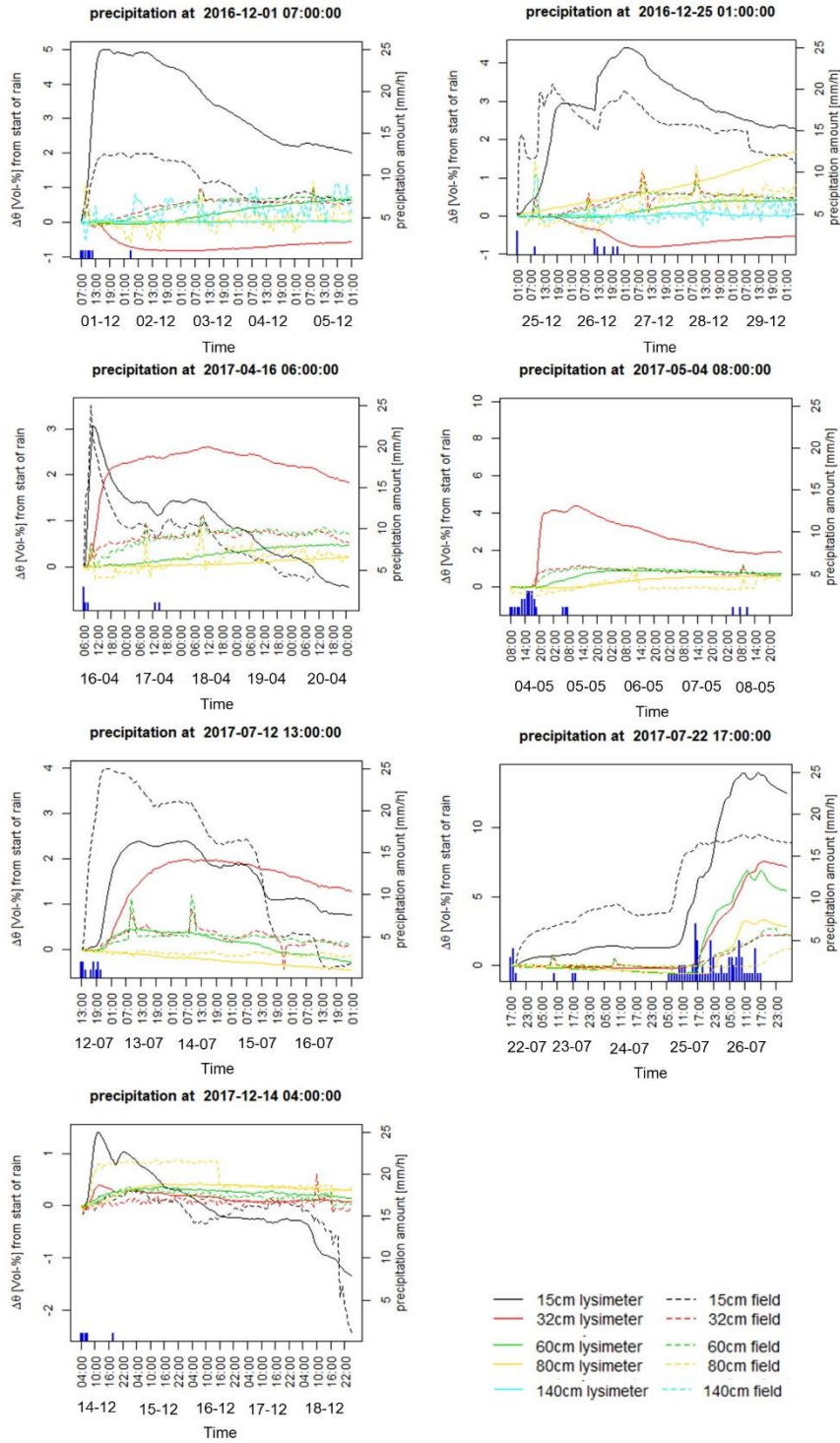
A3.5: Wavelet spectra of lysimeter and field (A1, B1, C1, and D1) and cross wavelet spectra of pressure head values in lysimeter and field (A2, B2, C2, and D2) at 15-cm (summer 2017), 60-cm (spring 2017), 80-cm (summer 2017) and 140-cm depth (spring 2017). Major precipitation events that were further analyzed are marked with a blue arrow and a date below the plot. Time is given at the x axis in the number of hours from the start of the year. The period of the spectra is given in hours. The area outside the cone of influence (COI) is shaded and mark the part of the plot where edge effects influence the data. Areas in the wavelet and cross wavelet spectra that differ significantly (significance level = 5%) from a background power spectrum are shown as thick contour lines. Arrows in the cross wavelet spectrum illustrate the time shifts of the water content in response to precipitation between lysimeter and field. Arrows that are turned right (east) indicate a perfect correlation. If they are turned left (west), the time series show anti-correlation. Arrows pointing upwards indicate a faster reaction to precipitation in the field soil as compared with the lysimeter soil, whereas arrows turned downwards show a faster reaction in the lysimeter.

A3.6: Wavelet spectra of lysimeter and field (A1, B1) and cross wavelet spectra of soil water content (SWC) in lysimeter and field (A2, B2) in 15-cm, 32-cm, 60-cm, 80-cm, and 140-cm depth in autumn 2016 (dry year) and spring 2018 (dry year). Major precipitation events that were further analyzed are marked with a blue arrow and a date below the plot. Time is given at the x axis in the number of hours from the start of the year. The period of the spectra is given in hours. The area outside the cone of influence (COI) is shaded and mark the part of the plot where edge effects influence the data. Areas in the wavelet and cross wavelet spectra that differ significantly (significance level = 5%) from a background power spectrum are shown as thick contour lines. Arrows in the cross wavelet spectrum illustrate the time shifts of the water content in response to precipitation between lysimeter and field. Arrows that are turned right (east) indicate a perfect correlation. If they are turned left (west) the time series show anti-correlation. Arrows pointing upwards indicate a faster reaction to precipitation in the field soil as compared with the lysimeter soil, whereas arrows turned downwards show a faster reaction in the lysimeter.

A3.7: Soil water content (SWC) increase in response to additional precipitation events from Tab. 3.4 in lysimeter and field at 15-cm, 32-cm, 60-cm, 80-cm, and 140-cm depth in 2016, 2017, and 2018.

124

Appendix for Chapter 4
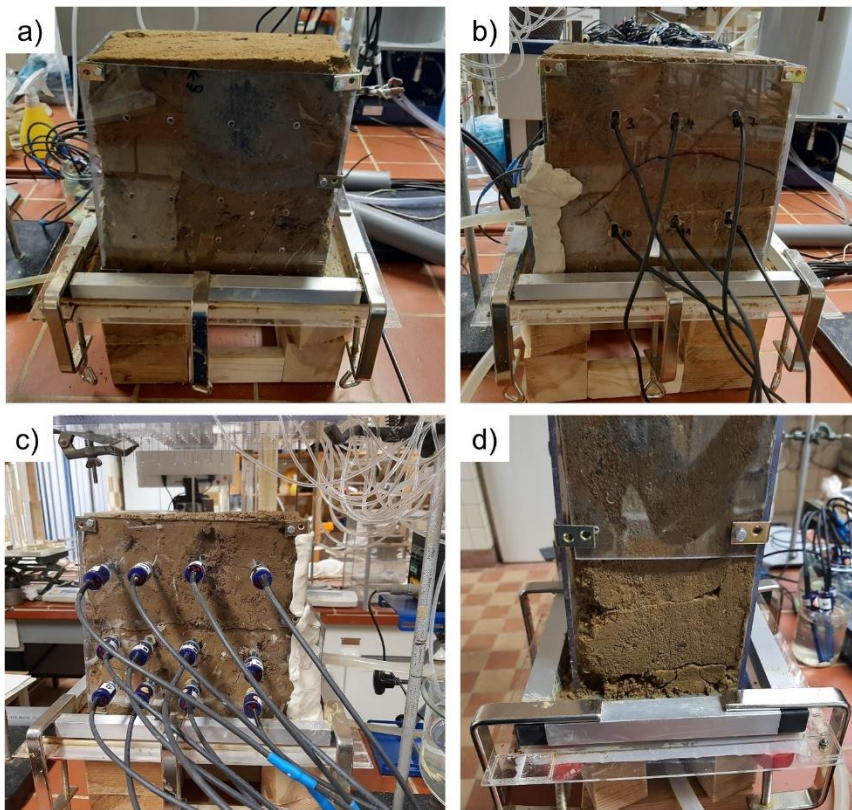
A4.1: Sensor insertion into soil monolith in carbonate glass box: soil monolith in the carbonate glass box (a), FDR sensor installation (b), 12 tensiometers inserted into the box (c), opening for the side tension disc (d)
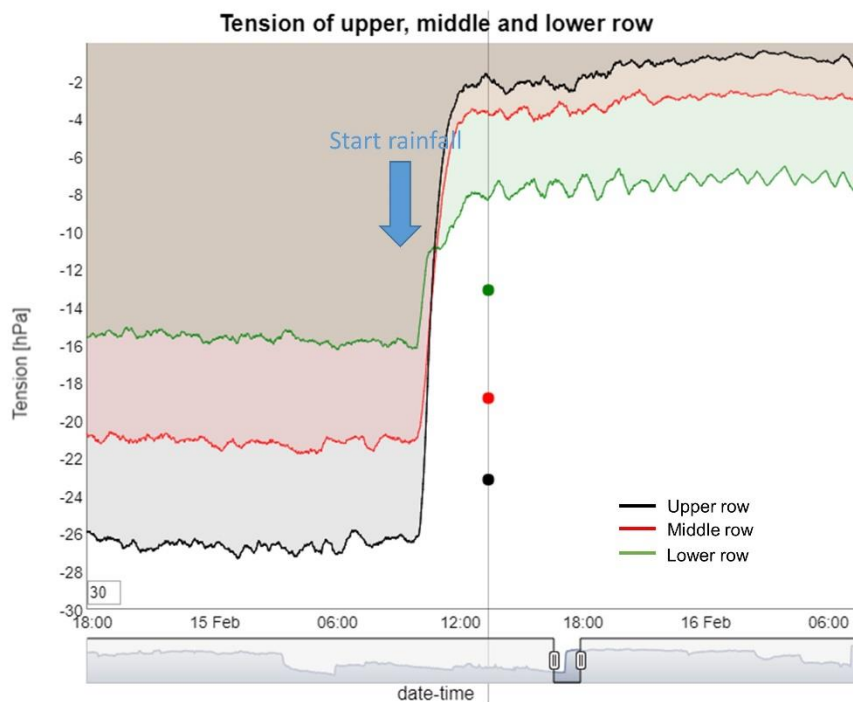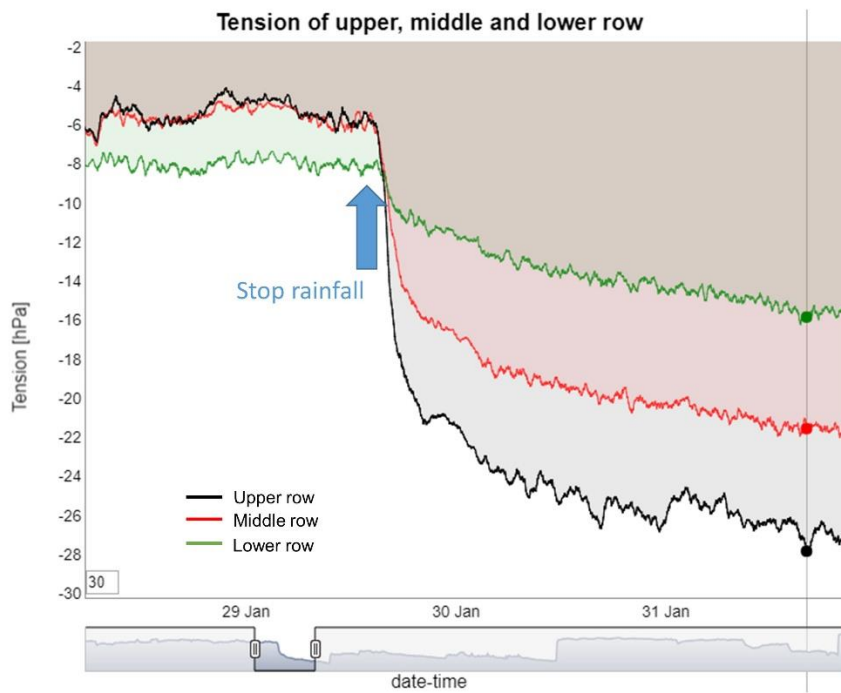
A4.2: Time series of the pressure heads taken for the derivation of the water retention curve during wetting of the monolith; time series was smoothed with a moving average of 30 values
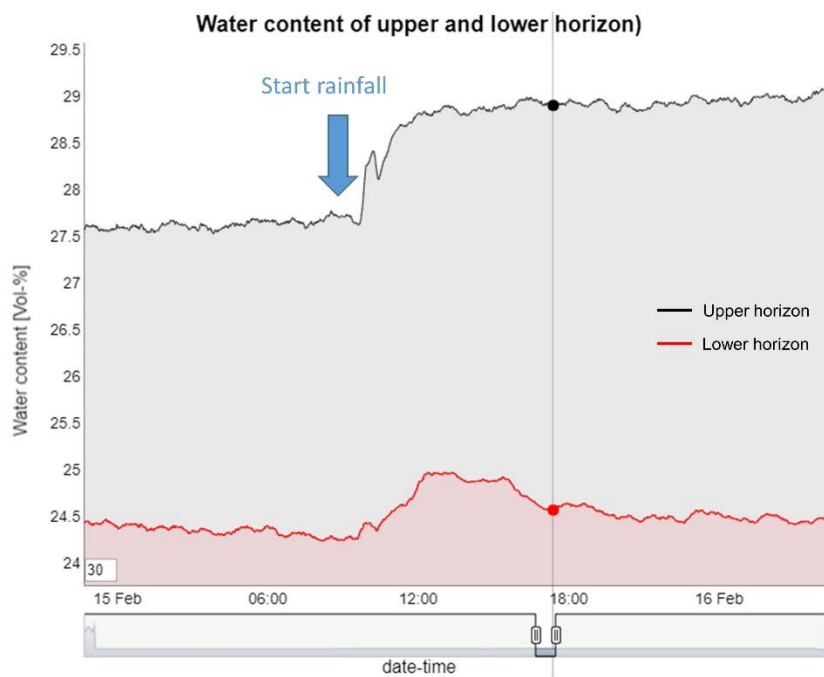
A4.3: Time series of the water content taken for the derivation of the water retention curve during wetting of the monolith; time series was smoothed with a moving average of 30 values
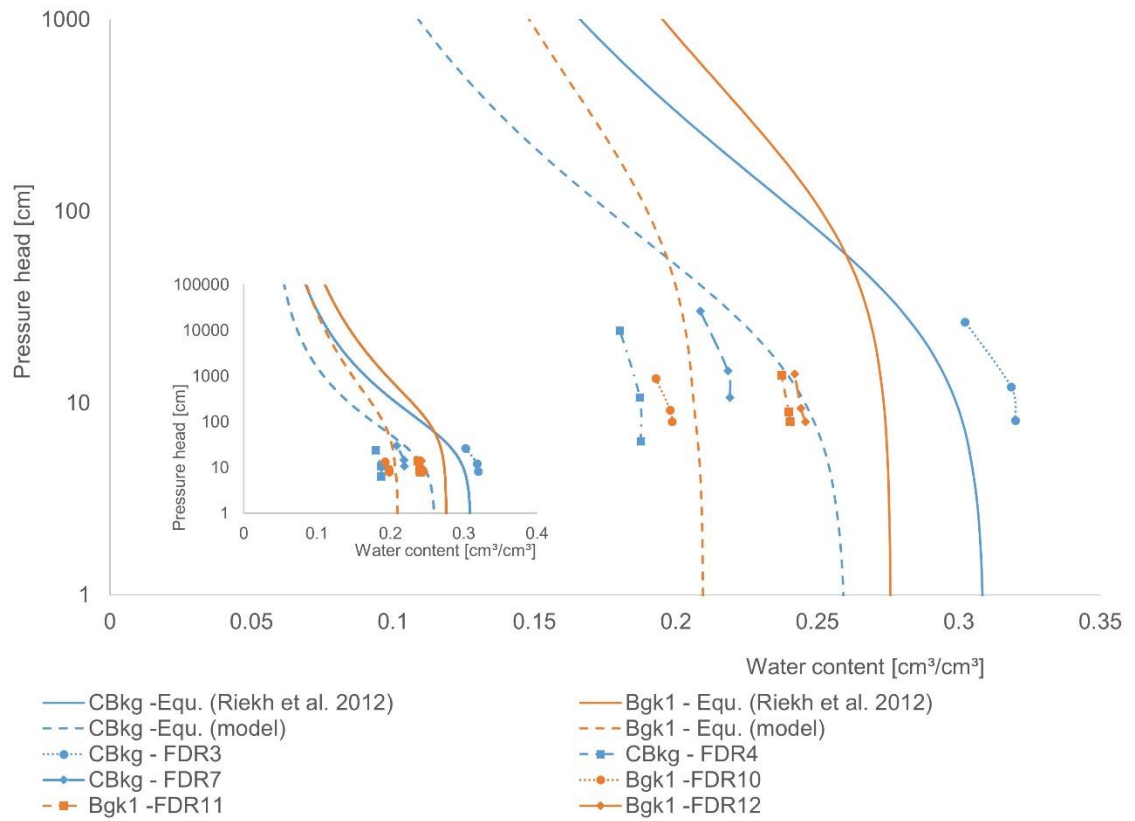
A4.4: Modelled curves of the CBkg (blue) and the Bgk1 (orange) horizons form this paper (broken lines) and from Rieckh et al. 2012 (solid lines) and the measured values from the monolith experiment during drying (short curves)

A4.5: Time series of the pressure heads taken for the derivation of the water retention curve during drying of the monolith; time series was smoothed with a moving average of 30 values
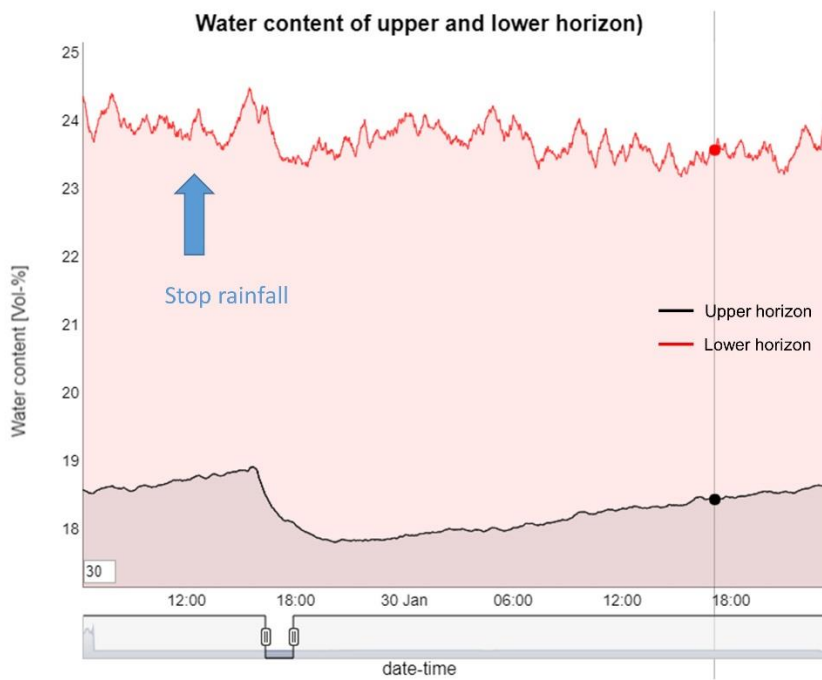

A4.6: Time series of the water content taken for the derivation of the water retention curve during drying of the monolith; time series was smoothed with a moving average of 30 values

List of Publications

Published

Kaiser, A., **Ehrhardt, A.**, Eltner, A., 2018. Addressing uncertainties in interpreting soil surface changes by multitemporal high-resolution topography data across scales. Land degradation & development 29, 2264–2277. https://doi.org/10.1002/ldr.2967.

Ehrhardt, A., Groh, J., Gerke, H.H., 2021. Wavelet analysis of soil water state variables for identification of lateral subsurface flow: Lysimeter vs. field data. Vadose zone j. 20. https://doi.org/10.1002/vzj2.20129.

Ehrhardt, A., Deumlich, D., Gerke, H.H., 2022. Soil Surface Micro-Topography by Structure-from-Motion Photogrammetry for Monitoring Density and Erosion Dynamics. Front. Environ. Sci. 9. https://doi.org/10.3389/fenvs.2021.737702.

Ehrhardt, A., Berger, K., Filipović, V., Wöhling, T., Vogel, H.-J., Gerke, H.H., 2022. Tracing lateral subsurface flow in layered soils by undisturbed monolith sampling, targeted laboratory experiments and model-based analysis. Vadose zone j., e20206, https://doi.org/10.1002/vzj2.20206

In Discussion

Ehrhardt, A., Gerke, H.H., 2022. Exploring the Possibility of the Soil Temperature to Identify Preferential and Lateral Subsurface Flows. Vadose zone j.

Curriculum vitae

Personal Data

- Name: Annelie Ehrhardt
- Date of Birth: 11 August 1993
- Place of Birth: Berlin

Education

- Since February 2019: Doctoral student at "Martin-Luther-Universität Halle-Wittenberg" and "Leibniz-Zentrum für Agrarlandschaftsforschung (ZALF) e.V." in the working group „Hydropedologie"
- September 2016 – Dezember 2018: Master of Science in Geoecology at "Technische University Bergakademie Freiberg", Saxony, Germany
    - Master Thesis: „Experimentelle Untersuchung der Infiltration in gefrorene Böden"
- September 2013 – August 2016: Bachelor of Science in Geoecology at "Technische University Bergakademie Freiberg", Saxony, Germany
    - Bachelor Thesis: "Untersuchung von Sackung in Lössböden aufgrund von Starkniederschlagsereignissen"

Datum / Date   (Annelie Ehrhardt)

Eidesstattliche Erklärung / *Declaration under Oath*

Ich erkläre an Eides statt, dass ich die Arbeit selbstständig und ohne fremde Hilfe verfasst, keine anderen als die von mir angegebenen Quellen und Hilfsmittel benutzt und die den benutzten Werken wörtlich oder inhaltlich entnommenen Stellen als solche kenntlich gemacht habe.

I declare under penalty of perjury that this thesis is my own work entirely and has been written without any help from other people. I used only the sources mentioned and included all the citations correctly both in word or content.

—————————————————   —————————————————

Datum / Date   (Annelie Ehrhardt)